Summer 2021

DESIGN AND DEVELOPMENT OF A VARIABLE RESISTANCE HAND EXERCISER USING A COMPLIANT MECHANISM

Jyothi Komatireddy
Missouri University of Science and Technology

Department:

DESIGN AND DEVELOPMENT OF A VARIABLE RESISTANCE HAND EXERCISER USING A COMPLIANT MECHANISM

by

JYOTHI KOMATIREDDY

A THESIS

Presented to the Graduate Faculty of the

MISSOURI UNIVERSITY OF SCIENCE AND TECHNOLOGY

In Partial Fulfillment of the Requirements for the Degree

MASTER OF SCIENCE IN MECHANICAL ENGINEERING

2021

Approved by:

Ashok Midha, Advisor
K. Chandrashekhara
Frank Liou

ABSTRACT

Rehabilitation exercise plays a vital role in recovering from an injury or illness condition by improving flexibility and restoring muscle strength. If not done correctly, exercising can cause more damage to the health condition than in healing. Understanding the muscle's resistance level while performing an exercise helps design the exercising equipment not to overstrain the muscle during operation. This research presents a methodology to develop a variable-resistance hand exerciser by using a compliant cam-follower mechanism. The proposed design comprised a compliant follower and a rigid cam. The rigid cam is synthesized using the human hand force-deflection profile as an input along with the material and geometric properties of the compliant follower. A novel pseudo-rigid body model approach is used to inspect the compliant follower's interference with a rigid cam during the operation. Design considerations such as optimizing the exerciser weight and size are considered by analyzing the input variables. Anthropometric data of the hand is also employed to develop the exerciser in conjunction with hand tool design guidelines. A customization process is proposed to adapt to individual needs. The results are also validated experimentally.

ACKNOWLEDGMENTS

Firstly, I would like to express my sincere gratitude to my advisor, Dr. Ashok Midha, for his generous support and invaluable guidance in completing this research study. His continuous motivation and visionary thinking have made this project come into the current shape. I am immensely thankful for the given opportunity and mentorship provided.

I would also like to extend my thanks to my committee members, Dr. K. Chandrashekhara, for providing me an excellent education in the subjects of Finite Element Analysis and Composite Materials and Structures and Dr. Frank Liou for his words of encouragement. Their insightful thoughts and constructive comments are broadly acknowledged.

I want to thank the Department of Mechanical and Aerospace Engineering and the Product Innovation and Creativity Center (PICC) at Missouri S&T for the facilities provided to accomplish the research.

Special thanks to Vamsi Lodagala and Pratheek Bagivalu Prasanna for the practical advice and exemplary contributions to this project's development. The influential work of former student, Kyle Buschkoetter, is gratefully acknowledged; I am thankful for his generous assistance provided with the synthesis approach. Finally, I thank my family for providing and supporting my education and always being understanding.

TABLE OF CONTENTS

Page

LIST OF ILLUSTRATIONS

Page

LIST OF TABLES

Page

NOMENCLATURE

Symbol	Description
a	X co-ordinate of deflected beam
a_i	X co-ordinate of curved beam
A_{k-1}	Constant coefficient of element k-1
b	Y co-ordinate of deflected beam
b_i	Y co-ordinate of curved beam
B_{k-1}	Linear coefficient of element k-1
C_{k-1}	Quadratic coefficient of element k-1
D	Displacement
D_{in}	Input displacement
D_k	Displacement when follower is at node k
E	Modulus of elasticity (Young's Modulus)
F_{out}	Output force
k_{max}	Number of nodes on cam profile
k_o	Nondimensionalized parameter
L	Beam length
N_k	Normal force at node k
n_k	Axial to transverse force ratio at node k
P_k	Transverse component of force at node k
P_{max}	Maximum grip force
P	Force

r	Radius of Delrin cylinder
R	Radius of curvature
T	Beam thickness
Travel	Total input displacement
W	Beam width
X	X co-ordinate of cam surface
Y	Y co-ordinate of cam surface
α_k	Angle of inclination of cam at node k
γ	Characteristic radius factor
Θ	Pseudo-rigid-body angle
Θ_k	Angle of follower from vertical at node k
Θ_1	Start angle of follower
$\Theta_k - \Theta_1$	Pseudo-rigid-body angle at node k
μ	Coefficient of friction

1. INTRODUCTION

1.1. COMPLIANT MECHANISMS

Unlike rigid-body mechanisms, compliant mechanisms gain mobility through the deflections of the flexible members [1]. These deflections allow for the transfer of force, motion, and energy [2]. By replacing one or more rigid links/bodies with flexible members, the rigid-body mechanism may be converted into compliant mechanisms. Figure 1.1 shows an example of a fully compliant mechanism known as compliers®, a one-piece compliant fishhook remover.

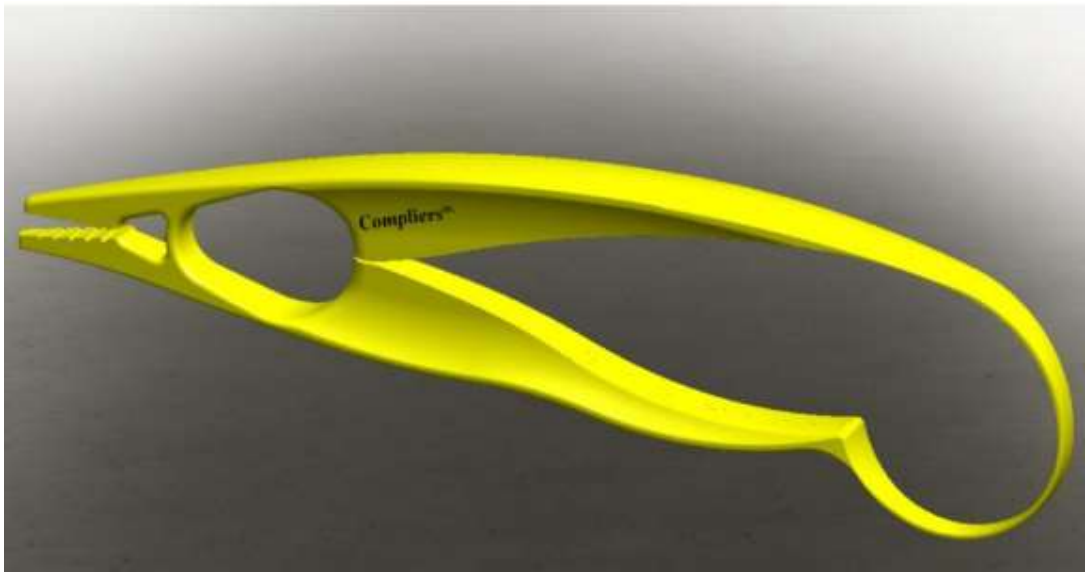

Figure 1.1 Compliers®

The compliant mechanism has several advantages over rigid-body mechanisms such as:

- Less number of components:

The total number of parts can be reduced by replacing multiple rigid components with one compliant segment.

- Reduction in assembly time:

The reduction in the number of components, in turn, results in a decrease in assembly time

- Reduction in manufacturing cost:

Reduction in manufacturing cost is derived from a less number of components and material requirements. And also, many compliant members can be manufactured through 3D printing and quick and effective production. In the rigid body mechanisms, the initial equipment setup can cost more.

- Reduction in wear:

Reduced wear is achieved because of fewer components in the design and the absence of backlash associated with rigid-body mechanisms.

- Increased precision:

The improved precision is achieved because there won't be any backlash in the compliant members, unlike the moving parts in the rigid-body mechanisms.

- No need for lubrication:

With the idea of single-piece designs, the need for lubrication can be eliminated completed.

- Reduction in total weight:

As a result of the reduced total number of components in the design, the product's total weight can be minimized to a greater extent compared to rigid-body mechanisms.

Also, the flexible members can be sized up to the size of human hair, which is an added advantage both in terms of weight and portability of the mechanism.

Along with the significant advantages, there are also several challenges involved in compliant mechanisms

- Creep:

Compliant members undergo larger deformations and cyclic loads compared with rigid bodies. Due to the higher stresses in the members for a long time can cause creep in the material.

- Fatigue failure:

Compliant members who remain under cyclic loads for a long time can also cause fatigue failure. While designing any compliant member, one should consider the fatigue life factor to accommodate the components' expected life.

- Energy loss:

Unlike rigid bodies, compliant members don't transfer total energy; indeed, it will store some energy. This can be a drawback in some applications where the function is to transfer total energy from one input to output.

- Component replacement cost/ material wastage:

In compliant mechanisms, members are generally designed as integrated parts, where the failure in one joint can adversely affect the performance of the component. The replacement of those joints could get challenging, leading to the disposal of the complete unit.

1.2. BACKGROUND HISTORY OF COMPLIANT MECHANISMS

Compliant mechanisms heavily rely on the deflections of their members. Analyzing the large deflection behavior helps in the design and development of tools. The study of the deflections in the compliant mechanism is often involved with load and displacement as input boundary conditions. Euler-Bernoulli equations are used to study the beam's small deflections, which uses the small-angle approximation [3]. But often, the compliant mechanisms are involved with large deflections and the assumption of small-angle approximation may not be appropriate to use in this case. In consideration of that, Bisshop and Drucker [4] developed a closed-form solution of elliptical integrals to solve the large deflection of the cantilever beam. This process is notoriously cumbersome, but the results are accurate. This idea was extended by Shoup [5] further for different boundary conditions. The kinetostatic synthesis approach satisfying kinematics of deformation and static equilibrium is developed by Burns [6] and Burns and Crossley [7]. Even though the closed-form elliptic integral method [8,9] is complex, the results are very effective and made this method a standard procedure to validate the results from other alternative methods.

To overcome the difficulties of complexity a simple and effective method of PRBM is introduced. Based on the observation of Burns and Crossley [7], which states, "the path tip of a cantilever beam under forces of magnitude and direction, very closely approximates an arc centered at one-sixth span from the fixed end." Figure 1.2 shows the PRBM of the fixed free beam with force at one end. In the early discussions of Midha and Her [10], the idea of using equivalent rigid-body models and springs to study the behavior of compliant mechanisms is mentioned. The introductory studies on the PRBM

concept are performed by Salamon and Midha [11,12]. Howell and Midha [13] and Howell et al. [14] developed the methodology of designing and analyzing a cantilever beam large deflection using the PRBM approach. The PRBM for an initially curved fixed-free segment and initially straight fixed-guided segments are developed by Howell [15]. The PRBM parameters of a fixed free compliant beam subjected to end forces are improvised by Pauly and Midha [16]. PRBM's of a fixed-free compliant segment with initially straight, initially curved small length flexural pivot (SLFP) are verified using an elliptical integral approach [17]. Midha and Howell [18,19] extended the PRBM for several compliant segments and provided a design methodology as 'synthesis with compliance.' Design tables for compliance synthesis are developed by Midha et al. [20]. Bapat et al. [21] implemented the use of energy/torque equations in compliance synthesis.

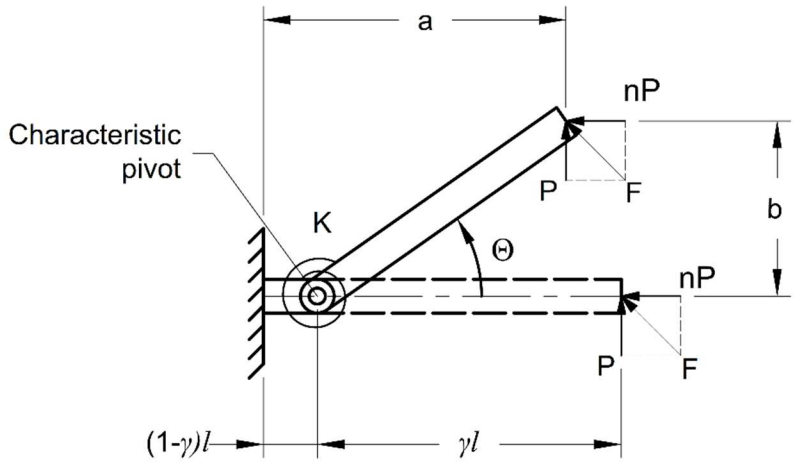

Figure 1.2 PRBM of Initially Straight Fixed-Free Beam

The PRBM approach is considered the most valuable and effective tool in designing, developing, and analyzing compliant mechanisms. The substantial advantage being its ability to convert a compliant mechanism into a rigid-body and vice versa. The PRBM also helps in synthesizing compliant mechanisms analytically to avoid the iterative and experimental process.

1.3. BACKGROUND HISTORY OF NONLINEAR SPRINGS

Non-linear force-deflection profiles are quite popular in several applications; one of such is constant-force mechanism design. The constant-force mechanisms are designed such that the force is zero at zero deflection, and with a small increase in deflection, the force increases rapidly and reaches a constant value. This force remains constant over a definite deflection range. Type synthesis of 28 possible constant-force slider mechanisms was performed by Murphy [22]. Howell et al. [23] performed the dimensional synthesis of six of these mechanisms. One such example of slider mechanisms is shown in Figure 1.3. Figure 1.4 represents the equivalent constant-force cam mechanism where the links are replaced by the toroidal cam surface [24]. Howell has also designed constant-force exercising equipment consists of a fixed-free beam instead of an SLFP [25]. Four versions of the cam follower constant-force mechanisms are synthesized and validated by Karthik [26]. Christian also validated one version of a fixed-free constant force mechanism [27]. Midha and Vamsi et al. [28] further hypothesized that a plain compliant segment or a rigid link with torsional spring generates a constant force under axial loading. Compliant springs are designed for an arbitrary non-linear force-deflection profile by Jutte and Kota [29,30].

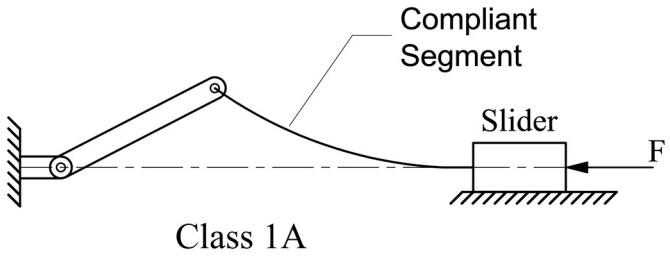

Figure 1.3 Constant-Force Slider Mechanism [23]

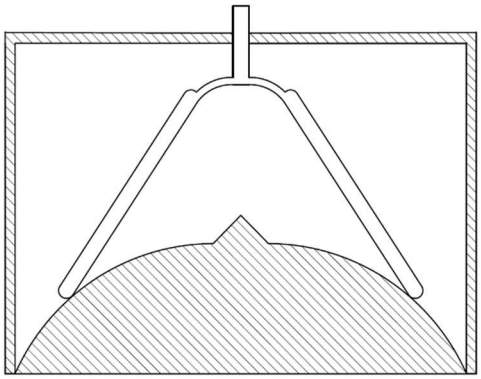

Figure 1.4 Constant-Force Cam Mechanism [24]

1.4. APPLICATIONS OF COMPLIANT MECHANISMS

There are numerous classic examples of compliant mechanisms in ancient tools such as the longbow and catapult [31]. These were the tools known as the tactical weapons used by human generations. In these tools, compliant members are drawn to store potential energy and provide the stored energy when released.

The Michelin Tweel Airless Tires [32], NASA mars rover wheels [33], and Adidas Springblade Shoes [34] also use a similar compliance energy storage function. Compliant fishhook remover, commercially known as compliers®, is a single-piece design equivalent to conventional metal fishhook remover. The compliers® are plastic

injection-molded parts that utilize the stored energy in the deformed flexible link. This tool is cheaper and advantageous than conventional metal design due to its simplicity and its not corrode with usage.

The compliant chair designed by Mettlach et al. [35] is another example. The chair mechanism legs are designed so that, when a load is placed on the seat, the compliant legs deform and store energy to allow the chair to recline to provide an ergonomic position to the user. The energy stored in the legs also helps the user while getting out of the chair. The numerous advantages of compliant mechanisms have helped develop several devices in a wide range of applications, such as MEMS (Microelectromechanical systems), including microactuators and microsensors, micro bistable mechanisms, and transmission systems, robotics, electrical connectors, etc. Compliant mechanisms also have significant applications in bio-medical devices. The flexible spinal disc replacement designed by peter et al. is one of many examples [36]. This flexible disc is made of titanium strips, and it is designed to provide the natural movement of the spine in any direction.

Figure 1.5 shows the BYU-developed spinal disc and its six flexures, which provide the device's motion in different directions. Flex-Foot Cheetah [37,38], a prosthetic foot replacement made from carbon fiber, is another example. This foot replacement not only helps disabled people in day-to-day activities; many people in amputee Paralympic runners also use it. Trocar surgical tool developed by Nikolai Begg [39] uses its flexible members to achieve precise motion during surgery. The constant force exercising equipment designed by Howell [25] is another example of successfully implementing a compliant mechanism in biomedical devices.

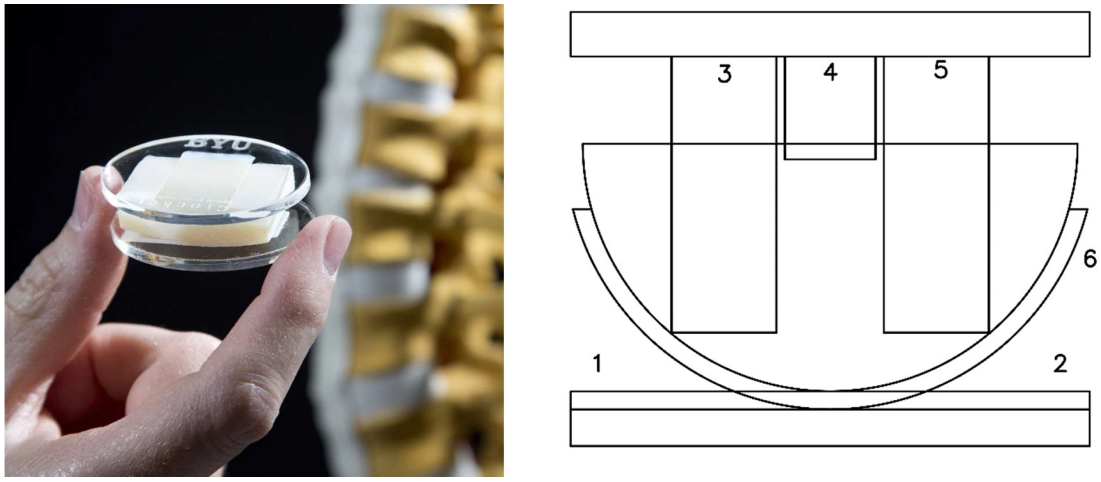

(a) (b)

Figure 1.5 Flexible Spinal Disc Replacement (a) Designed at BYU (b) Guiding Flexures of the Spinal Disc [36]

1.5. SCOPE OF INVESTIGATION

This research's main objective is to design and develop a variable resistance hand exerciser using a compliant cam-follower mechanism to generate the required force-deflection profile as an output. This is achieved by synthesizing a rigid cam profile, using material and geometrical properties of the compliant follower as an input. The current approach utilizes the force-deflection profile developed by experimental studies conducted on the human hand and a mathematical model that predicts the maximum grip force as a function of the handle's diameter based on real-world grip strength constraints. A methodology is then proposed to modify the mechanism for different force-deflection profiles. A novel PRBM approach is also presented to verify the interference of the cam surface with the followers during operation. The results are validated experimentally and using finite element analysis (FEA). Unlike the current state of art designs, the proposed design duly regards the hand's variable mechanical advantage characteristic in different

positions for a more natural feel over the device's full stroke. Without overstraining the hand in any operation position, it can be easily customized to meet individual needs. The present research is divided into nine sections.

Section 1 presents the introduction to the compliant mechanisms, their applications, and the development of compliant non-linear force-deflection mechanisms and current research.

Section 2 presents the introduction to human hand behavior and its grip strength constraints. The experimentation methods to generate the human hand's force-deflection profile with the discussion of the current state of hand exercisers' current state of art designs are explained. Advantages of current research over existing methods are presented.

Section 3 presents the analysis of the large deflection of a fixed-free beam with load at one end using the PRBM approach. Mechanism synthesis is also explained in this section.

Section 4 presents the effects of input parameters of compliant follower on the output force-deflection profile.

Section 5 presents the novel PRBM approach to calculate the deflected beam profile to check the interference of the follower with the cam surface. The validation of results with the FEA method is also discussed.

Section 6 presents the methodology to modify the mechanism for the required force-deflection profile.

Section 7 presents the experimental setup used to validate the synthesis approach along with the discussion of the results. The design of the hand exerciser prototype and design guidelines are taken into consideration.

Section 8 concludes the thesis with a discussion of future work.

This research aims to develop a hand exerciser that can avail people suffering from hand arthritis in their rehabilitation process. By considering the human hand's variable resistance behavior in the development of the exercising device, the conditions of overstraining the muscle and trouble to perform the complete stroke of an exerciser can be avoided. Also, the need for variable resistance hand resistance is evident because most of the existing designs use linear springs or elastomers to provide flexibility to the muscle.

2. INTRODUCTION TO HUMAN HAND AND GRIP STRENGTH

2.1. HUMAN HAND

In the words of Dr. Bryce Rutter: “Next to the human brain, the hand is the most fascinating and complex human organ [40].” Several joints in the hand and wrist work simultaneously to produce desired motion and forces. The majority of the day-to-day activities involve using hands [41]. However, the ease of performing activities involved in hand usage may be affected by injuries or illnesses, e.g., hand arthritis. Arthritis is described as one or more joints inflammation [42]. There are multiple reasons for the occurrence of arthritis, and it can affect many areas of the hand and wrist. This condition’s improper treatment could lead to deterioration of bones at joints, severe pain levels, and restricted joints motion. There are more than 100 forms of arthritis but many people struggling with two major types (i) osteoarthritis (ii) rheumatoid arthritis.

Osteoarthritis destroys the cartilage that protects the joints leading to bone deterioration by bones rubbing against each other. This results in damaging the bones and causing inflammatory symptoms in overtime a period [43]. Osteoarthritis develops at a later stage of life. Rheumatoid arthritis occurs due to the immune system’s malfunction, which attacks the joint protector synovial membrane leading to bone erosion. Unfortunately, there is no complete cure for this arthritis. The primitive treatment for arthritis is to control the pain levels and improvise joints’ mobility by using occupational and physical therapy [44]. Figure 2.1 illustrates the various joint conditions.

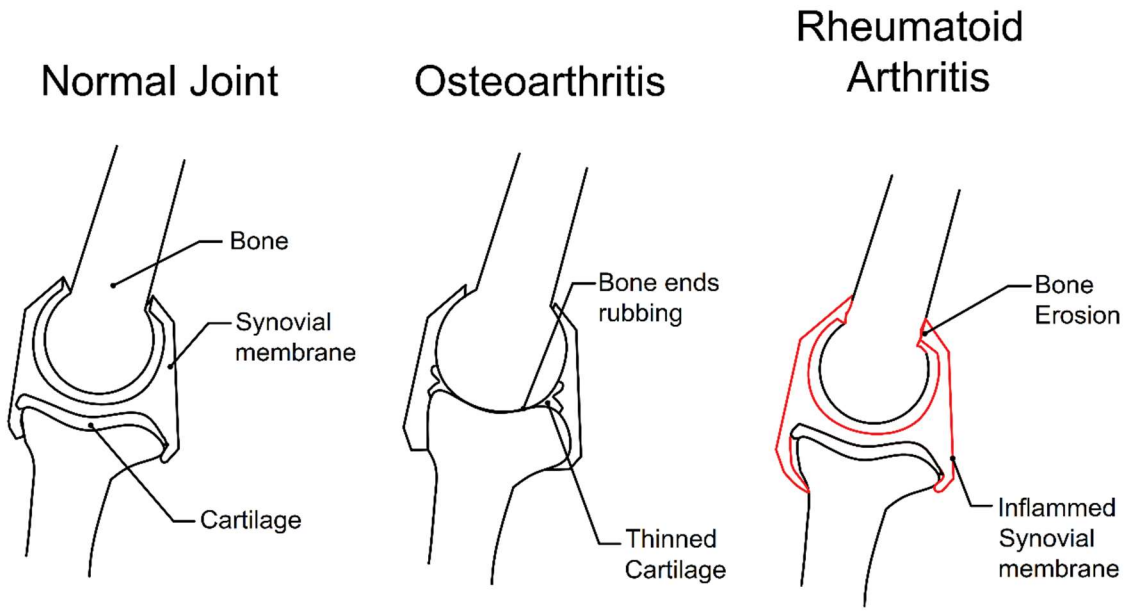

Figure 2.1 Joint Conditions: Normal Joint vs. Osteoarthritis vs. Rheumatoid Arthritis [44]

According to Health Day News article [45], more than 40% of people are afflicted by arthritis in at least one hand. The study was led by Jin Qin, based on 1990-2010 data on more than 2,200 people from North Carolina, aged 45 years or above. Osteoarthritis affected approximately 27 million American population, while 1.3 million Americans are prone to rheumatoid arthritis [44].

2.2. STATE OF THE ART

The available therapy methodologies include suggesting simple hand exercises [46, 47] or using various hand exercisers to enhance joint flexibility and alleviate pain levels. The details are discussed in detail further in this section. By performing exercises, the joint's muscles strengthen [48]. The movements in joints help in tendon flexibility and hand function by improvising the hand's motion range. According to [48,49], it

improves the production of the lubricating synovial fluid. This fluid acts as a nutrient supplier to the cartilage and also a shock absorber.

Some examples of simple hand exercises as presented in Figure 2.2 are involved in most therapy programs without using any exerciser are finger bends, forming a fist, thumb bends, making an ‘O’, finger lift, etc. [46]. Tendon glides, finger extension, proximal interphalangeal and metacarpophalangeal join extensions are a few other suggested exercises. Apart from exercises, arthritis pain is also treated by using heat or cold therapy [50]. The areas affected by swelling and pain are comforted by this. Heat therapy mainly helps in improving blood circulation to pacify the pain by relaxing the muscle. But one must be cautious about the heat levels and duration of application. Cold therapy, on the other hand, helps in reducing swelling and inflammation.

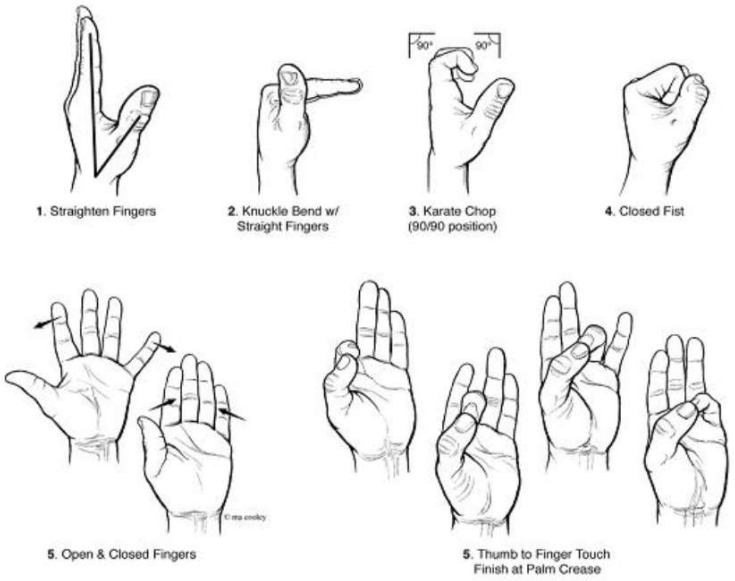

Figure 2.2 Physical Therapy Prescribed Hand Exercises [47]

Along with the simple hand exercises to improve the hand functionality and grip strength for arthritis people, several assisting devices are available. Hand grippers as shown in Figure 2.3 are distinctively designed to improve the gripping strength of the hand. These devices mainly consist of a linear spring attached to two handles. The resistance is provided from linear spring by moving the handles [51]. Thera-Band exercises are designed to give flexible motion to the hand fingers and forearm. These are made of squeezable non-toxic material available in different sizes and resistance levels. The available tension ranges from 3 lbs to 17lbs. Therapy Putty helps in providing motion to hands and fingers. The user molds the silicon-based putty material by hand. The different colors of the materials indicate different resistance levels. It is always suggested to perform the hand exercises with caution to avoid further injury or increase pain levels [51]. The putty claimed to maintain its resistance for one year. This product is also non-latex and unscented. The strength of the hand is provided by performing different squeezing actions [52]. The ultimate hand helper [53] is another example of a hand strengthener. This device's resistance is provided by using elastic bands on the adjustable hand frame, as shown in Figure 2.3. The hand Xtensor [54] developed by Healio health is designed to supplement hand interactions for gamers with heavy gaming devices. There are also hand exercising elastic bands, according to [55] was with different resistance levels to various user groups. The Digi-flex finger exerciser shown in Figure 2.4 mainly helps in improvising finger strength. This has five finger presses and has a tension range from 3 lbs to 8.5 lbs [56]. The exercise on this device is performed by placing the fingers in the loops, spreading and closing fingers by giving motion to all fingers and muscles. There are also different types of arthritis gloves [57] available to

give support and comfort to arthritis-affected hands. Fingertip gloves, wrist wraps, and heated gloves are few types of these. The open tip glove design helps the users perform day-to-day activities without any obstruction.

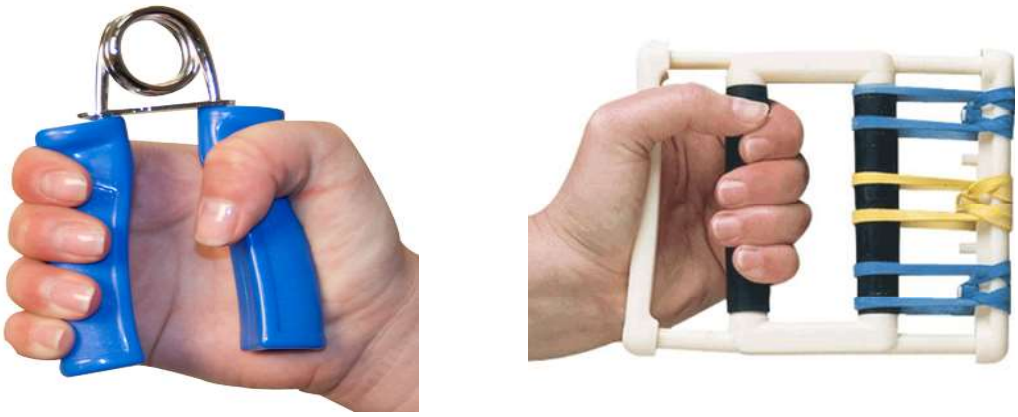

(a) (b)

Figure 2.3 Hand Exercisers: (a) Hand Grip Exerciser (b) Norco Hand Exerciser [51]

(a) (b)

Figure 2.4 (a) Digi-Flex Exerciser [55] (b) Thumb Exerciser [58]

The finger and thumb exerciser [58] shown in Figure 2.4 (b) is one more variety of exerciser designed to improve thumb strength. The rubber band provides resistance to the thumb on the top head of the exerciser.

2.3. HANDGRIP STRENGTH & MECHANICAL ADVANTAGE

The human hand is a complex structure comprised of many bones, joints, ligaments, tendons, and muscles. All of these components contribute to the flexibility, movements, and strength of the hand. The intricate structure of the hand made it challenging to effectively reproduce the features of the hand in robotic hands and grippers [59]. Investigating the biomechanical structure of the hand helps toward an understanding of the essential attributes that affect the functionality of the hand. It also helps provide better designs of hand related devices, to improve hand functionality and reduce the eccentric loading of joints and muscles. The crucial biomechanical features of the hand include bones, tendons (flexor and extensor), and joints.

2.3.1. Bones and Joints. The human hand is comprised of 27 bones that are connected by joints and ligaments [40], as presented in Figure 2.6. Every finger consists of 3 phalangeal joints known as distal interphalangeal (DIP), proximal interphalangeal (PIP), and metacarpophalangeal (MCP) joints except the thumb, which has only one distal interphalangeal joint. The joints are connected by ligaments that restrict the range of motion of the finger. Ligaments are fibrous tissue bands that connect two adjacent bones. The primary function of the ligament is to support the joint by providing stability and avoid bending it sideways. There is a total of 12 phalangeal joints in 4 non-thumb fingers, as shown in Figure 2.5.

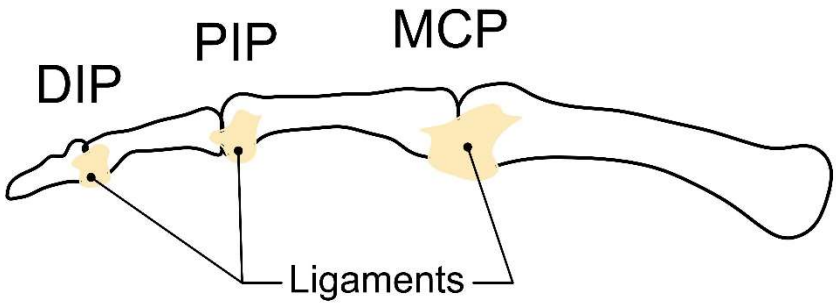

Figure 2.5 Ligaments of the Finger [59]

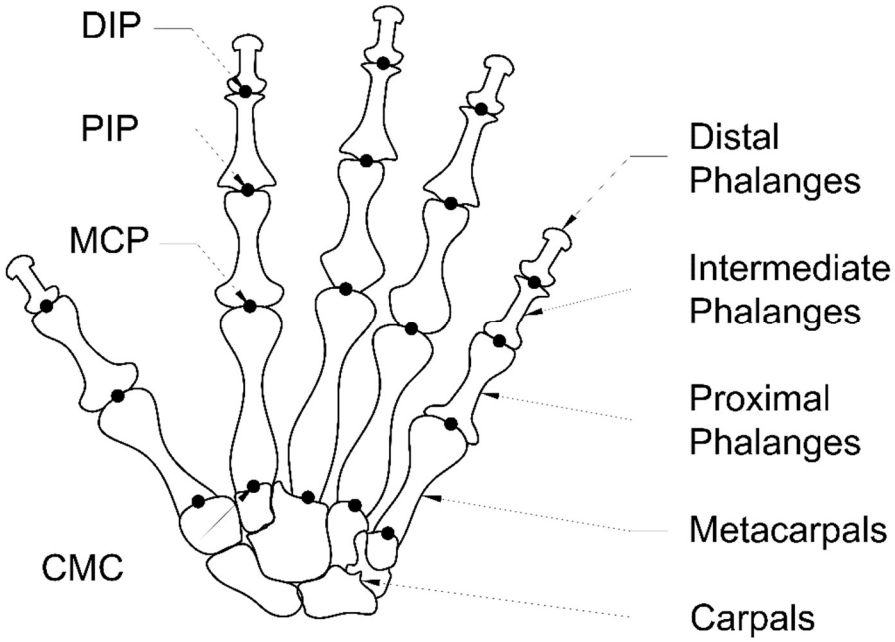

Figure 2.6 Human Hand Bones and Joints [59]

2.3.2. Tendons. There are two different varieties of tendons in the human hand: extensors and flexors. The extensor tendon helps in straightening the finger, and the flexor tendon helps in bending the finger [60]. The tendon is comprised of fibrous tissue that connects and transfers the force from the muscles to the bones. The motions of the

tendons originate from the muscle group in the forearm [61,62]. As shown in Figure 2.7, the extensor tendon starts from the wrist and branches out on the dorsal side of the finger. At the same time, the flexor tendons are on the palmar side of the finger traveling through the tendon sheaths [63,64]. The tendon sheaths are collagen-based fibrous tissues that act as elastic pulleys that wrap around the flexor tendons. This structure could undergo rupture and tear under intense flexion forces, e.g., rock climbing. The dexterity of the human hand can be greatly affected by the elasticity of the pulleys.

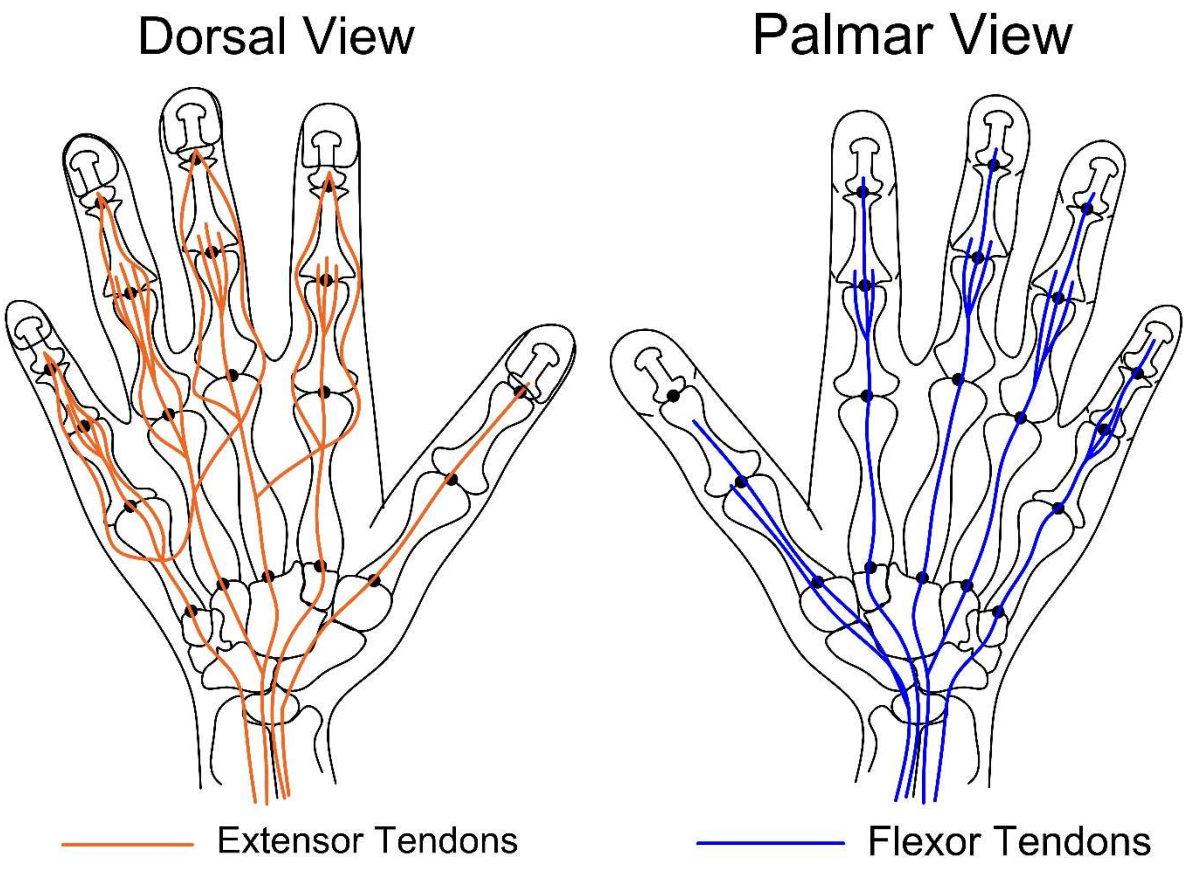

Figure 2.7 Tendons of Hand [59]

2.3.3. Mechanical Advantage. During gripping action [65], the human hand operates with a variable mechanical advantage situation because of its biomechanical features. The mechanical advantage of the hand varies from one position to the next in the hand gripping motion. In general, the mechanical advantage (MA) of a system is simply defined as the ratio of the output force (Fout) to the input force (Fin). The higher the mechanical advantage, the lower will be magnitude of the required input force is to generate a desired output force. On the other hand, the lower the MA, to generate a given output force Fout, a higher input force will need to be applied.

$$\text{MA} = \frac{F_{out}}{F_{in}} \tag{1}$$

In the four-bar mechanism, the mechanical advantage may be relatable to the transmission angle, Θ_T, i.e., the angle between the coupler and the follower (output) link as shown in Figure 2.8. The crank provides the input force, and the coupler transmits an output force on the follower link. The optimum transmission angle, $\Theta_T = 90^o$, for best transmission of force and motion to the output link. Similarly, the quality of mechanical advantage of the hand may be studied by trying to understand the elements involved in the gripping action. The muscles in the hand may be considered to serve as the actuators which supply the input forces through contractions due to electric charges [64,66-67], as shown in Figure 2.9. However, the input force is limited by the ability of muscle group contractions before overstraining [68]. This in turn limits the maximum gripping (output) force for a given position.

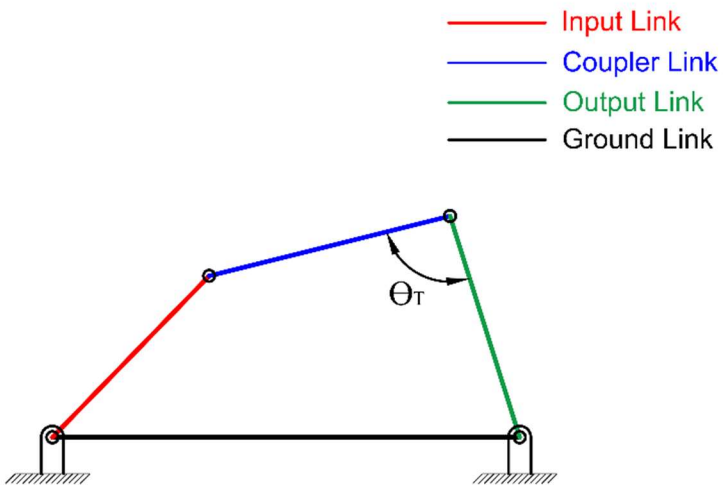

Figure 2.8 Transmission Angle Θ_T in Four-Bar Mechanism

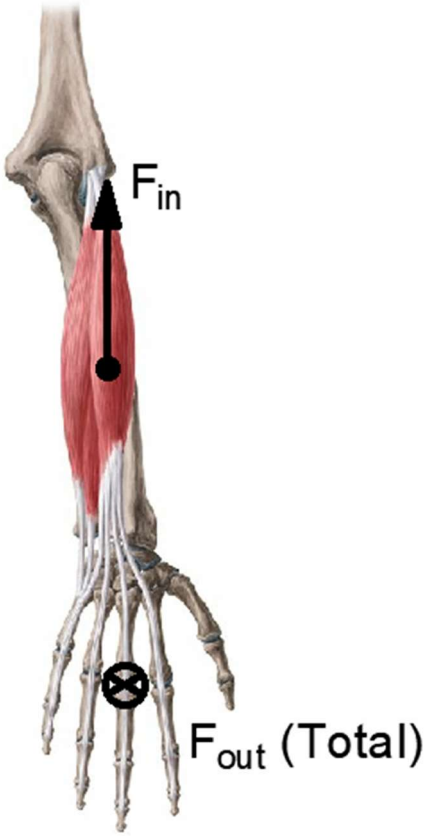

Figure 2.9 Forces in Human Hand [64]

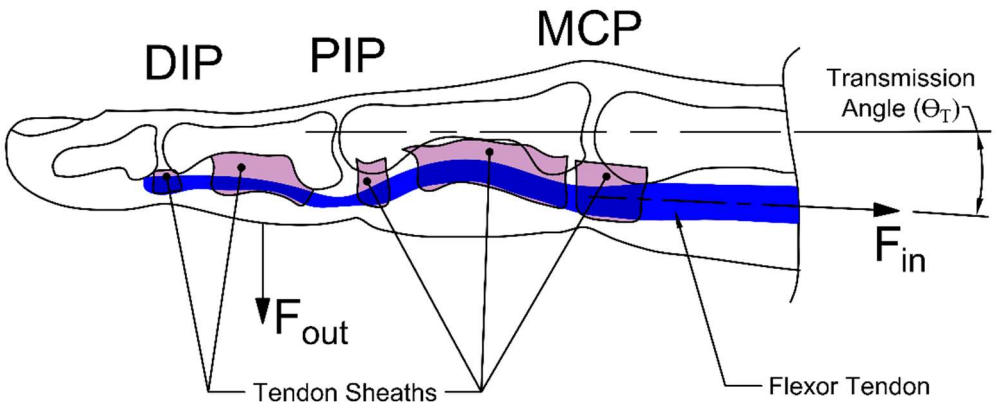

Figure 2.10 Biomechanical Structure of Hand Flexor Tendon [59]

The tendons of the hand act as a transmission system that effectively transfers the forces and motion to each finger during a gripping action. The forces in the tendons are measured as tension forces that affect the gripping forces, as observed in various studies [66,69-70]. In the human hand system, the transmission angle can be qualitatively evaluated as the angle between the flexor tendon and the finger during the gripping action, as shown in Figure 2.10. An experimental study [69] has also proved that the force transferred to the joints during a crimp grip (the fingertips are on the edge, e.g., edge of a mountain cliff, and the hand is hyper extended) is higher than the forces in slope grip (the fingertips are on the edge, e.g., edge of a mountain cliff, and hand is flexed). The tension forces in the tendons were reduced during both the scenarios, a more effective transfer of forces occurred for a larger transmission angle [69]. This may be easily explained; when the finger is straight, irrespective of how firmly the muscles contract, the output (gripping) force at the finger is always low due to the small transmission angle.

Figure 2.11 depicts the transmission angles for various gripping positions during the gripping action, which can be related to its mechanical advantage. The transmission angle ($\Theta_{T)}$, for a four-bar mechanism, is measured in between the coupler link and output link, as shown in Figure 2.8. In a human hand system, the flexor tendon can be considered as a coupler link transferring the force from the muscles to the finger (output link). Hence, the transmission angle in each gripping position can be measured between the flexor tendon and the finger. However, it is difficult to measure the angle between them accurately due to the complex structure of the hand. The tendon is connected to the finger by tendon sheaths that are attached to the phalangeal bones, as seen in Figure 2.10. One such connection between them is simplified and shown in Figure 2.11 as a characteristic contact – which is not a physical point of contact, but it is a location where the tendons are effectively pulling the finger during a gripping action. Since the tendon is not a linear structure, unlike the coupler link in four-bar mechanism, a tangent to the tendon is considered at the contact point. Similarly, a tangent line to the center axis of the finger at the contact point is also shown in Figure 2.11. The angle measured in between these two tangent lines is considered as the transmission angle, Θ_T, for a given gripping position. For accurate measurement of the transmission angles, an extensive study on the motion and force transmission between the tendons, tendon sheaths, ligaments, and phalangeal bones of the finger is required. For a simple and rudimentary treatment, the tendon sheaths and ligaments are not included nor shown in the Figure 2.11. In reality, each finger contributes to the total hand gripping force and helps to define a “component mechanical advantage.” These component mechanical advantage values help define and

limit the net mechanical advantage [71] of the hand system. This is not investigated in the current research study.

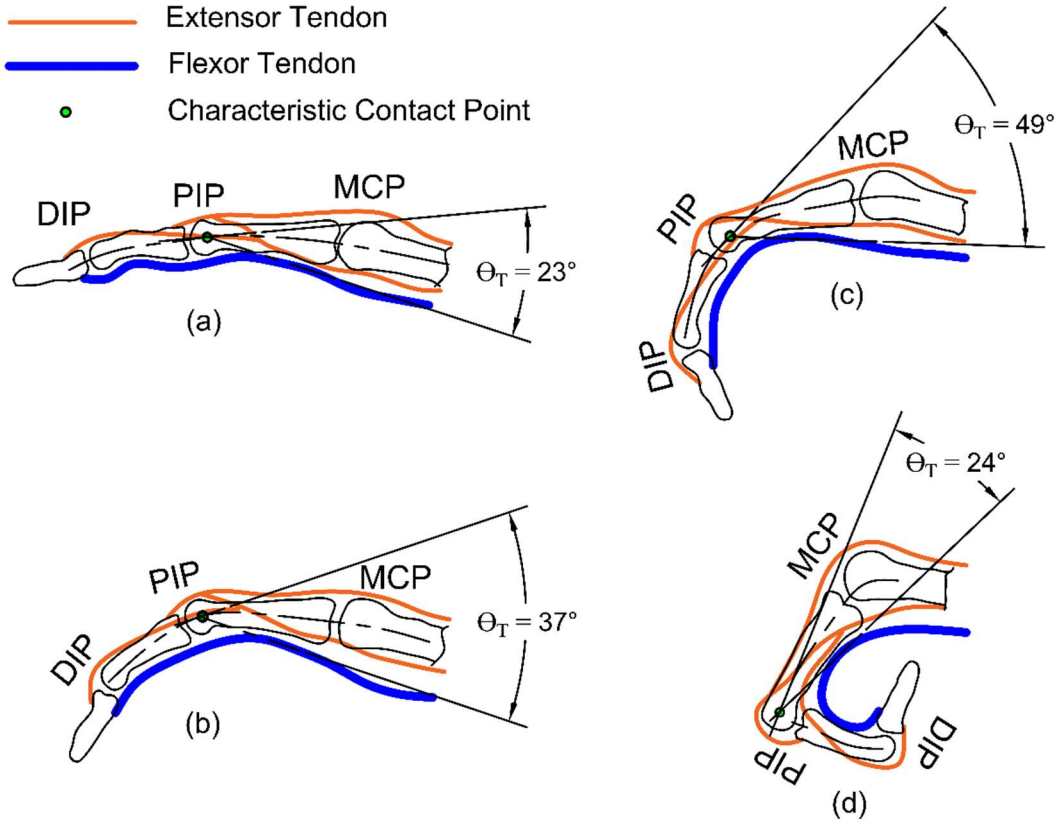

Figure 2.11 Transmission Angle Θ_T at Various Hand Positions [59]

2.3.4. Gripping Strength. The force distribution of the hand is greatly dependent upon the index, middle, ring, and little fingers' phalangeal joints. The sum of forces exerted by all non-thumb fingers during a gripping action is considered as the gripping force or gripping strength of the hand [42]. To measure the percentage contribution of these phalangeal joints, several experimental studies have been performed. The results are used to compose the force profile of the hand. Designing a hand exercising device

using such data will significantly help people in the rehabilitation process and improve muscle flexibility, since the design already considers the force limitations of the hand to avoid the overstaining of the muscles.

The present research uses the force-deflection profile of the human hand developed by Freund et al. [42]. Their analysis is based on the experimental studies conducted by Amis [72], where in the maximal forces are reduced when the handle diameter is increased from 3.1 cm to 12 cm. Experiments were performed on 17 subjects with 6 different cylinder diameters in 4 sets. The shear and normal forces at each phalangeal joint of 4 non-thumb fingers are measured on different cylinder diameters. The average force of each finger on each cylinder is calculated.

The hand's gripping force is modeled as the function of handle diameter and size of the handle. However, the data is also verified by a grip test on 10 right-handed subjects. The mathematical model and force-deflection curve are established by using the 24 data statistics generated by Amis. The model equation considered the constraints of real-world grip strength. If we use the data generated by Amis is directly used, there will be 4 different sets. But for the force-deflection profile single reliable model is required. By using the dimensional analysis, Freund et al. reduced the number of the variables in the experiment to express the data in 1 set consists of 24 data points. An assumption is made that longer finger better grips larger diameters to minimize the variables. But to avoid using two variables, cylinder diameter and finger length, the term relative diameter, a ratio of cylinder diameter to finger length is introduced. Using this dimensionless ratio on the x-axis, the 4 sets of 6 data points are expressed as 1 set of 24. The data is curve fitted, as shown in Figure 2.12 with an average force on the y-axis. The curve trend also

proves the assumption of Freund et al. of finger length and cylinder diameter. The Equation 2, the maximal grip force is developed by using non-linear least-squares fitting.

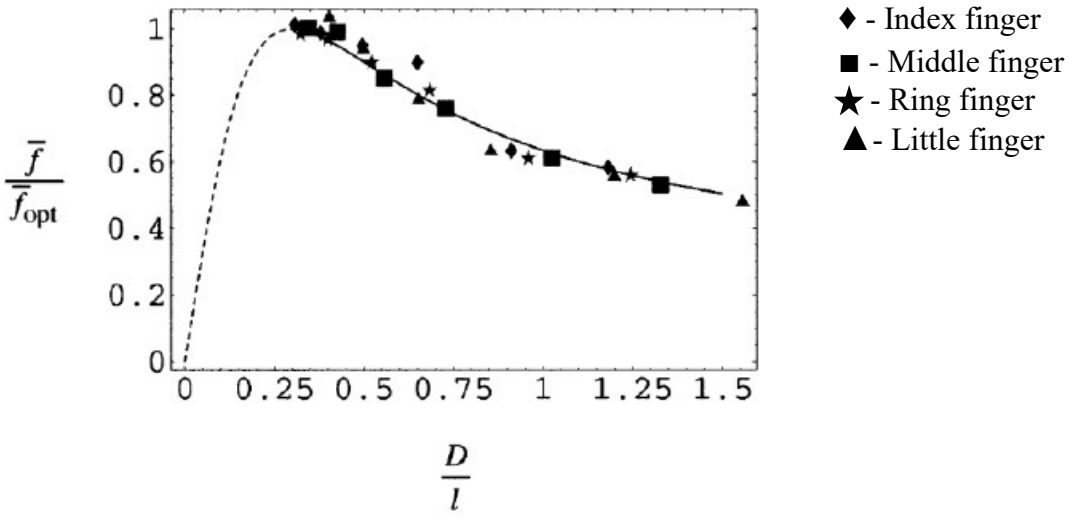

Figure 2.12 Freund et al. Function Fit to Experimental Data [42]

$$\frac{\bar{f}}{\bar{f}_{opt}} = \varepsilon \frac{\varepsilon\delta + 2(1-\delta)}{\varepsilon^2 + 1 - \delta} \tag{2}$$

where the parameter values are found to be $\delta = 0.11$, $\varepsilon = \frac{k}{0.27}$; $k = \frac{D}{l}$

l length of the middle finger

D handle diameter

f grip force

f *maximal grip force*

k *relative cylinder diameter*

By observing different experimental results, it is evident that the grip strength is decreasing with handle diameter. But smaller handle diameters further result in lower

gripping forces. The optimum handle diameter will provide better gripping strength to the user. The force distribution can vary due to the change in surface area of contact between the object and the hand, and also due to the change in the transmission angle in various positions. As depicted in Figure 2.11, the transmission angle increases from an open grip position to a slightly closed grip position, and then decreases again until a nearly closed grip position. This supports the findings of Freund et al., and Radhakrishnan et al., [42,72-74], of achieving the optimum gripping forces for optimum cylinder diameters. It is also observed that the percentage contribution of individual finger forces to the gripping strength remains unaffected with a change in handle diameters [73,74].

2.4. ADVANTAGES OVER PRIOR ART

Most of the hand exercisers discussed in the state-of-the-art Section 2.2 provide resistance using springs. The springs are linear force-deflection profiles, where the output resistance is linearly proportional to the deformation [51]. The other exercisers use elastomers or rubbers to provide non-linear resistance [51]. However, none of the exercisers accommodate the resistance capacity of the hand in different positions. This leads to a harmful situation for the hand. In resistance training, the common problem is strength, not equivalent to resistance. When the force-deflection profile of the resistance exceeds, the strength is called a “sticking point” [75]. At these points, the full stroke of exercise cannot be complete with ease because the resistance is high, and it may exceed the user’s maximum strength [76]. In the words of Komi, “the idea of accommodating resistance is to develop maximal tension throughout the complete range of motion.” The possible solutions to this problem are by using isokinetic machines or variable resistance

machines [77]. Isokinetic machines are controlled electronically to change the resistance at a constant rate of motion. The user specifies the training velocity. During the positive acceleration, the machine's resistance goes high, and during the negative acceleration, the resistance goes low. The isokinetic machine is confirmed to zero acceleration and specified training velocity while performing the exercise. As a result, the maximum force is exerted throughout the motion. The isokinetic machines are often very expensive and mostly used in high-speed applications such as kicking [78].

The variable resistance exercise machines exert resistance with varied forces throughout the stroke of exercise. These machines are designed to have a force-deflection profile of the specified joints. These machines are designed for an average population, unlike individual user-specific [79]. Providing a balanced resistance at each deflection to match with the joint's strength is the main aim of a variable resistance exerciser [75]. This kind of machine is beneficial to older people by providing the capability to perform the full range of motion by applying resistance [80].

Unlike the state-of-the-art exercisers discussed in Section 2.2, the current research is focused on designing and developing a variable resistance hand exerciser to provide a natural motion to the hand throughout the range of motion by generating the force-deflection profile of the human hand as an output. This variable resistance hand exerciser also helps in the rehabilitation process by avoiding the risk of injury by not over straining the muscle. It also comes with added advantages associated with the compliant mechanism, such as a low number of components, less weight, low cost and ease of specialization and easy maintenance.

3. INTRODUCTION TO MECHANISM SYNTHESIS

3.1. BACKGROUND OF LARGE DEFLECTION ANALYSIS

In any traditional structural system, flexibility and deflections are avoided to improve the stability of the system. For example, flexibility in high-speed mechanisms might create vibrations in the system leading to mechanical failure. Even in structures like bridges, the deflections are always undesirable for structural stability. The kinematic analysis of rigid mechanisms always considers that the links are rigid, and deflections are very small. This assumption is valid in most structural applications where the stress limit is below the elastic limit. These small deflections can be solved by linear equations. However, compliant mechanisms rely entirely on their members' deflections, and these deflections are large deflections in nature that cannot be solved using linear equations. In this section, a quick review of small deflection and large deflection analysis is discussed. While designing a structure, generally, the force is known, and the structure's displacement due to the force is calculated. But in designing a compliant mechanism, the displacement boundary conditions are often known, and force is calculated.

Consider a fixed free beam, as shown in Figure 3.1, with an end force F, and the small deflection can be calculated using Equation 3. The *E, I,* and *L* are constants from the geometrical and material properties of the beam. The Equation 3 is a linear equation. However, Equation 3 is derived from the assumption that the deflections are small. The equation is derived from the Bernoulli-Euler equation that bending moment is proportional to the curvature of the beam.

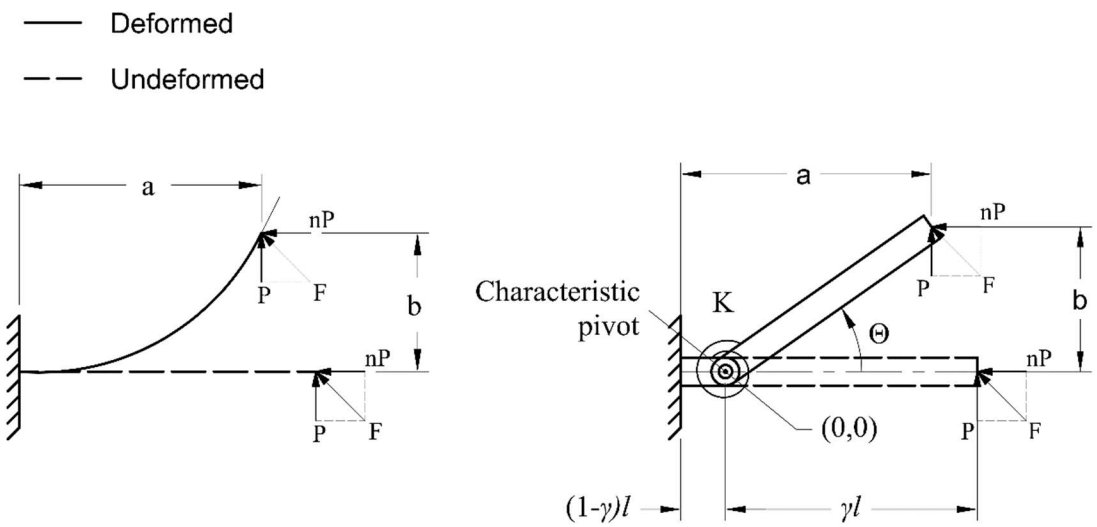

Figure 3.1 Fixed-Free Beam with Force at the Free End

$$\delta = \frac{PL^3}{3EI} \tag{3}$$

where,

$$I = \frac{bh^3}{12} \tag{4}$$

$$M = EI\frac{d\theta}{ds} \tag{5}$$

$$\frac{d\theta}{ds} = \frac{{}^{d^2\delta}/_{dx^2}}{\left[1+\left({}^{d\delta}/_{dx}\right)^2\right]^{3/2}} \tag{6}$$

$$\frac{d\theta}{ds} \approx \frac{d^2\delta}{dx^2} \tag{7}$$

$$\frac{P(L-x)}{EI} = \frac{d^2\delta}{dx^2} \tag{8}$$

$$\frac{P}{EI}\int_0^L \int_0^L (L-x)dx^2$$

$$= \int_0^L \int_0^L \frac{d^2\delta}{dx^2} dx^2$$

$$\frac{PL^3}{2EI} - \frac{PL^3}{6EI} = \delta \tag{9}$$

which results in Equation 9.

But for large deflection, the slope of deflection cannot be considered small so,

$$\frac{P(L-x)}{EI} = \frac{{d^2\delta}/{dx^2}}{\left[1 + \left({d\delta}/{dx}\right)^2\right]^{3/2}} \tag{10}$$

To solve the large deflections, elliptical-integral solutions can be used, which is a very complicated process. But the results are considered accurate, and this method is regarded as the standard method to compare against other alternative methods. Other alternatives approach like Chain algorithm and FEA, can be used to solve the forces for large deflections. But PRBM is considered the most simple and effective approach to work.

The PRBM considers the spring stiffness of the compliant members and provides accurate models for the large deflections. Figure 3.1 shows the PRBM of a fixed-free compliant segment with force at the free end. The PRBM uses the idea of elliptical-integral equations of large deflections, which shows that the free end of a cantilever beam with force at that end follows an approximately circular path. This assumption is used in developing the deflected path of the beam. The PRBM of a flexible beam is represented

as two pinned rigid links. At the pin-joint, a torsional spring is added to show the beam stiffness. This pin joint is called a characteristic pivot. The empirical relation between parameters of link length and spring stiffness is defined [13]. The parameters' accuracy is validated to be 0.5% error up to 58.5 degrees [31]. PRBM method is considered as the simple tool for designers compared with FEA and elliptic integral method. PRBM has demonstrated an efficient way of accommodating large deflections in different applications accurately. PRBM approximates the compliant beam as rigid links, which helps the designer to use the same approach of rigid body mechanics

3.2. PRBM OF FIXED-FREE BEAM WITH A FORCE AT THE FREE END

Figure 3.1 shows a fixed free compliant segment of length L, elasticity E, with a moment of inertia I. The beam is subjected to an end load P at angle Θ. The PRBM has two critical parameters: characteristic radius factor γ and load factor n. The length of rigid links depends upon the value of radius factor γ, and the shorter link length is l (1-γ), the length of the longer link is γl. Below equations are used to estimate γ for different n values.

for ($-4 < n < -1.5$)

$$\gamma = 0.855651 - 0.016438n \tag{11}$$

for ($-1.5 < n < -0.5$)

$$\gamma = 0.852138 - 0.018615n \tag{12}$$

for (-0.5 < n < 10)

$$\gamma = 0.851892 - 0.020805n + 0.005867n^2 - 0.000895n^3 + 0.000069n^4 - 0.000002n^5 \quad (13)$$

As shown in Figure 3.1, the axial component of the force is denoted by nP, and the transverse force is P. the load factor n is defined as the ratio of the axial to transverse force. Load factor n is positive for positive compressive axial force. n is also depending upon the angle of applied force Θ.

The torque at the characteristic pivot is

$$T = K.\Theta \quad (14)$$

where,

$$K = \gamma K_\Theta \frac{EI}{L} \quad (15)$$

The value of K_Θ is estimated as follows [81]:

for -4 < n < -1.5

$$K_\Theta = 2.66041 - 0.069005n - 0.002268n^2 \quad (16)$$

for -0.5 < n < 10

$$K_\Theta = 2.648834 - 0.074727n + 0.026328n^2 - 0.004609n^3 + +0.000390n^4 - 0.000013n^5 \quad (17)$$

The axial deflection of the beam end is denoted as *a,* and the transverse deflection of the beam end is *b*. The values a and b are calculated by trigonometry relation, as shown in Figure 3.1:

$$a = l[1 - \gamma(1 - cos\Theta)] \quad (18)$$

$$b = \gamma l sin\Theta \quad (19)$$

Similarly,

$$\Theta = \tan^{-1}(\frac{b}{a - (1 - \gamma)l}) \quad (20)$$

3.3. MECHANISM SYNTHESIS

The current research utilizes the cam-follower synthesis methodology proposed by Kyle [82]. In this section, a review of the mechanism synthesis is provided. The cam-follower mechanism consists of a compliant fixed-free beam with a rigid radius at the free end and a rigid cam surface. The fixed end is fixed to a slider, and the free end is free to move on the cam surface. Figure 3.2 depicts the PRBM of the mechanism. The mechanism is displaced with an input displacement D_{in} during operation, with the origin of the mechanism being at the characteristic pivot. The rigid cam constrains the angular displacement of the compliant beam. The rigid cam surface is synthesized using three

static equilibrium and four kinematic equations of the PRBM. The static equilibrium equations include the sum of moments, the sum of X-forces, and the sum of Y-forces on the follower, as shown in Figure 3.3.

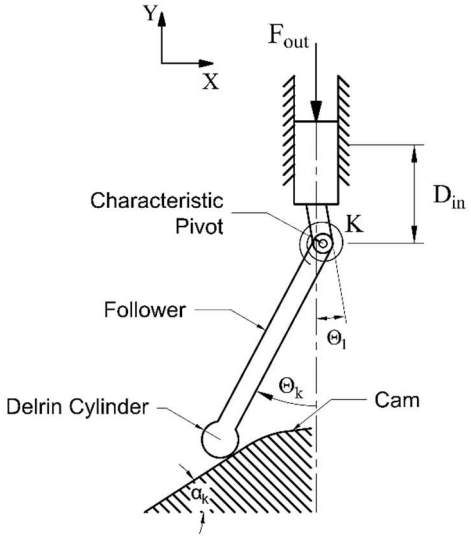

Figure 3.2 PRBM of the Mechanism

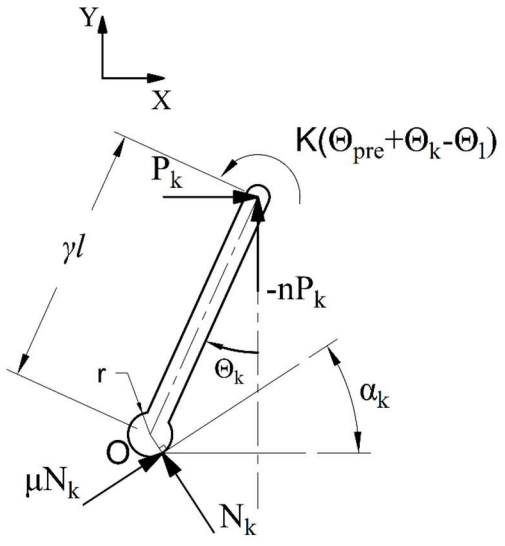

Figure 3.3 Free-Body Diagram of the Mechanism

To ensure a continuous smooth surface of the cam surface for the flexible beam movement, the cam surface is modeled as a spline curve. The total cam surface is divided into multiple spline curves, and each curve is synthesized using the following equations. All the curves are joined together for the given input displacement to create the required cam surface. The kinematic equations include the equations of the quadratic spline curve and its first derivative at node k-1 and node k for the k-1 element, as shown in Figure 3.4.

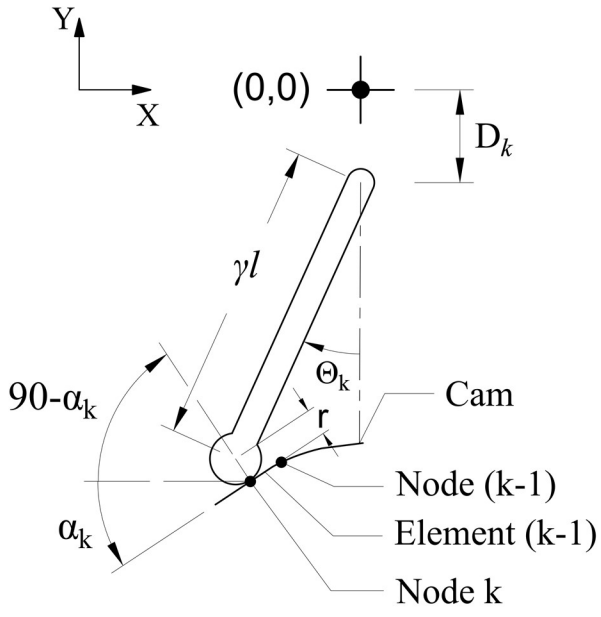

Figure 3.4 Kinematic Diagram of the Mechanism

The static equilibrium equations are as follows:

$$\Sigma M_0 = 0$$

$$\gamma K_\Theta \frac{EI}{l}(\Theta_k - \Theta_1) + (-n_k P_k)[\gamma l sin(\Theta_k) - r sin(\alpha_k)] - (P_k)[\gamma l cos(\Theta_k) + r cos(\alpha_k)] = 0 \quad (21)$$

$$\Sigma F_X = 0$$

$$\mathrm{P_k} + \mu \mathrm{N_k} \cos(\alpha_\mathrm{k}) - \mathrm{N_k} \sin(\alpha_\mathrm{k}) = 0 \tag{22}$$

$$\Sigma F_Y = 0$$

$$(-n_k P_k) + \mu N_k \, sin(\alpha_k) + N_k \, cos(\alpha_k) = 0 \tag{23}$$

The kinematic equations are as follows

Loop closure at node k-1:

$$\begin{aligned} A_{k-1} + B_{k-1}[rsin(\alpha_{k-1}) - \gamma lsin(\Theta_{k-1})] \\ + C_{k-1}[rsin(\alpha_{k-1}) - \gamma lsin(\Theta_{k-1})]^2 \\ = -\gamma lcos(\Theta_{k-1}) - rcos(\alpha_{k-1}) \\ - D_{k-1} \end{aligned} \tag{24}$$

The slope of cam at node k-1

$$\begin{aligned} B_{k-1} + 2C_{k-1}[rsin(\alpha_{k-1}) - \gamma lsin(\Theta_{k-1})] \\ = tan(\alpha_{k-1}) \end{aligned} \tag{25}$$

Loop closure at node k:

$$\begin{aligned} A_{k-1} + B_{k-1}[rsin(\alpha_k) - \gamma lsin(\Theta_k)] \\ + C_{k-1}[rsin(\alpha_k) - \gamma lsin(\Theta_k)]^2 \\ = -\gamma lcos(\Theta_k) - rcos(\alpha_k) - D_k \end{aligned} \tag{26}$$

The slope of cam at node k:

$$\begin{aligned} B_{k-1} + 2C_{k-1}[rsin(\alpha_k) - \gamma lsin(\Theta_k)] \\ = tan(\alpha_k) \end{aligned} \tag{27}$$

The above equations are used in the synthesis, including the prescribed force-deflection profile parameters, flexible beam geometrical and material properties, and PRBM parameters. The design table presented below shows the total number of variables used in the synthesis, along with its source information.

Table 3.1 Design Table

Number of variables	**Variable Names**	**Source**
3	P_k, D_{k-1}, D_k	Force-deflection function
6	E, I, l, Θ_{pre}, Θ_1, μ	Compliant follower dimensions & materials
2	γ, K_Θ	PRBM parameters
2	Θ_{k-1}, α_{k-1}	From the previous node solution
7	Θ_k, n_k, N_k, α_k, A_{k-1}, B_{k-1}, C_{k-1}	Solved with Equations 21-23 and 24-27
Total: 20		

The first set of Equations from 21-23 are solved for k=1, and resultant Θ_1 and alpha1 are used to solve Equations 21-27 for k=2. This process can continue until k = k_{max} is achieved for total k_{max}-1 elements. By giving initial element position information, the remaining elements are solved for the given respective displacement.

4. STUDY OF INPUT VARIABLES

As mentioned in Section 3.3, the proposed cam-follower mechanism synthesis method utilizes the compliant follower geometrical properties as input to generate the required force-deflection profile. The beam length, width, and thickness cannot be provided arbitrarily because these values significantly affect the resultant cam profile. The dimensions of the cam, in turn, can affect the overall size of the hand exerciser. To achieve an optimized hand exerciser design with optimum size and weight, understanding input variables' effect is helpful. Additionally, this will also help customize the design for individual users.

The variation of the resultant cam profile for a given force and travel value of 1.5 inches and 1.4 inches is studied by changing the input variables. The initial variable values are shown in table 4.1. These values are changed gradually, and the synthesized cam profiles are compared. The effect of variables is also studied for the resultant force-deflection profile.

Table 4.1 Initial Input Variables

Variable	**Value**
L	2 in.
w	0.6 in.
t	0.015 in.

4.1. VARIATION OF LENGTH

The initial value of the beam length is 2 inches. For every iteration, the parameters width and thickness are maintained constant by changing the length value. It is observed that by increasing the beam thickness, the resultant cam profile width is increased, and the steepness is decreased. By reducing the beam length, the resulting cam profile's steepness is increased, resulting in less width. The resultant cam profiles are compared with initial length value of 2 inches in the below Figure 4.1.

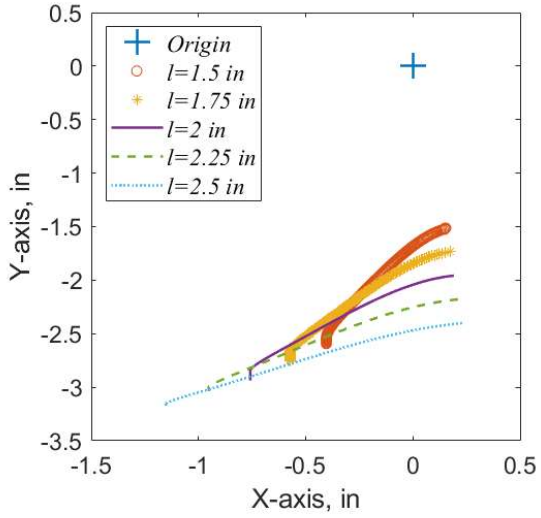

Figure 4.1 Cam Profiles Compared with Variation in Length

4.2. VARIATION OF WIDTH

The initial value of the width is 0.6 inches. For every iteration, the parameter's length and thickness are maintained constant by changing the width value. It is observed that the resultant cam profile width is decreased by increasing the beam width, and the steepness is increased. The resulting cam profile's steepness is reduced by reducing the beam width, resulting in a wider cam profile. The resultant cam profiles are compared

with an initial width of 0.6 inches in the below Figure 4.2. However, the change in width resulted in cam profiles whose initial co-ordinates remained the same.

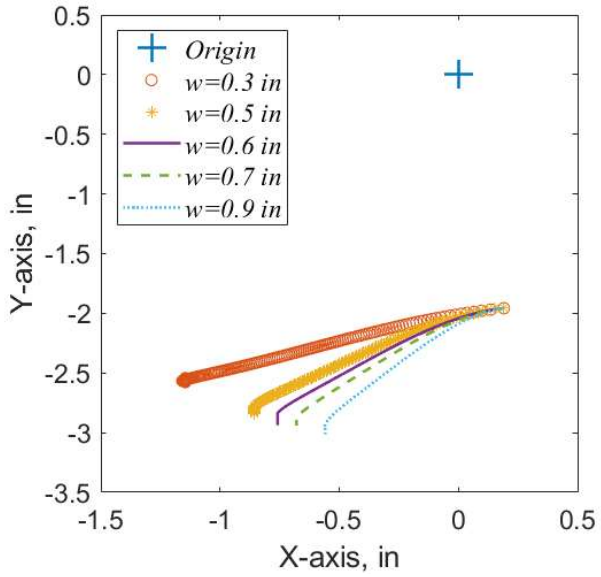

Figure 4.2 Cam Profiles Compared with Variation in Width

4.3. VARIATION OF THICKNESS

The initial value of the thickness is 0.015 inches. For every iteration, the length and width are maintained constant by changing the thickness value. It is observed that the resultant cam profile width is decreased by increasing the beam thickness, and the steepness is increased. By reducing the beam thickness, the resultant cam profile's steepness is reduced, resulting in a deformed wider cam profile. The resulting cam profiles are compared with an initial thickness of 0.015 inches in the below Figure 4.3. However, for various thickness values, the resulted in cam profiles have the same initial co-ordinates.

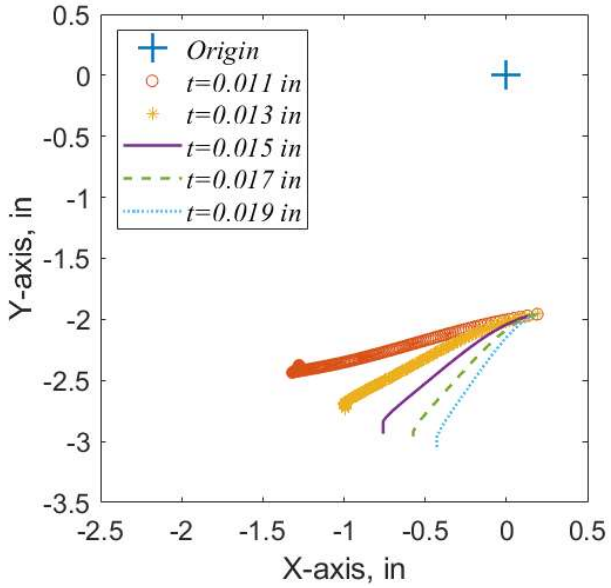

Figure 4.3 Cam Profiles Compared with Variation in Thickness

From the above iterations, it is noted that changing beam length affected the overall height and width of the cam profile. The beamwidth did affect the cam profile majorly in the overall width, but its overall height remained the same. Beam thickness affected the cam profile's width radically, but the height of the cam remained the same for all values.

The effect of variables on the resultant force-deflection profile is investigated. The change in length and width did affect the resulting force-deflection profile at the end of the stroke majorly. The overall profile, however, remained the same as prescribed. But varying the thickness has affected the beginning and end of the stroke.

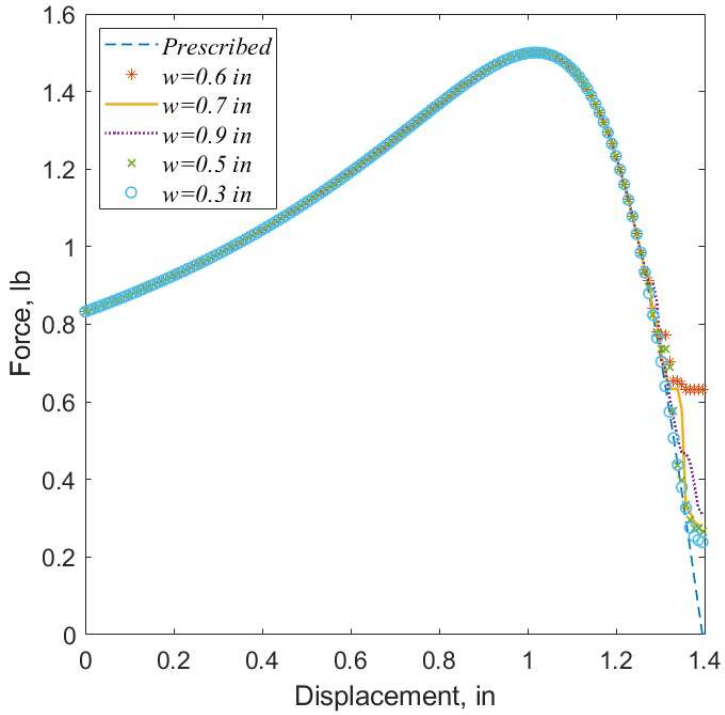

Figure 4.4 Force-Deflection Profile variation with varying Width

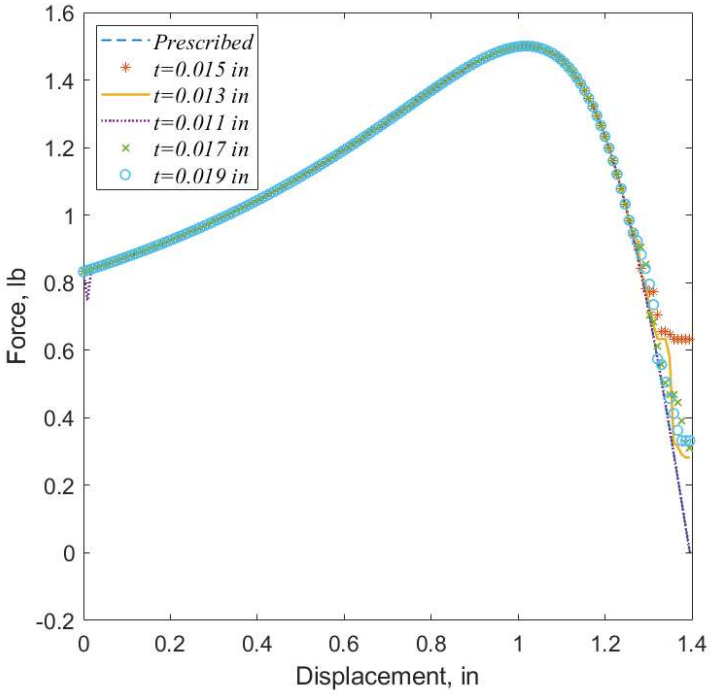

Figure 4.5 Force-Deflection Profile variation with varying Thickness

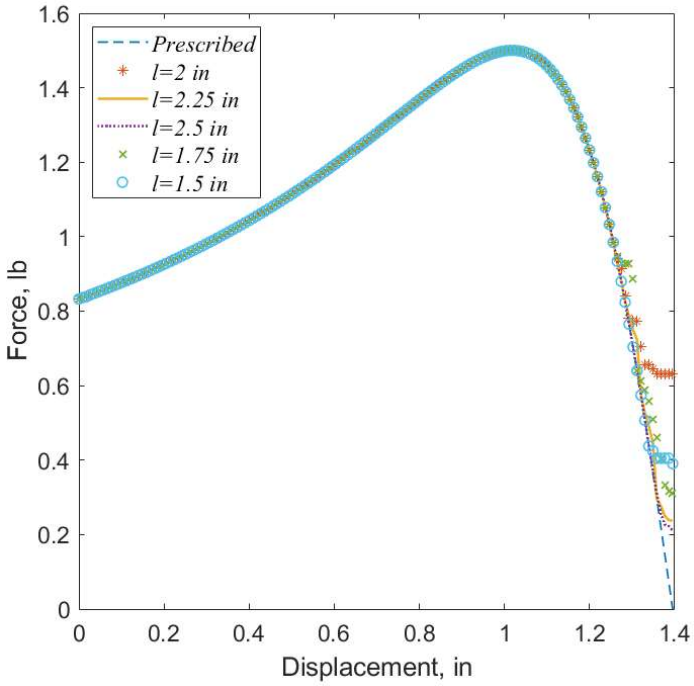

Figure 4.6 Force-Deflection Profile variation with varying length

5. PRBM APPROACH TO VERIFY THE BEAM INTERFERENCE ON CAM

In the proposed cam-follower mechanism, the compliant fixed-free beam with a rigid radius at one end is designed to travel on the rigid cam surface without contacting it during the travel. If the flexible beam's body interferes with the cam surface during the operation instead of a rigid radius, the mechanism cannot be operated throughout the entire stroke. Also, it makes the PRBM model developed for the mechanism (shown in Figure 3.2) obsolete. This also affects the resultant force-deflection profile. Considering the adverse effects, the follower interference with the cam surface is examined. One way to review the deflected beam positions during the operation is by using the FEA approach. This process is cumbersome and time-consuming, which is explained in detail in Section 5.3.

A new method of calculating the deflecting beam profile is proposed in this thesis. This method utilizes the PRBM approach of calculating the radius of curvature value in estimating the deflected beam profiles. The deflected beam end co-ordinates are computed using a simple PRBM model, and the co-ordinates are transferred accordingly to calculate the radius of curvature of the beam. The radius of the curvature value of a beam is considered as the initially curved beam's radius value. The same value can be used to find the deflected beam profile because "the deflected path of a flexible cantilever beam with force at one end follows an approximately circular path with some radius along the beam length" [31]. In the proposed cam-follower mechanism, the fixed-free compliant follower is displaced at a fixed end. This results in varied fixed local co-ordinates for every input displacement. The radius of curvature value is calculated for

every given input displacement. The obtained beam end co-ordinates and deflected beam profiles from the PRBM approach are compared with the results from the FEA approach.

5.1. RADIUS OF CURVATURE APPROACH

In [31] radius of curvature approach, the deflected beam end co-ordinates are considered as the co-ordinates of the initially curved fixed-free flexible beam, as shown in Figure 5.1. A nondimensionalized parameter value k_o is defined, which is the ratio of the length of the beam to its radius, as shown in Figure 5.2. It is assumed that the flexible beams are thin, and their neutral axis is at the centroidal axis. By using the k_o value the initial beam end x and y co-ordinates a_i, b_i are calculated using the Equations 29 & 30 below.

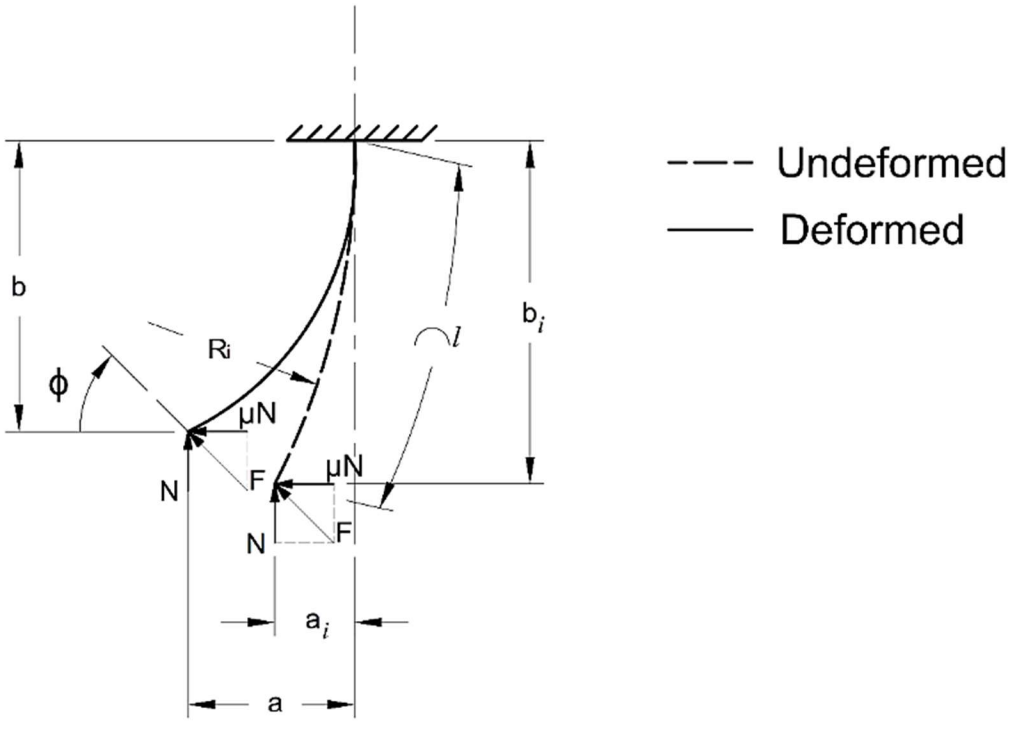

Figure 5.1 Initially Curved Fixed-Free Beam

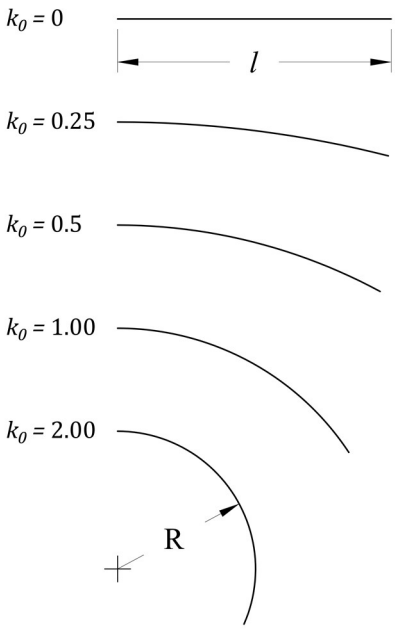

Figure 5.2 Beam Shapes for Various k_o Values

$$k_o = \frac{l}{R} \tag{28}$$

$$\frac{a_i}{l} = \frac{1}{k_o} sink_o \tag{29}$$

$$\frac{b_i}{l} = \frac{1}{k_o}(1 - cosk_o) \tag{30}$$

However, the deflected beam end co-ordinates are calculated as discussed in Section 3.2 by using Equations 18 & 19. For calculating the deflected beam profile using the PRBM approach, a reverse approach is utilized. The deflected beam end co-ordinates are calculated for the initial orientation, as shown in Figure 3.1 using Equations 18 & 19. These co-ordinates are then transformed accordingly to make sure the beam's orientation in Figure 3.1 is the same as in Figure 5.1. Where the origin is at the fixed end and the

beam is initially straight. The transformed co-ordinates are used as the initial co-ordinates of the curved beam in the Equation 29 or 30 and solved for k_o. Using this k_o in Equation 28, the radius of curvature value is calculated. This value is used as the radius of the deflected beam along its length. This radius value is calculated for each input displacement, and corresponding deflected beam orientation is concluded based on this value.

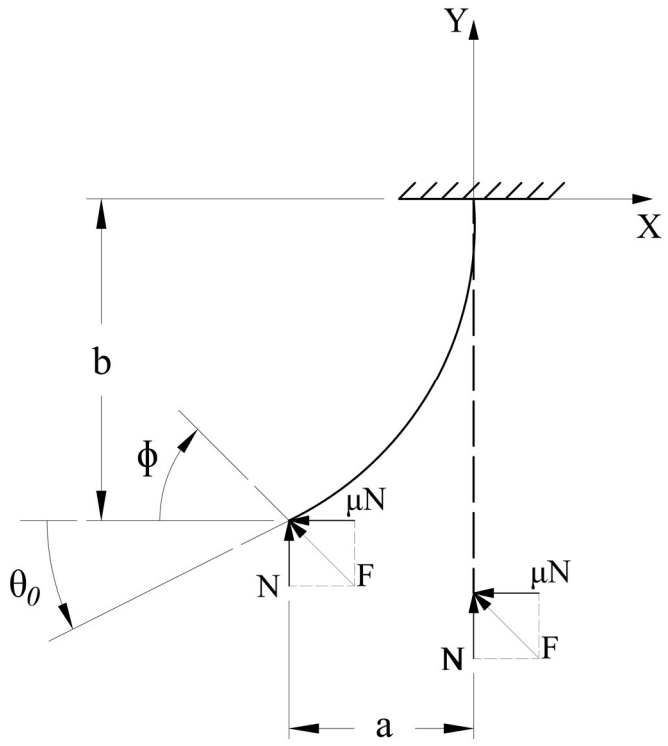

Figure 5.3 Initially Straight Fixed-Free Beam with Force at One End

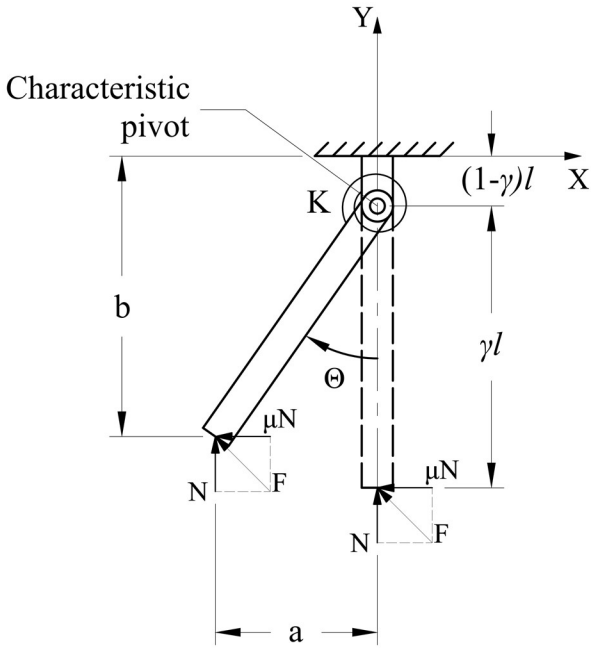

Figure 5.4 PRBM of Initially Straight Fixed-Free Beam with Force at One End

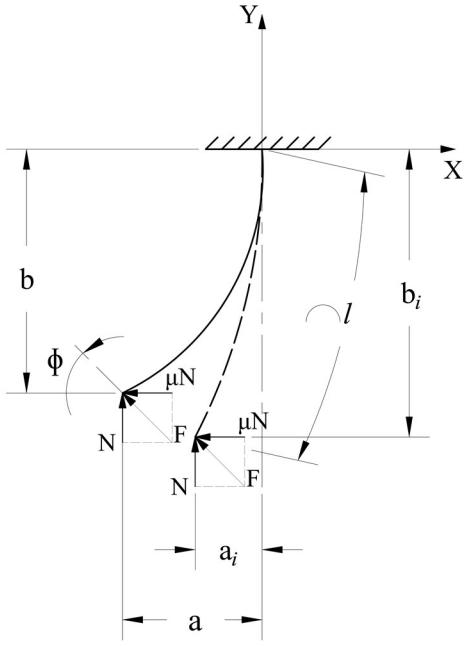

Figure 5.5 Initially Curved Fixed-Free Beam with Force at One End in Vertical Orientation

The beam end co-ordinates of the initially curved beam defined by Howell [70] are derived in detail below. The equations are derived using equations of chord length and arc length of a circular segment by considering the initially curved beam as a segment of the circle. This derivation assumes that the curvature of the beam remains constant after the deflection.

As shown in Figure 5.6, the curved segment with an initial radius of R_i is considered as an arc of a circle with length l. The chord length of the arc is considered as C with a central angle of K_θ. Thus, the X, Y co-ordinates of the beam/arc are obtained by calculating the a_i, b_i. From the triangle formed by the trigonometric relation by joining both ends of the chord, below equations are formed.

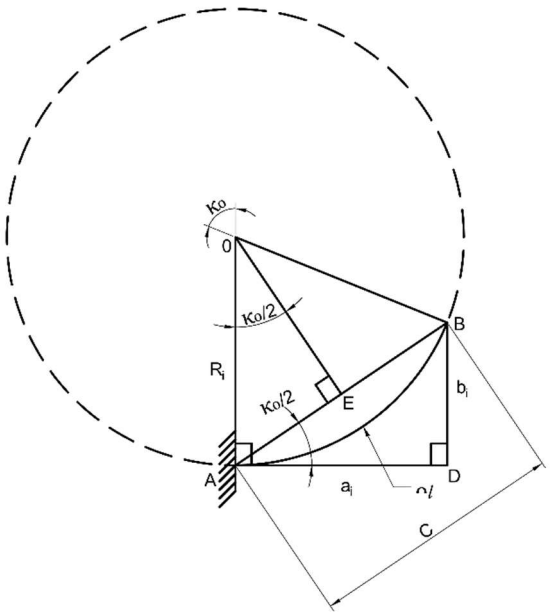

Figure 5.6 Initially Curved Fixed-Free Beam as a Circular Segment

$$\sin\frac{K_\Theta}{2} = \frac{\frac{c}{2}}{R_i}$$

$$c = 2R_i \sin\frac{K_\Theta}{2} \tag{31}$$

where, $K_\Theta/2$ is half of the central angle. From the trigonometric relations

$\angle AOE = \angle DAB = K_\Theta/2$

where,

$$K_\Theta = l/R_i \tag{32}$$

From ΔDAB

$$\cos\frac{K_\Theta}{2} = \frac{a_i}{c}$$

$$a_i = c\cos\frac{K_\Theta}{2} \tag{33}$$

$$\sin\frac{K_\Theta}{2} = \frac{b_i}{c}$$

$$b_i = c\sin\frac{K_\Theta}{2} \tag{34}$$

From Equation 31,

$$a_i = 2R_i \sin\frac{K_\Theta}{2}\cos\frac{K_\Theta}{2}$$

$$b_i = 2R_i \sin\frac{K_\Theta}{2}\sin\frac{K_\Theta}{2}$$

From trigonometric relations, the equation for a_i, b_i:

$$\sin 2\Theta = 2\sin\Theta\cos\Theta$$

$$\cos 2\Theta = 1 - 2\sin^2 \Theta$$

$$a_i = R_i \sin k_\Theta$$

$$b_i = R_i \left(1 - \cos k_\Theta\right)$$

Below is the step-by-step procedure to calculate the deflected beam profile using the radius of curvature approach. The process is majorly divided into two categories, and it is explained in detail in Section 5.2.

i) Calculating the beam end co-ordinates

ii) Calculating the radius of curvature value

5.2. CALCULATING THE DEFLECTED BEAM PROFILE USING RADIUS OF CURVATURE

i) Calculating the beam end co-ordinates: As discussed in Section 3.2, the axial and radial beam end co-ordinates of the fixed-free beam are calculated by using the below equations

$$\frac{a}{l} = 1 - \gamma(1 - cos\Theta) \tag{35}$$

$$\frac{b}{l} = \gamma sin\Theta \tag{36}$$

However, the above end co-ordinates are calculated considering the beam origin at a fixed end. But, in the current arrangement, the origin is considered to be at the characteristic pivot, which needs to be moved to the fixed end of the end. Below are the steps to calculate the beam end co-ordinates: Calculate the beam end co-ordinates using Equations 35, 36 in its initial orientation, as shown in Figure 5.7.

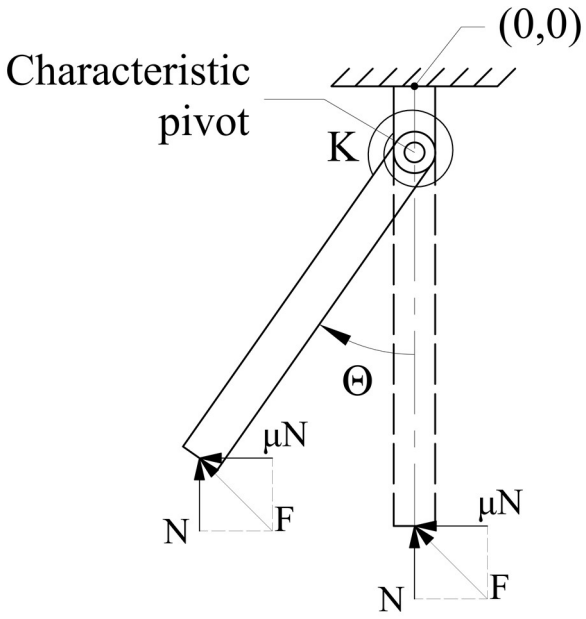

Figure 5.7 Origin of the Co-ordinate System at the Initial Position

Translate the origin to the characteristic pivot. The co-ordinates obtained from step 1 are moved by the value of (1-γ) *l,* which is the distance between the beam fixed end to characteristic pivot, as shown in Figure 5.8. The co-ordinate transformation is an essential step in calculating the deflected beam profile. Suppose the beam end co-ordinates don't fit with the actual beam position with each input displacement. In that case, the resultant beam profile will not depict the actual beam profile, thus misleading the synthesis output results further. To avoid that, also to make sure the setup of the beam orientation is maintained similar to synthesis set up of generating the required force-deflection profile, a few co-ordinate translation operations need to be performed.

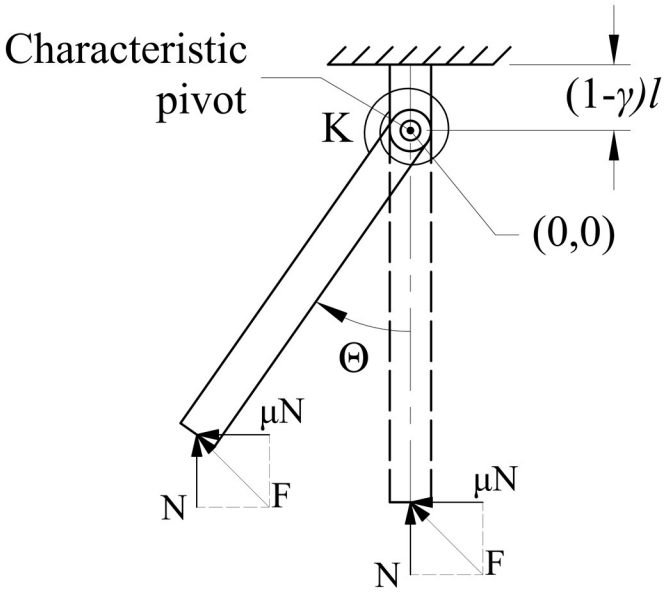

Figure 5.8 Origin Translated to Characteristic Pivot

Translate the co-ordinate system from fixed end to new origin location, i.e. characteristic pivot as shown in Figure 5.9.

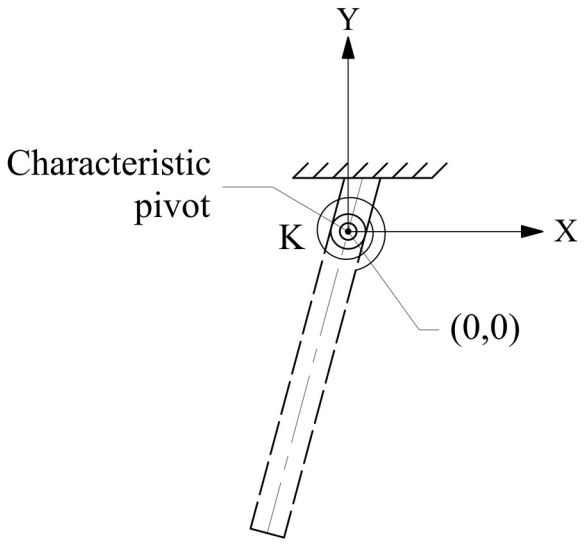

Figure 5.9 Co-ordinate System Translated to Characteristic Pivot

The obtained co-ordinates from are then rotated by 5º, as shown in Figure 5.10 to accommodate the beam initial angle.

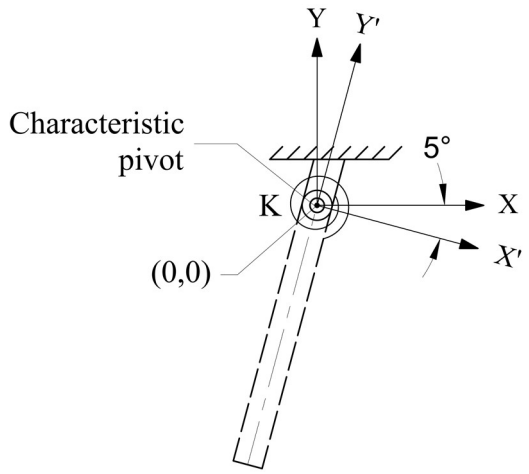

Figure 5.10 Co-ordinate System Rotated to 5°

The obtained co-ordinates from above are translated to a fixed end as a new origin, as shown in Figure 5.11.

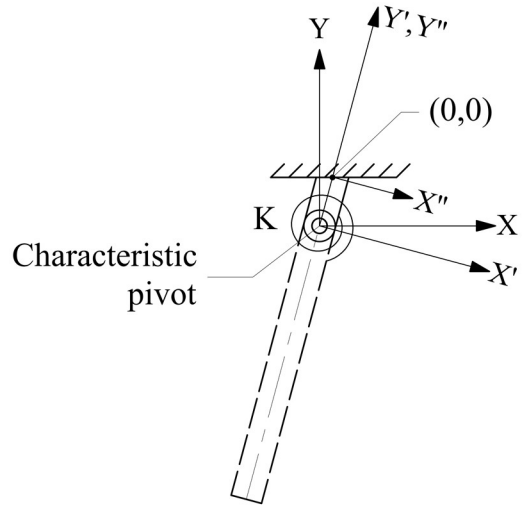

Figure 5.11 Co-ordinate System Translated to Fixed End

The mechanism is displaced vertically for the given input displacement value; the co-ordinates obtained from above are transferred to this local origin. The fixed end of the beam is transferred to the input displacement value, which is a function of total travel value, and the number of elements the cam surface is divided into. Each beam end co-ordinate is calculated for the respective local origin, as shown in Figure 5.12.

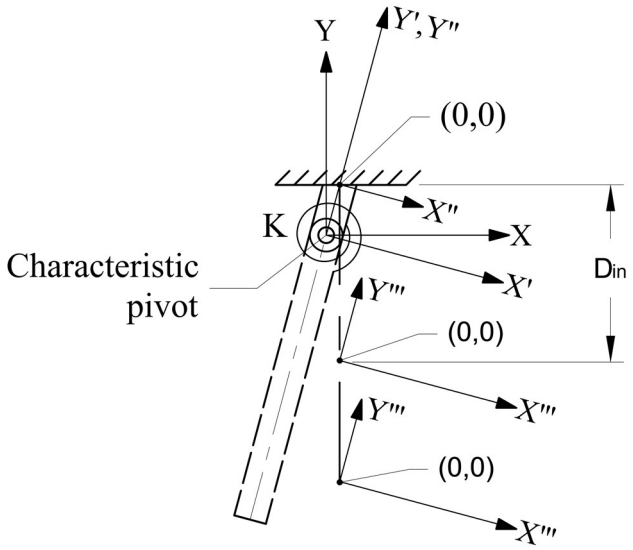

Figure 5.12 Co-ordinate System Translated to Input Displacement

The obtained co-ordinate values from above are translated as a new origin, as shown in Figure 5.12. But the X co-ordinate from Figure 5.12 is considered Y co-ordinate of the beam end (b_i). The obtained Y co-ordinate is considered X co-ordinate of beam end (a_i) because of the current mechanism's vertical beam orientation. The obtained beam end co-ordinates of the deflected beam are compared with FEA beam end co-ordinates, as shown in Figure 5.13. The maximum percentage error calculated between these co-ordinates is below 0.5%. The co-ordinate values obtained are supplied

as initial co-ordinates in the Equation 29 &30 to solve k_0 and find the radius of curvature value from Equation 28. By using the radius of curvature value, the deflected beam profile is drawn for every element of the cam surface. The resultant beam profiles are compared with FEA results.

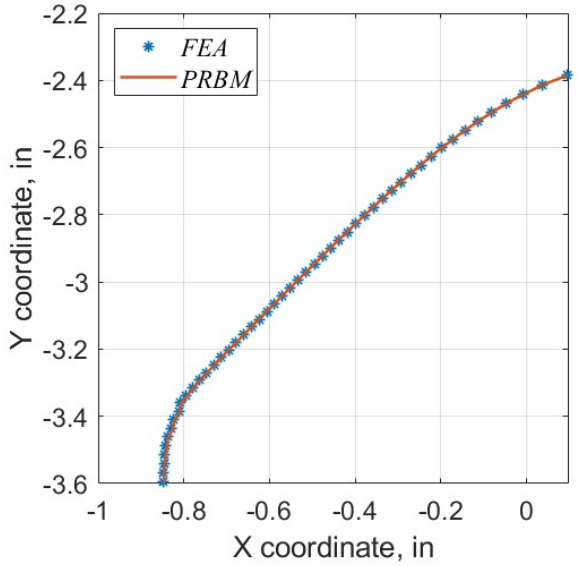

Figure 5.13 Comparison of Beam End Co-ordinates from PRBM & FEA

5.3. FEA APPROACH

As mentioned before, the deflected beam profile can be obtained using the FEA approach. In the FEA approach, the beam is divided into an 'n' number of elements. By using the Euler-Bernoulli beam elements and applying the boundary conditions, the deflected beam end co-ordinates are solved. The below finite element model is used to solve the unknown displacements.

$$[K]\ \{U\} = \{F\} \tag{37}$$

$$\{U\} = \{F\}\,[K]^{-1} \tag{38}$$

$$w_1 = 0 \tag{39}$$

$$\frac{dw_1}{dx_1} = 0 \tag{40}$$

$$w_{801} = x\ co-ordinate\ of\ cam\ surface \tag{41}$$

$$[U_1, U_2, U_3, U_{4,} \ldots..] = [w_{1,}\theta_1, w_2, \theta_2 \ldots.] \tag{42}$$

$$[F_1, F_2, F_3, F_{4,} \ldots..] = [P_{1,}M_1, P_2, M_2 \ldots.] \tag{43}$$

For each element, the stiffness matrix [K] is calculated and assembled to find the global stiffness matrix. The boundary conditions of the cantilever beam are provided as an input to set up the nodal displacement vector {U} and force vector {F}. At the fixed end, the displacement and rotation of the elements are zero. Also, the displacement at the final element is from the cam surface co-ordinates. The displacement matrix corresponds to element transverse displacement and rotation, and the nodal force-displacement matrix is defined as the element load and moment. This approach is developed based on Peter I. Kattan's MATLAB Guide to Finite Elements [83]. The process also considers the initial beam angle to find the beam's transverse and axial deflection as shown in Figure 5.14. Euler- Bernoulli beam elements are typically accommodating the small deflections of beam. However, in the mechanism the deflections are considered to be large deflection. By using Chain-Algorithm [84] the large deflections can be accurately modeled as many Euler- Bernoulli elements.

According to [85], “each element is considered inextensible and therefor the axial deflection is assumed to be negligible. Consequently, a large number of elements are required for accurate results”. However, the initial angle of the beam contributes to the axial deflection of the beam. Where, the x-co-ordinate of the undeflected beam is the x-co-ordinate of the deflected beam. From the Figure 5.14 the axial deflection of the element is considered as $[L_i cos\Theta_i]$ and the transverse deflection as $[w_i]$. The deflected beam shape can be approximated by adding these deflections of each element from fixed end.

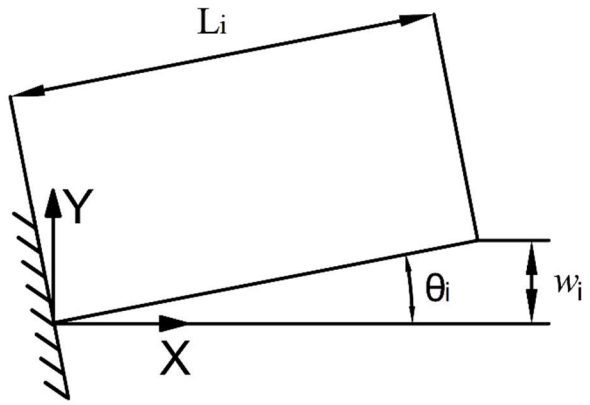

Figure 5.14 Beam End Co-ordinates of Element *i* in FEA

Figure 5.15 depicts an example of beam element discretization in chain algorithm approach where the beam is divided in to two elements and the transverse deflection and beam end angle is measured for each element.

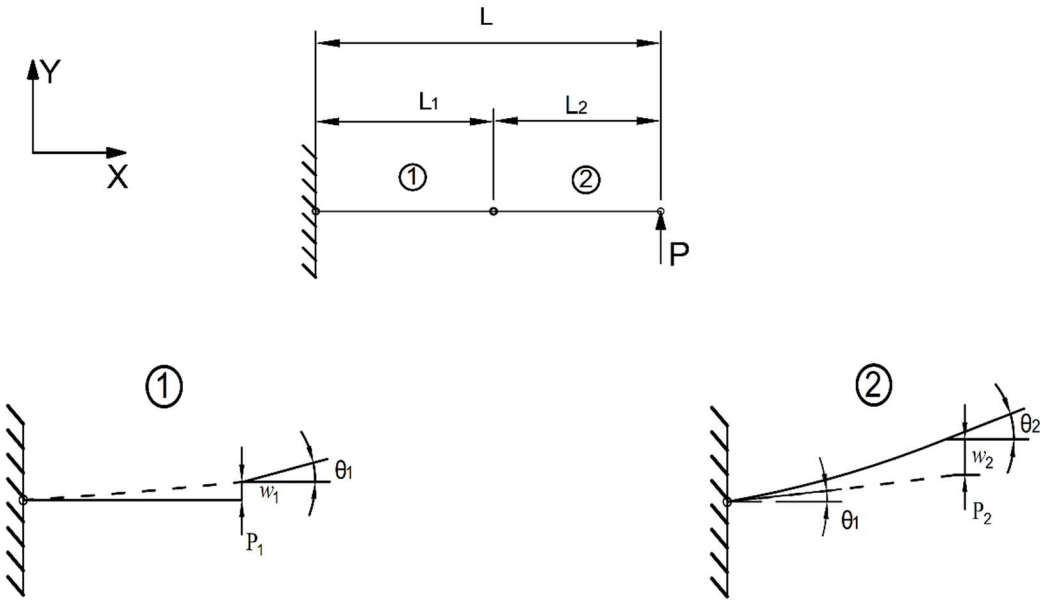

Figure 5.15 Beam Element Discretization in Chain Algorithm

5.4. COMPARISON OF RESULTS BETWEEN FEA AND PRBM

The deflected beam profiles obtained from FEA and PRBM are compared in Figure 5.16 and Figure 5.17 for 3 positions. The deflected beam obtained from PRBM is considered as accurate as the results from FEA. Because to balance the runtime accuracy, the number of beam elements is limited to 800. The discrepancy in the results is due to the consideration in the PRBM approach that the deflected beam shape always follows an arc. Where in FEA, moments of each element are calculated to generate the resultant deflected beam profile. The deflected beam profile from PRBM is drawn by using the radius of curvature value as an arc radius. The start point of the arc is the fixed end of the beam, and it changes with every input displacement. The endpoint of the arc is the center of the rigid radius at the corresponding position on the cam surface. The deflected beam positions are then verified to check the interference of the beam with the cam surface.

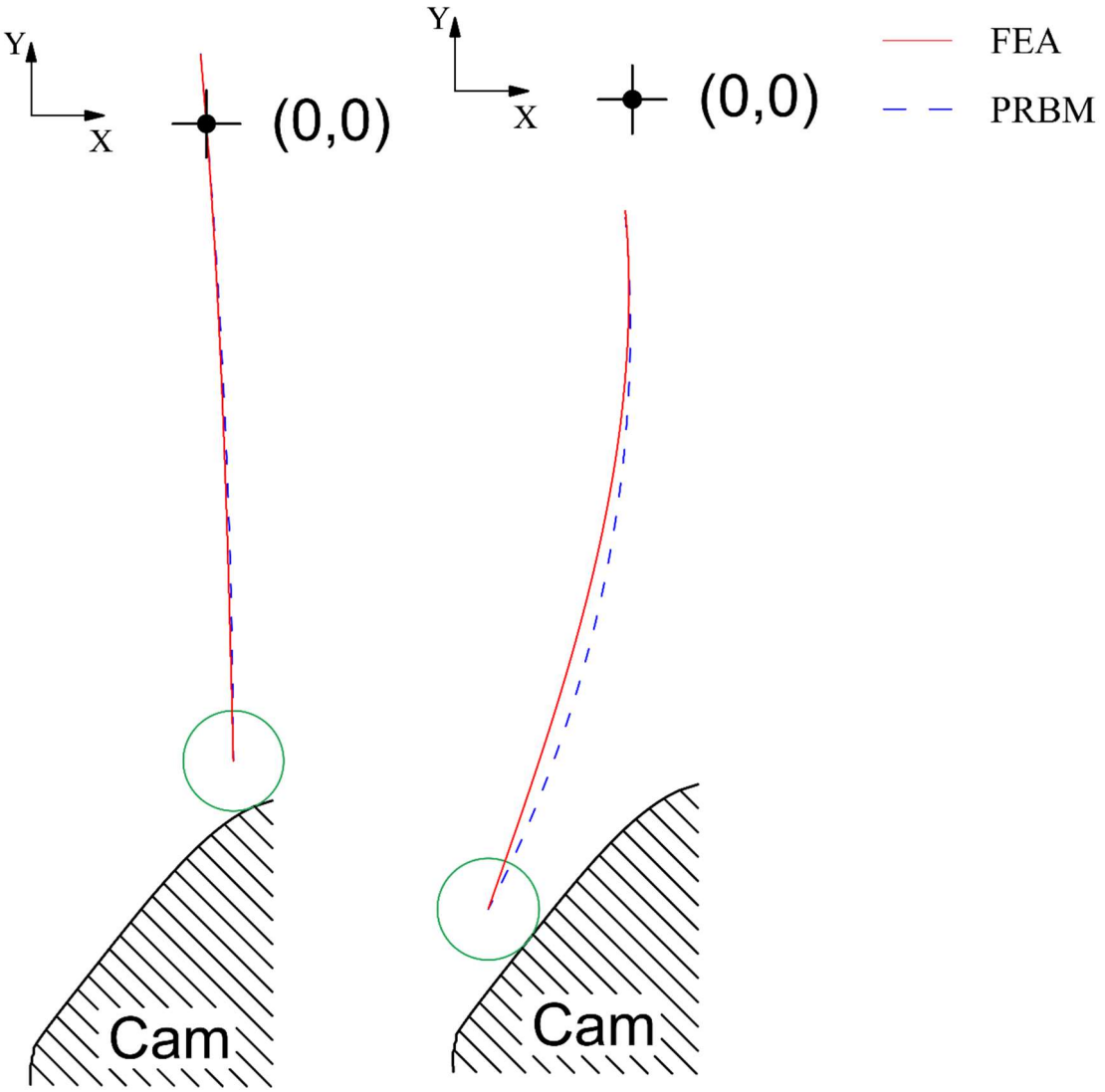

Figure 5.16 Comparison of Deflected Beam Profiles from PRBM & FEA at Different Positions

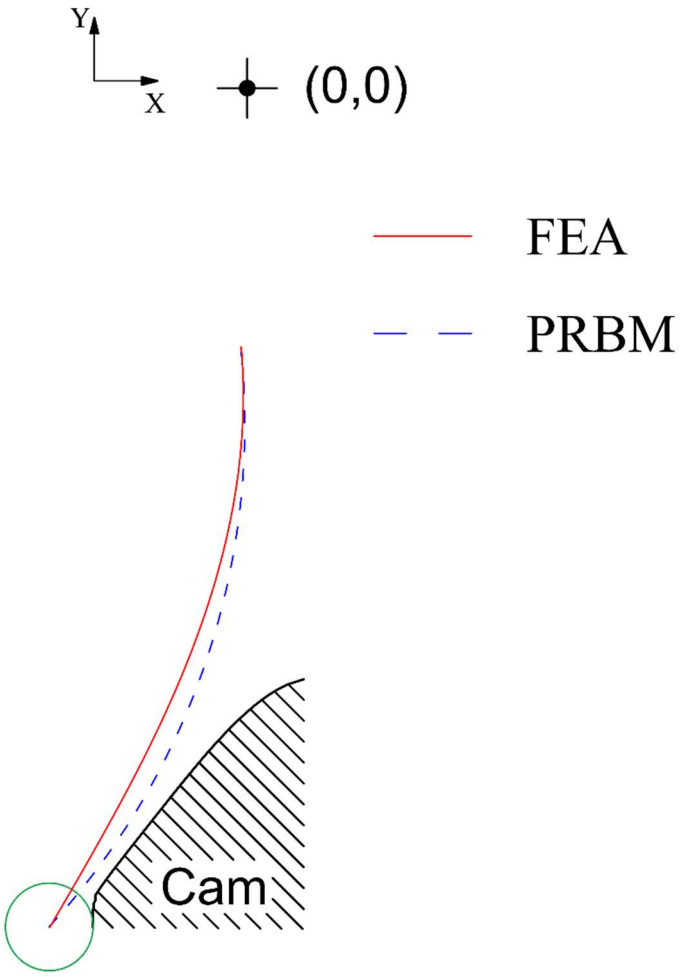

Figure 5.17 Comparison of Deflected Beam Profiles from PRBM & FEA at Different Positions

6. METHODOLOGY TO GENERATE REQUIRED FORCE-DEFLECTION PROFILE

6.1. MATHEMATICAL MODEL OF HAND FORCE

As mentioned in Section 2.3, the current research approach utilizes the mathematical model and force profile trend of the human hand developed by Freund et al. There are several reasons to choose this curve for hand exerciser design. The curve is developed by conducting several experiments on the human hand. The effect of different lengths of non-thumb fingers is also considered in developing this curve. Also, [72,74] experiments proved that gripping strength reduces with increasing the handle diameter. Freund et al. curve trend also validates this conclusion. It is evident that optimum gripping force doesn't change with alteration in finger length and cylinder diameter, and it remains at $k_{opt,}$ optimum relative diameter. This is defined as the ratio of the optimum cylinder diameter to finger length. The individual fingers' contribution to the total gripping force remains the same. This finding supports the assertion that optimal gripping force occurs at an optimal relative diameter. However, the mathematical model doesn't change the value of the maximum force of the hand. But it considers the different positions of the hand to avoid the muscles overstraining. Even though the curve is regarded as the user's maximum grip force, this value can be varied due to a change in measurement method and equipment. Also, the hand biomechanisms are impacted by the position of the wrist and elbow during the grip force measurement. Equation 44 describes the mathematical model developed by Freund et al. of hand in terms of relative cylinder diameter by utilizing the various experimental outcomes. These outcomes were further verified for the force distribution of grip force.

$$\frac{\bar{f}}{\bar{f}_{opt}} = \left({}^{k}/_{k_{opt}}\right)\frac{\left({}^{k}/_{k_{opt}}\right)\delta + 2(1-\delta)}{\left({}^{k}/_{k_{opt}}\right)^{2} + 1 - \delta} \tag{44}$$

where, $$k = {}^{d}/_{l} \tag{45}$$

The constraints for the above equations are follows:

$$\bar{f} = 0 \tag{46}$$

when, $k = 0$

$$\bar{f} = \bar{f}_{opt} \tag{47}$$

when, $k = k_{opt}$

$$\bar{f} = \bar{f}_{lim} \tag{48}$$

when, k→∞

The constraint1 is based on, the gripping force decrease as the cylinder diameter increase which is also supported by [72]. The constraint 2 indicated that the optimum gripping occurs at optimum cylinder diameter, the function global maximum is at $k_{opt} = \frac{d_{opt}}{l}$. The constraint 3 is explained by we cannot put much force on flat plate. This assumption is also experimented by Zong et al. [86] with a cylinder diameter d→ ∞.

6.2. PRESCRIBED FORCE DEFLECTION PROFILE FOR A GIVEN FORCE

The mathematical function from Equation 2 and the curve trend from Figure 2.6 is modified for adaptable exerciser design. The Freund et al. function in Figure 2.6 starts with a closed hand position. However, in general, the exercising device starts with an open hand position. To accommodate that, the function is flipped, as shown in Figure 6.1. The relative diameter *k* is replaced in terms of D is the deflection of hand exerciser and *Travel* is the distance traveled between hand open and close position.

$$\frac{d}{l} = \frac{-D + Travel}{Travel} = 1 - {}^{D}/_{Travel} \tag{49}$$

$$\frac{P}{P_{max}} = \frac{0.11 * 3.7^2\left(1 - {}^{D}/_{Travel}\right)^2 + 2(1 - 0.11) * 3.7\left(1 - {}^{D}/_{Travel}\right)}{3.7^2\left(1 - {}^{D}/_{Travel}\right)^2 + 1 - 0.11}$$

$$P = P_{max} \frac{1.51\left(1 - {}^{D}/_{Travel}\right)^2 + 6.59\left(1 - {}^{D}/_{Travel}\right)}{13.7\left(1 - {}^{D}/_{Travel}\right)^2 + 0.89} \tag{50}$$

Currently, Travel value is chosen based on the ranges offered by hand exercisers. This value can be modified based on user needs and for the current testing's and models a value of 1.4" is chosen. From Equation 2 the terms *f, f_{opt}* are replaced by *P, $P_{max.}$* This modified Equation 50 in terms of D, *Travel*, *P,* and $P_{max.}$ is used as an input to the synthesis method [69]. The P_{max} value can be selected based on maximum user resistance

to avoid the inconveniences while performing the exercises, while P is the output resistance experienced by the user based on the chosen Travel and P_{max} values. The modified force-deflection profile is shown in Figure 6.1.

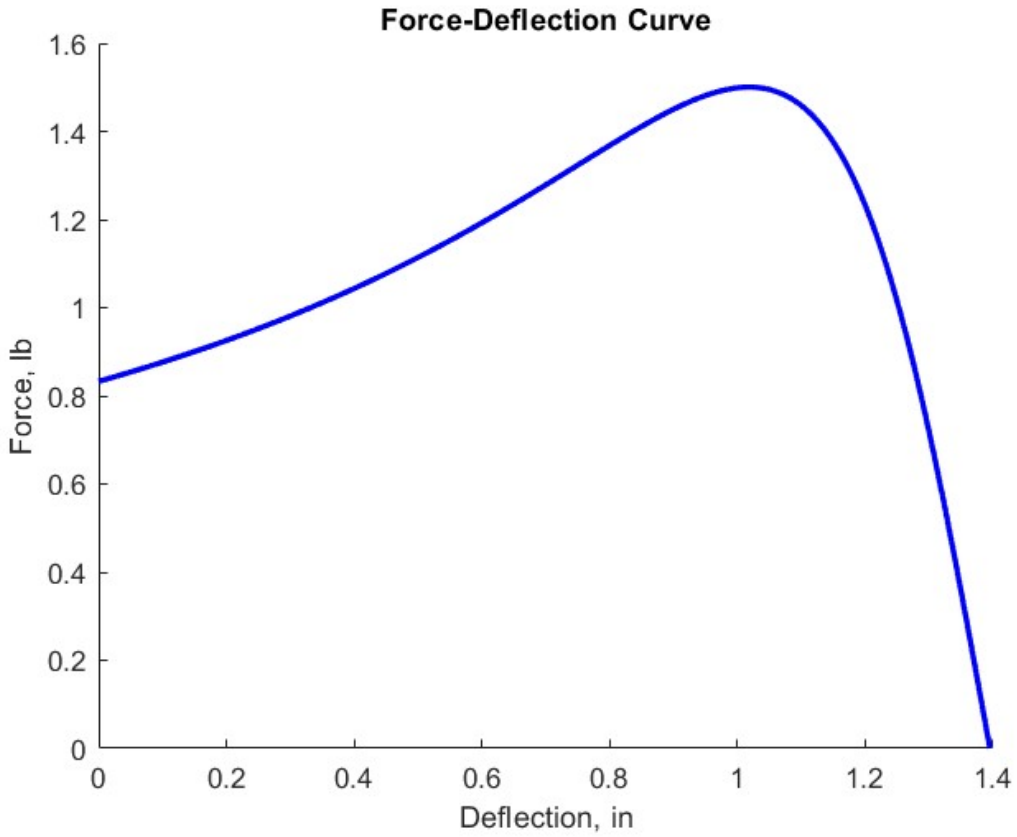

Figure 6.1 Modified Freund et al. Function

The input variable values chosen for the synthesis are shown in Table 6.1. An initial beam angle of 5º is given to allow the beam deflection. This is the angle the beams are designed to mount inward while making contact on the cam surface at the first node. The system is ready for the actuation at the position, but there is no transverse load acting at this position.

Table 6.1 Input Variable Values

Variable	Value
E	$30.5x10^6$ psi
I	2.1375e-06 in4
Θ_1	-5°
μ	0.1
γ	0.89
K_Θ	2.65
l	2.65 in
w	0.95 in
t	0.03 in

The steps of the methodology are shown in the flow chart presented below. A case study is then presented, following all the steps. For the case study, a force value of 15lb is considered. In the proposed approach, the 15lb is achieved by using two identical compliant beams and a cam profile in the mechanism, each beam providing 7.5lb. The value of $P_{max.}$ is 7.5lb substituted in the Equation 50 as required input to synthesis method along with beam geometrical and material properties. The input variable values presented in table 6.1 are also used as input to synthesize the required cam profile using the synthesis approach [82].

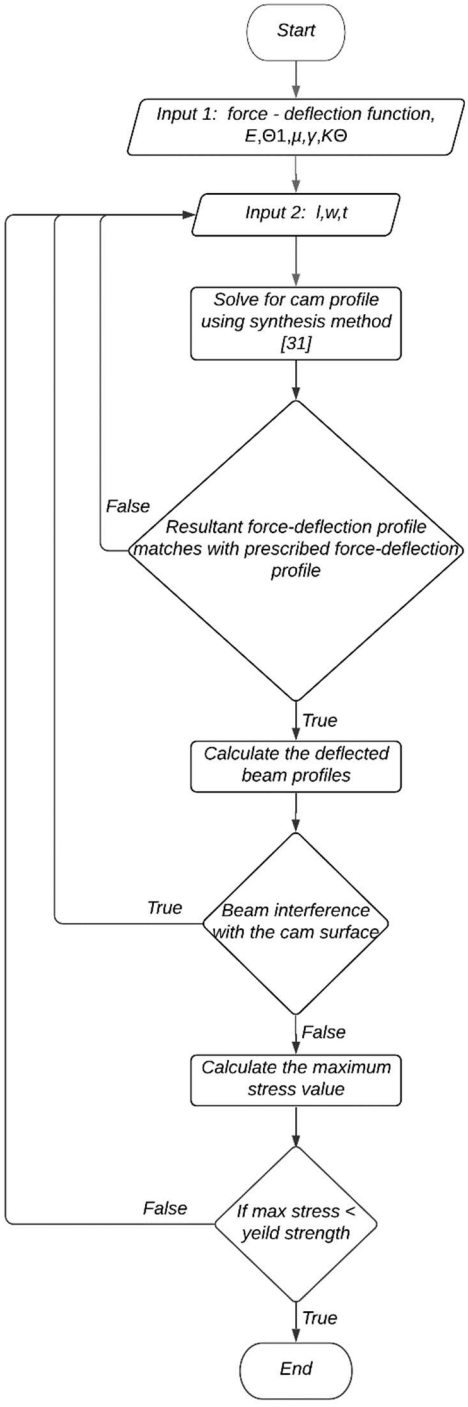

Figure 6.2 Flowchart of Methodology

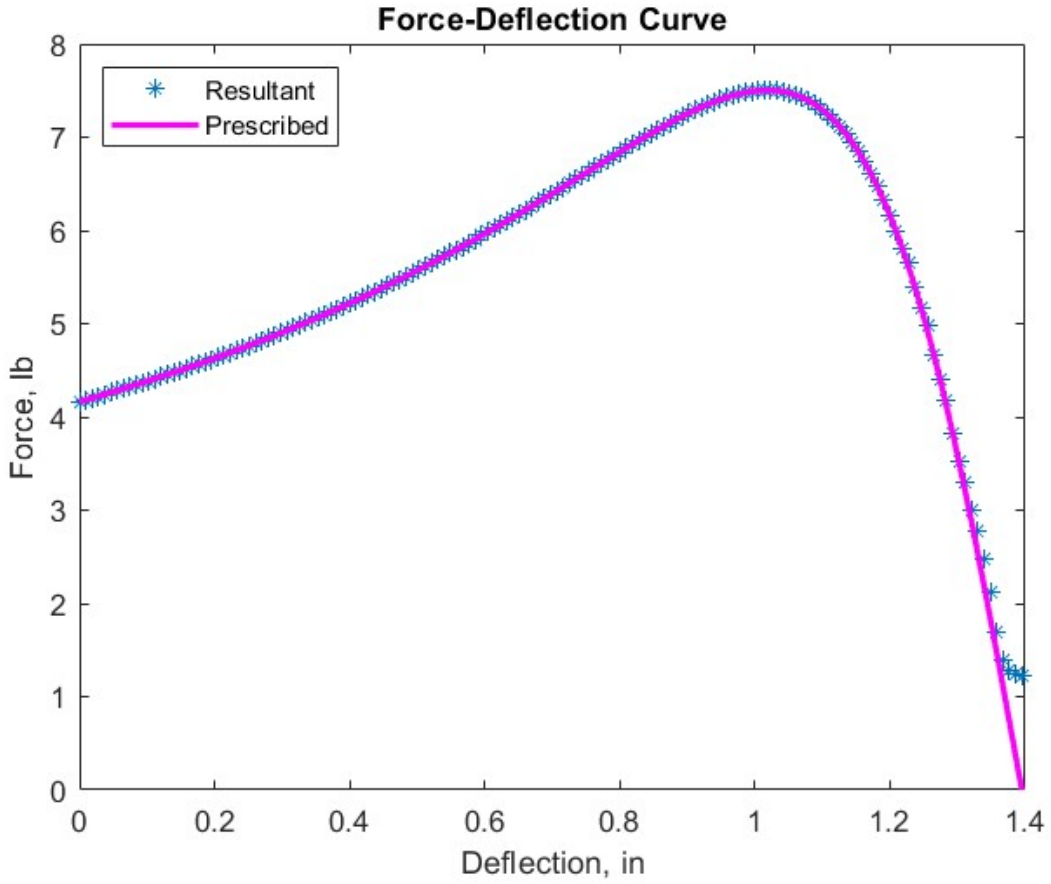

Figure 6.3 Force-deflection Profiles of Synthesis Result and Prescribed

The PRBM parameters γ, K_θ for the approach is used from [14,31]. The resultant force-deflection profile from this mechanism is compared with the prescribed function in Figure 6.3. The deflected beam profiles are then checked for interference with the cam surface for the entire travel. If the maximum stress in the beam is less than the material's yield strength, then the beam and cam parameters can be utilized. If the resultant force-deflection profiles don't match with the prescribed input force-deflection profile, values of the beam geometrical properties in the input should be modified. The same approach needs to be followed if there is any interference of beam with cam surface or the

maximum stress value is less than the yield strength of the material chosen. The deflected beam profiles are calculated using both FEA and the novel PRBM approach presented in this thesis, and results are compared.

The current hand exerciser is developed for a force ranges between 3lb to 15lb. this range is chosen based on the available hand exerciser force ranges. The hand ergonomics were taken into considerations along hand tool design guidelines. The constraints for the input parameters are chosen such that the thickness values are spring steel or stainless-steel industrial standard thickness values. The length and width of the steel beams are chosen such that the overall dimensions of the mechanism are followed by hand tool design guidelines [87-90] and comfortable to operate with average human hand size [91]. For the chosen spring steel beam with E value ranging between 270 ksi to 305 ksi and yield strength of 310ksi the various resistance ranges are developed.

The input beam parameters to achieve the force-deflection values that can be accommodated in a human hand are chosen based on the below considerations. One of the important considerations is to maintain compliance with the hand tool design guidelines [87]. Also, according to [88], the overall product dimensions should be not more than span range of 5.5inch. To achieve the mentioned dimensions by considering the limitations on the material properties, the geometrical dimensions (L x W x H) of the beams in this research are designed by not exceeding the yield limit when subjected to the maximum stress to avoid failure.

The maximum limit of the length is chosen based on the overall height limitation of the hand tool. Given the cam height is approximately 1.5 inch, the maximum length of

the beam can be 2inch. This would result in at least 1.5inch – 2inch of allowance for clamping.

According to [91], the maximum width can be up to 2.5 inch. But based on user experience and study of state-of-the-art hand exercisers, anything more than 2-inch width is uncomfortable for day-to-day use. The beamwidth is limited to 1inch, providing a maximum allowance for the product enclosure.

The thickness of the beam doesn't have to follow any limitations because of the mechanism orientation. But the thickness value is chosen to enable ease of material procurement. However, thinner beams can deflect more than thicker beams, but the stresses generated will be higher. The thickness of the beam is chosen such that the maximum stress of the beam is less than the yield strength value.

Table 6.2 Resistance and Stress values for Various Ranges

Beam Length (in)	**Beam Thickness (in)**	**Resistance (lb)**	**Stress (Ksi)**	**% Of Yield Strength**
1.7	0.015	3	196	63
1.75	0.02	5	212	68
1.75	0.025	7	219	70
1.75	0.03	10	227	73
1.75	0.032	13	241	77
1.75	0.032	15	264	85

7. EXPERIMENTAL TESTING AND VALIDATION OF THE MECHANISM

7.1. INTRODUCTION TO TESTING

Experimental testing plays a significant role in determining the effectiveness of analytical results. The proposed synthesis methodology is simple in approach with a given understanding of essential MATLAB and concepts of compliant mechanisms. The designer can easily modify the mechanism to the required force value depending upon user requirement by adjusting the beam parameters length, width, and thickness.

The proposed mechanism is validated in the previous sections using both FEA and a PRBM approach. This section explains the experimental testing conducted to prove the accuracy of the synthesis methodology results.

7.2. TEST SETUP DESIGN

A test setup is designed to perform the experimental testing. The CAD illustration of the test setup is shown in Figure 7.1. Figure 7.1 is depicted as the manufactured test setup. The test setup is similar to the one used in [82]. This setup contains two flexible spring steel beams and two machined rigid cams. The end of the flexible beam is attached to the Delrin cylinder. Instron Universal Testing Machine [92] is used to perform the test. The setup's overall dimensions are 4 inches in diameter and 6.5 inches in height. The sprig steel beams are waterjet machined to the required dimensions from a spring-steel sheet of 5feet long from the rock mechanics facility at Missouri S&T. One end of the flexible beam is screwed to the top mounting plate to create a cantilevered effect. The

other end of the beam is attached to the Delrin cylinder to ensure smooth travel on the cam surface.

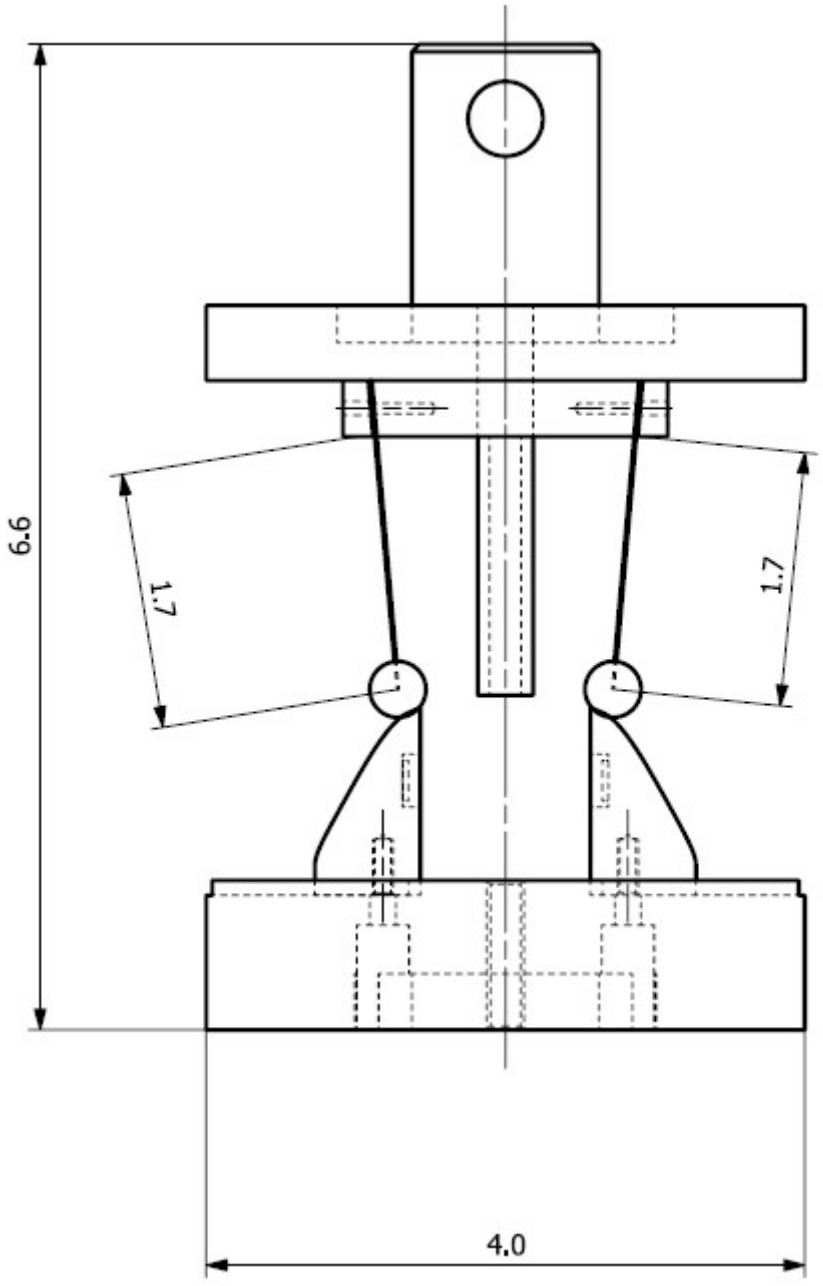

Figure 7.1 Test Setup for Hand Exerciser

A Delrin rod of 1 feet length is cut into pieces of the required length, and a center slot is machined to attach it to the beam, as shown in Figure 7.2.

The top and bottom plate of the test setup is designed to be mounted in the UTM machine [93]. The fixture profile on the UTM machine was studied, and a provision for clamping pin is added on the top plate. This provides the user a better control while testing and also the weight can be set zero before the testing. Three clamping pieces are machined such that the beams are clamped at an angle of 5°. The two outer clamping pieces have relief holes for the threaded holes, and the center mounting piece has thread holes on both sides. The center mounting piece is press-fit to the top plate by a shaft.

The rigid cams are machined on a CNC machine [94] at Missouri S&T to the required profile using an end milling [95] operation. To ensure the smoothness of the curve, the profile is milled as shown below Figure 7.3. The material on the cams is removed in the same direction of the beam travel.

After the profile is milled, the pieces are cut into required sizes to create the flat surfaces. The threading operation is performed at the end. A flat surface is added at the cam bottom such that the beams can complete the full travel on the cam without contacting the ground. Also, the cam face is extended at the initial point to provide the necessary preload to beams. The cams are screwed to the base accurately so that the beam end is tangent to the cam surface.

The accurate mounting positions of the beam and the cam on the top piece and bottom piece of the test setup are derived from the synthesis approach. For each force-deflection profile, the location of the cam with respect to the beam orientation must be referred duly.

Figure 7.2 Water Jet Machined Spring Steel Beams

Initially, the cams were machined, as shown in Figure 7.4, where the milling operation is performed in a way such that the resultant cam surface was not smooth for the beam travel. The surface finish of the cam plays a vital role in the resultant force-deflection profile. If the smoothness of the cam is not maintained as the synthesized cam; smooth spline curve, it would affect the total output force generating from cam – follower mechanism. This resulted in the machining of new cams, as shown in Figure 7.5, to avoid the burrs and achieve a greater surface finish. In which the material is removed in the same direction as the flexible beam travel during the mechanism operation.

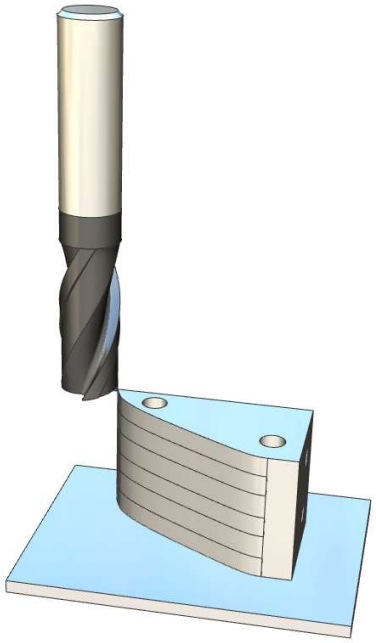

Figure 7.3 Desired Cam Profile Machining

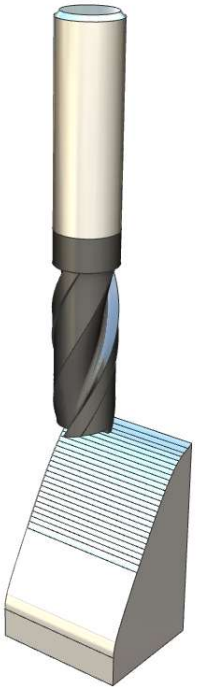

Figure 7.4 Initial Orientation of Cam Profile Machining

The base of the test setup is designed considering UTM bottom fixture dimensions. A rectangular slot is machined such that the cam is securely screwed to the base. The face of the base has relief holes for the screw holes, and the bottom face has threaded holes. The secondary holes are drilled on the bottom face to provide relief for the screw head. Again, these hole locations are accurately measured through CAD design to ensure the beam tangency to the cam surface. The engineering drawings of all the components are found below. A detailed bill of the material list is also added.

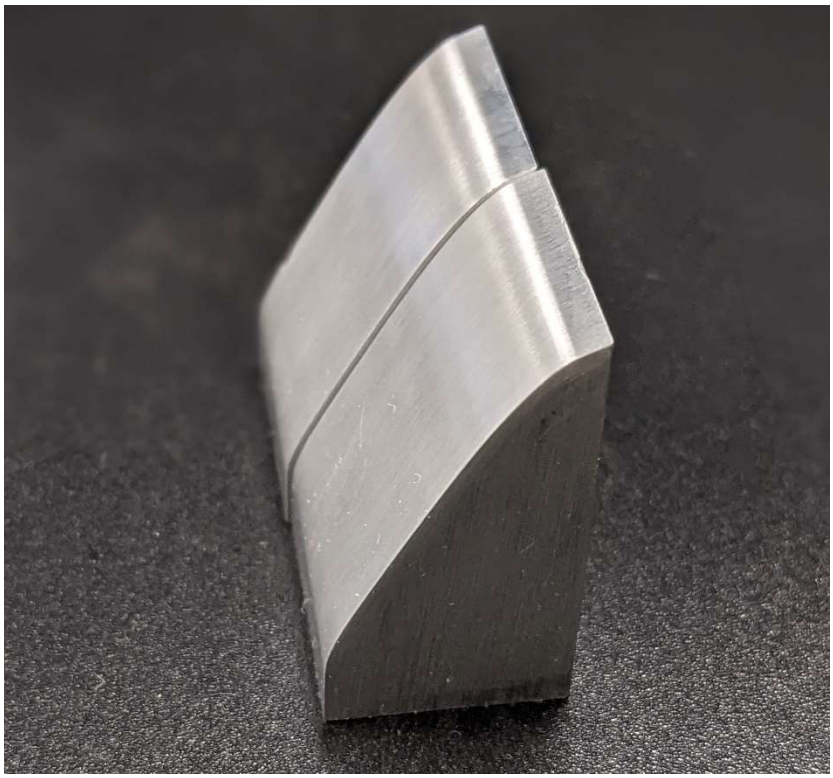

Figure 7.5 Machined Cam Surfaces

7.3. CASE STUDY 1 – HUMAN HAND FORCE-DEFLECTION PROFILE WITH 3LB RESISTANCE FORCE

The modified force-deflection from Equation 50 with a P_{max} value of 3 is used as an input to the synthesis method [82] to generate the cam surface. The flexible beams and cam surfaces are fabricated using the resultant dimensions obtained from the synthesis approach. The variable values presented in table 7.1 are used to generate the force-deflection shown in Figure 7.6 with the maximum resistance force of 1.5lb. Since two beams are used the total maximum resistance force is 3lb with each set of beam and cam are designed to generate 1.5lb during the operation. The obtained results from the experimental testing and synthesis approach are compared in Figure 7.7& 7.9.

Table 7.1 Input Variable Values

Variable	Value
E	30.5×10^6 psi
I	1.9687e-07 in4
Θ_1	-5º
μ	0.1
γ	0.89
K_Θ	2.65
l	1.7 in
w	0.7 in
t	0.015 in

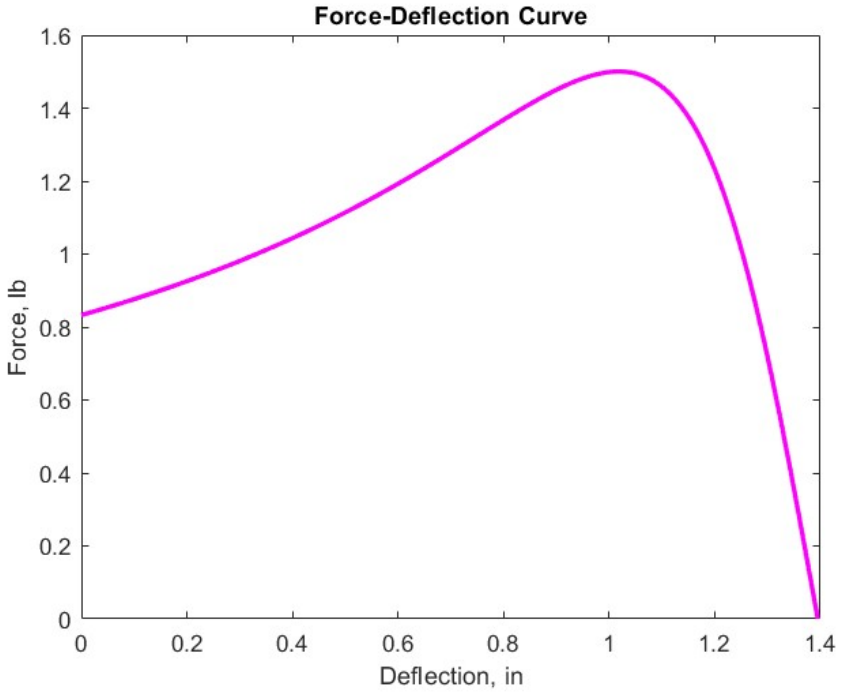

Figure 7.6 Prescribed Force- Deflection Profile of Each Beam and Cam

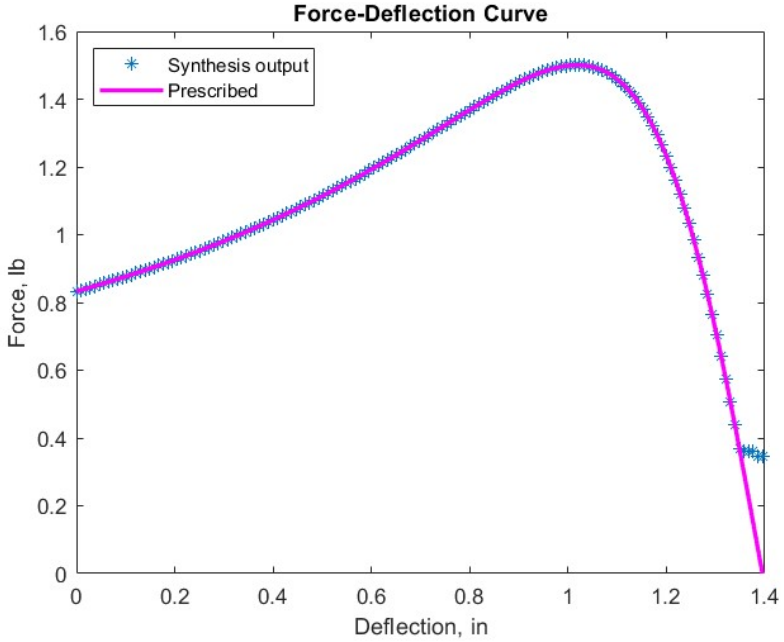

Figure 7.7 Comparison of Force-Deflection Profiles

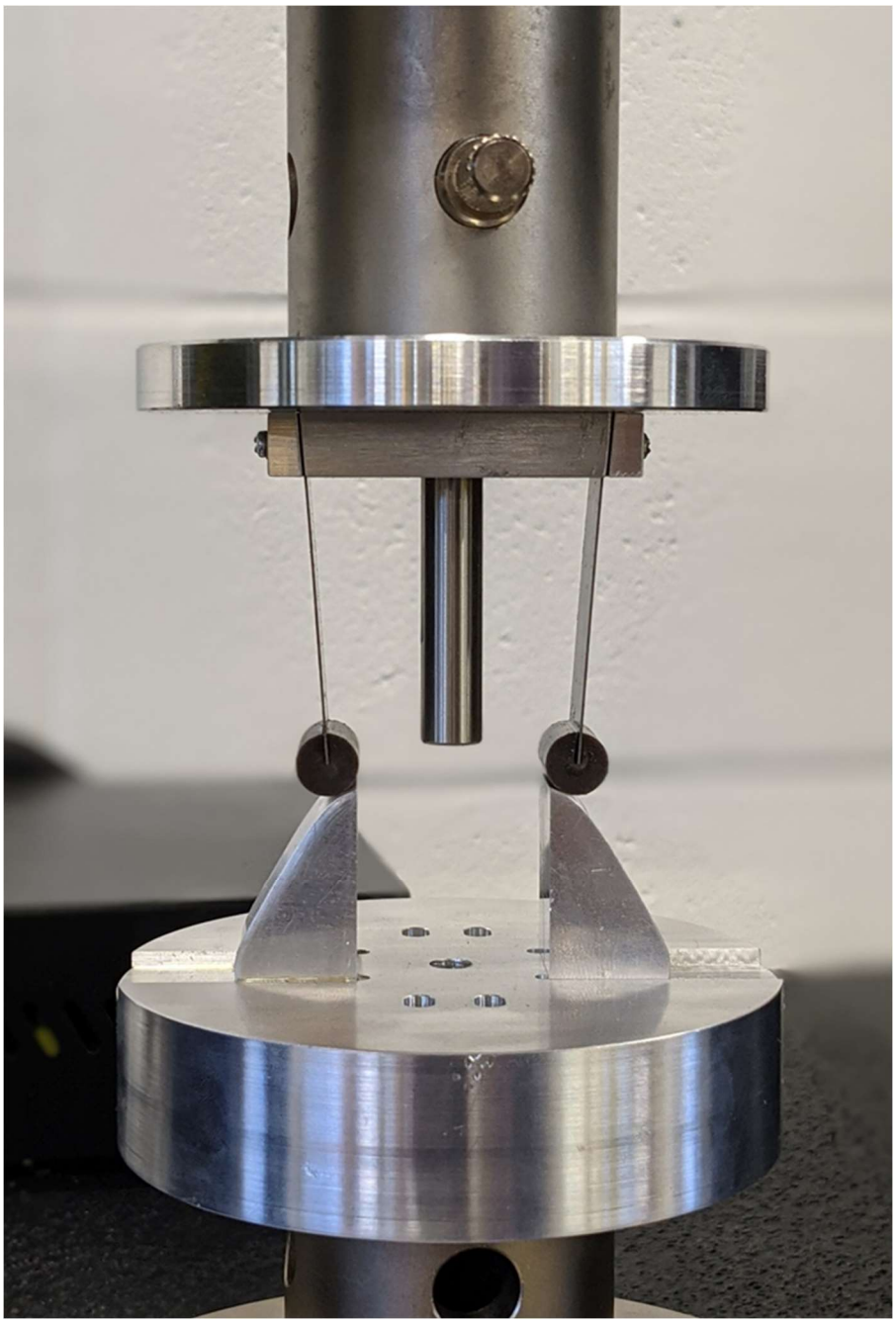

Figure 7.8 Test Setup in UTM

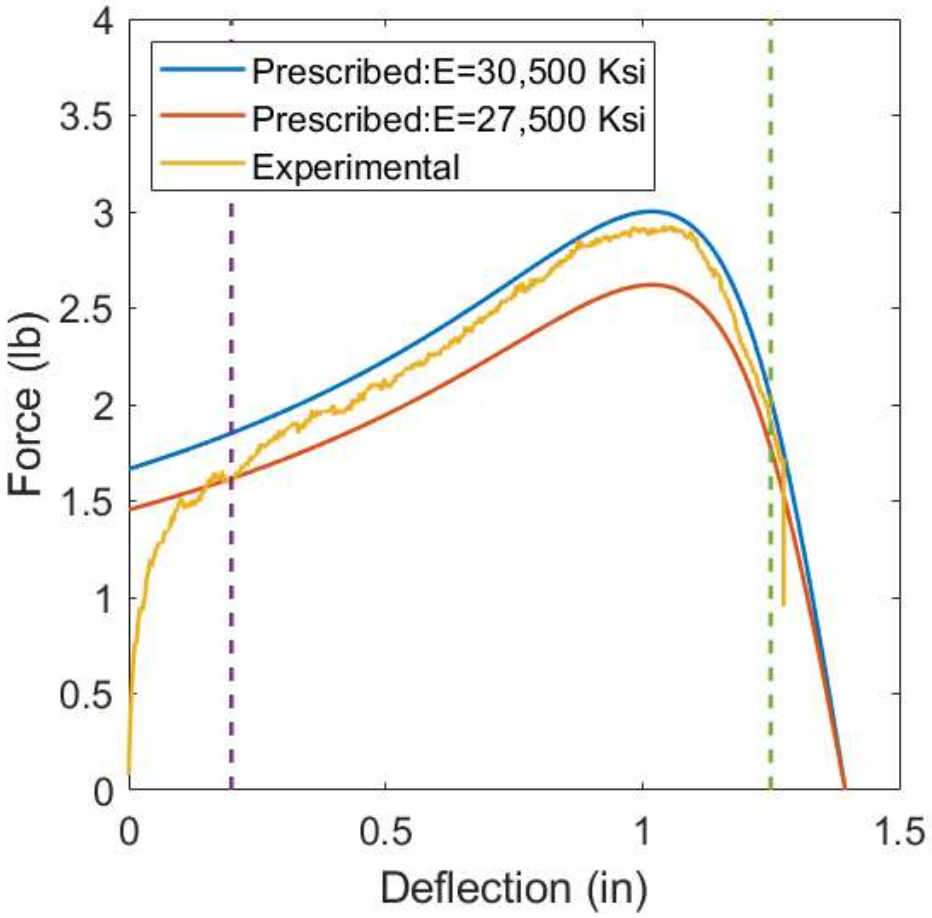

Figure 7.9 Experimental Results of Force- Deflection Profile for 3lb Force

7.4. CASE STUDY 2 – HUMAN HAND FORCE-DEFLECTION PROFILE WITH 15LB RESISTANCE FORCE

The modified force-deflection from Equation 50 is used as an input to the synthesis method [96] to generate the cam surface. The flexible beams and cam surfaces are fabricated using the resultant dimensions obtained from the synthesis approach. The variable values presented in table 7.2 are used to generate the force-deflection shown in Figure 7.10 with the maximum resistance force of 7.5lb. Since two beams are used, each set of beam and cam are designed to generate 7.5lb during the operation the total force

from the setup is 15lb. The obtained results from the experimental testing and synthesis approach are compared in Figure 7.11.

Material properties of the spring steel are a vital input parameter for the synthesis approach. In both the experimental results, it is observed that the testing results are presented with the range of E values. This is because, in contrast to the theoretical value, the spring steel material E value is expected to range from $30.5x10^6$ psi to $27x10^6$ psi. Initially, the synthesis is performed with an E value consideration of $30.5x10^6$ psi [97]. But according to the [98-100] material datasheet, the E value cannot be maintained constant for the spring steel sheets because of their thickness. However, the experimental results were found to be within the given range, and unlike expected results from synthesis, it couldn't generate the exact 3lb or 15lb force because of the E value inconsistency.

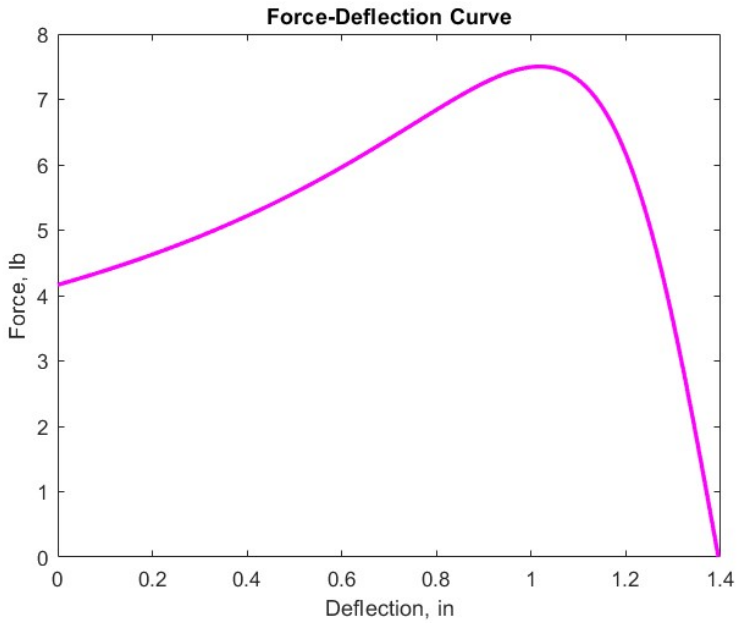

Figure 7.10 Prescribed Force- Deflection Profile of Each Beam and Cam

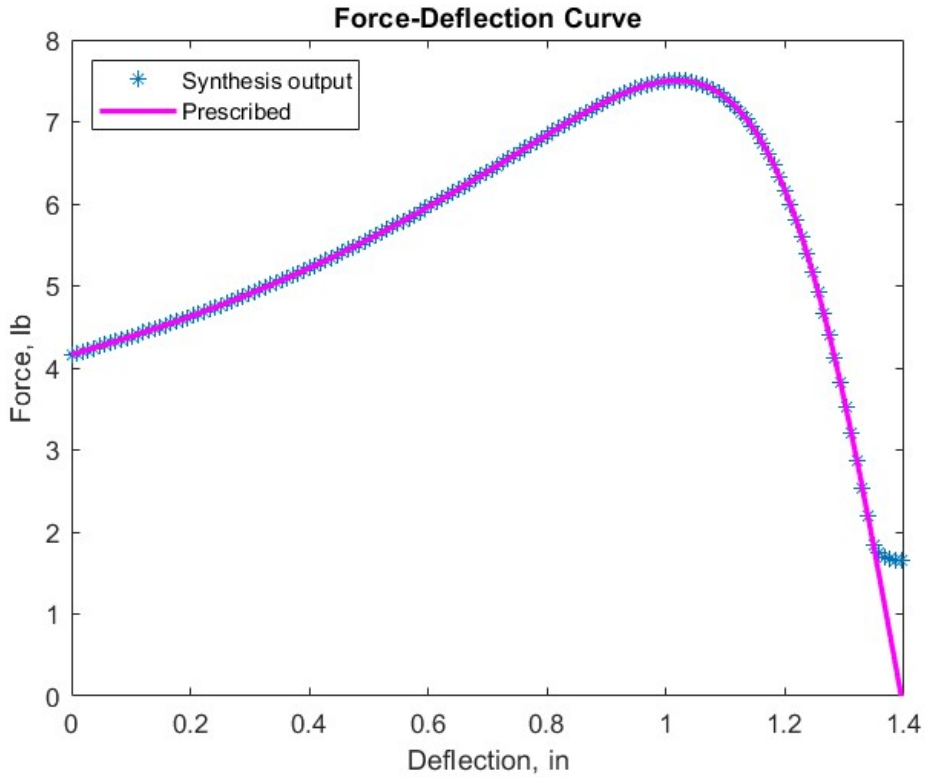

Figure 7.11 Comparison of Force- Deflection Profiles

Table 7.2 Input Variable Values

Variable	**Value**
E	30.5×10^6 psi
I	1.1068e-06 in^4
Θ_1	-5º
μ	0.1
γ	0.89
K_Θ	2.65
E	30.5×10^6 psi
l	1.75 in
w	0.85 in
t	0.025 in

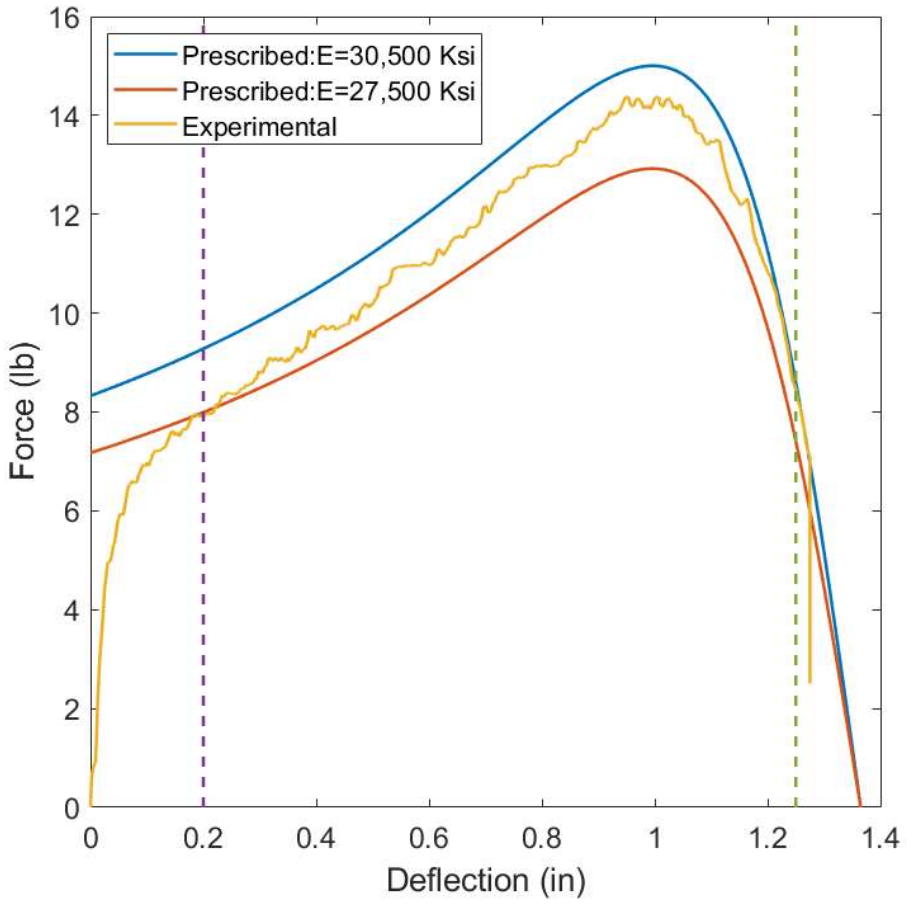

Figure 7.12 Experimental Results of Force- Deflection Profile for 15lb Force

To better understand the resultant force distribution better in the given scenario, the total force components are studied in Figure 7.12. The reaction force component N sin(α) contributes to more than 75% of the total force, and this force increases rapidly during the travel of the mechanism. However, the friction force component μNsin(α) also contributes to the total force. This analysis proves that the friction force component affects very minor to the total force of the mechanism. However, maintaining the cam's surface finish does affect the trend and smoothness of the resultant force-deflection profile. In order to control the surface finish, cam surface

machining methods have been explored in Section 7.2. The friction coefficient value between the cam material and the beam's rigid radius also plays a vital role in deciding the total frictional force. An increased friction value increases the total force output. In the current test setup, a coefficient friction value of 0.1 is used between aluminum cam and Delrin rigid radius. In the hand exerciser's final product, one must consider the frictional value closely to avoid the discrepancies in the output force-deflection profile.

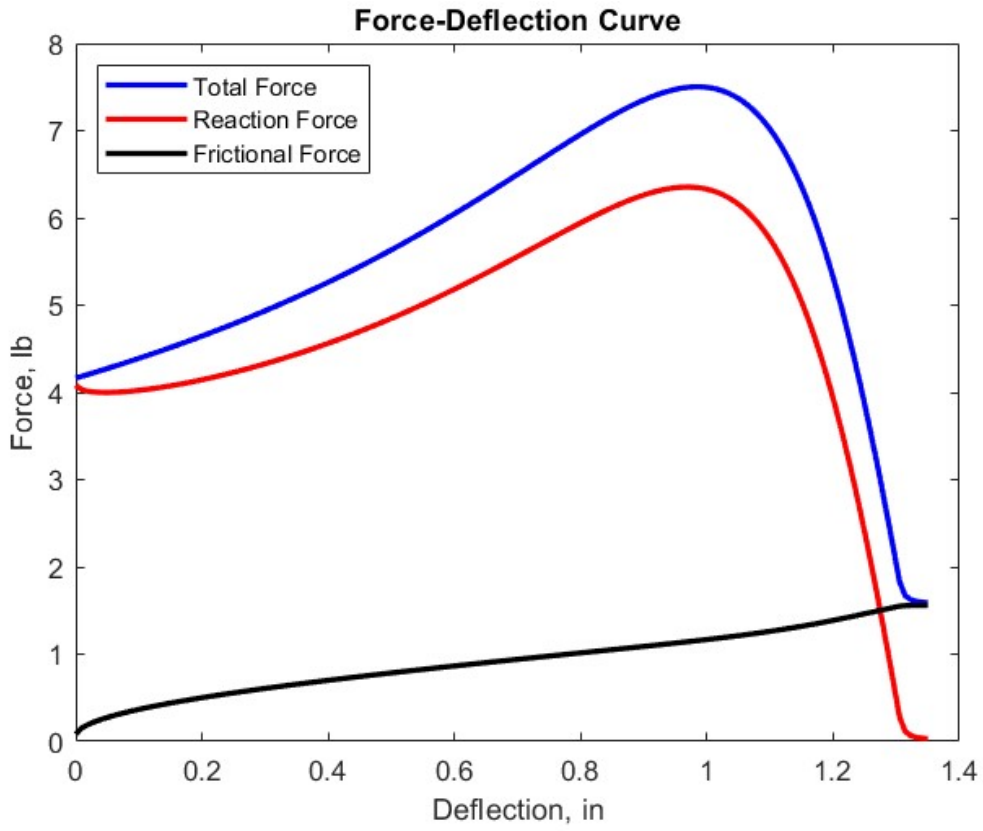

Figure 7.13 Total Force Distribution

7.5. PROTOTYPE DESIGN FOR HAND EXERCISER

The prototype design is chosen in conjunction with hand tools design guidelines to provide better grip and ease of use. The design is inspired by the SMINT® mint dispenser design. As seen in the below Figure 7.14, this is a 2-piece design with spring steel beams over-molded on the top piece, plunger. The cams are attached to the bottom piece, housing. The housing and plunger are always locked in position by the snap-fit. The snap-fit is chosen over other assembling methods because of advantages such as ease to assemble, cost-effective solution, and suitability for molding in any complex geometry.

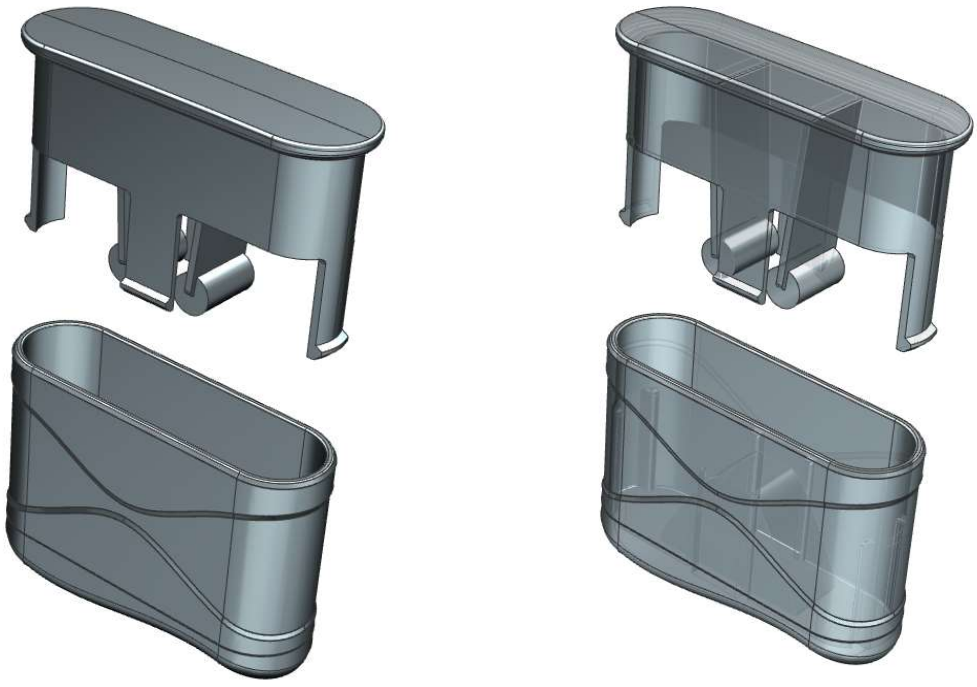

(a) (b)

Figure 7.14 Two-Piece Prototype Design (a) Normal View (b) Transparent View

When the snap fits are designed with proper thermoplastics, it produces better flexibility and sufficient rigidity [101]. Snap fits are also considered one of the quickest assembly methods. In the presented design, a cantilevered snap-fit design style is used; this eliminates the need for additional slides and reduces the molding complexity. 4 cantilevered beams snap the plunger and housing on four sides of the housing. To provide a linear motion to the beams during operation and also to avoid rotation, an additional set of guiding walls is provided in the housing. The snap-fit fingers/beams are designed to withstand the maximum resistance force during the operation without failing. The bottom face of the housing is designed to provide ergonomic support to the hand curvature. For the bottom curve design, a thorough literature survey is conducted on the effect of handle design during gripping action.

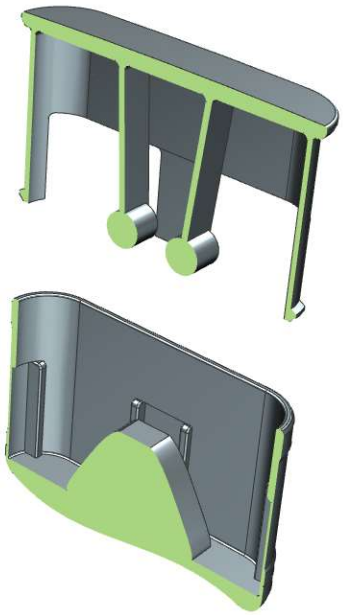

Figure 7.15 Sectional View of Two-Piece Prototype Design

In any hand tool design, the curvature of the handle also plays a vital role along with the handle diameter. Ergonomic handle curvature not only provides comfort but also improves gripping. The tool handle could be designed with a flat surface or with a profile. There are few studies [102] conducted to understand the relation between the curvature of the handle and comfort and effectiveness of the grip. According to [103,104], the handle curvature neither affected the muscle activities nor the comfort's qualitative measure. The combination of curvature used with the hand anthropometric data is an essential factor in determining the convenience of the hand devices. However, the subjective user data suggested that the comfort level is more with a curved profile over a flat surface [104]. The ergonomic hand tool design [104] indicates that to avoid any wrist deviation during gripping action, a curved handle design is more preferred. The handle curvature should match the curve of the palm of the hand for better griping. In the study of the laparoscopic tool handle [104], a curvature is developed for holding the handle at an angle of 45°. There are experimental studies [105] conducted for ergonomic handle designs. This study also suggests that increasing palm support would provide a better grip on the handle. Several manufacturers [106,107] in the market are currently following this approach in the hand tool industry.

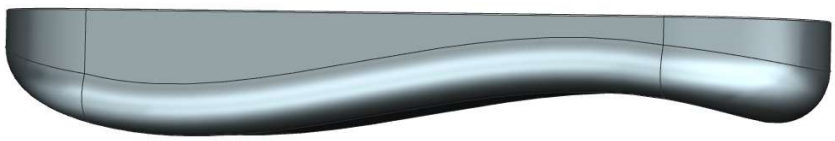

Figure 7.16 Curvature on Housing

Similarly, the top face of the plunger is designed to improve human hand gripping. To improve the grip on both top and bottom surfaces of the housing and plunger the bottom curvature on the housing shown in Figure 7.16 will be made out of thermoplastic elastomer material. This material is easy mold, offer slip resistance and good shock absorption [108]. Also, because of its soft touch appealing it is greatly used in consumer goods. Thermoplastic elastomers and thermoplastic polyurethanes are wildly popular material choices for medical applications of injection molding [109]. Each material offers excellent flexibility, dimensional stability and clarity [110]. By adding the TPE layer a soft cushioning effect can be added while performing the exercises.

The overall dimensions of the prototype are in accordance with hand tool design guidelines [87]. It is suggested that the span range of the two-handle tool should be between 3.5” to 5” to provide a comfortable operation. A design guideline also suggests utilizing the hand anthropometric data [88,89] of the users. According to [90], the tool's handle length should not be more than the sum of the thumb breadth and handbreadth. The details of the hand dimensions can be found from the anthropometric data of the hand [91]. By studying this, the limitation of (L x W x H) of the product – 4 in x 2 in x 3.5 in are defined. Followed by ergonomic design guidelines for hand tools, the overall dimensions of the prototype are obtained (3.35 in x 1.05 in x 3.2 in).

The material chosen for both plunger and housing is also essential to have properties such as low friction. The total resistance experienced by the user is not affected during device usage. The author suggests using the Delrin© [111] as the housing material, with outstanding flexibility and suitability for injection molding. Delrin© is

acetal resin thermoplastic with excellent frictional and wear properties, generally used in applications where lubricants are not desirable.

Figure 7.17 Assembled View of Prototype

Considering the application of the device, self-lubrication materials are preferred over adding an external lubricant. Also, to further reduce the friction, the Delrin can be filled with Teflon fibers, which have the lowest friction coefficient of all Delrin grades. The suggested plunger material is Zytel nylon resin©, which exhibits an outstanding abrasion resistance. Also, the reason for choosing is because of the low coefficient of friction value [111] of Delrin on Zytel 101©. The author believes that these two materials will provide the design with a low coefficient of friction and good wear and abrasion resistance from available material specifications.

8. CONCLUSIONS AND FUTURE WORK

8.1. CONCLUSIONS

Variable resistance hand exercisers are valuable and effective in resistance training rather than linear resistance hand exerciser discussed and presented in this thesis. Designing a variable force-deflection profile by studying the human hand behavior in the exercising device with utmost importance given to hand tool design guidelines and considering the factors such as anthropometric data is an added advantage over the current state of the art designs. The author also believes that this approach could be extended to various exercisers design by observing the human body part responses. As it is stated, if appropriately designed, these exercisers would provide a better mechanical advantage and ease of performing the exercises and can be more effective in the rehabilitation processes. Fortunately, a compliant mechanism is an effective way to provide a non-linear force-deflection profile over rigid-body mechanisms because compliant mechanisms are generally designed to generate resultant forces with displacement boundary conditions. This thesis presented a methodology to design a variable resistance hand exerciser with various force ranges.

The presented compliant mechanism consists of a rigid cam and compliant spring steel follower to generate the designer's required force-deflection. A computer algorithm proposed by Kyle is used to synthesize the cam surface. A novel PRBM approach is proposed to calculate the deflected beam profile during mechanism operation. The design variables are optimized such that the overall dimensions of the hand exerciser are within design limitations. The stresses generated in the beams are considered to avoid design

failure. The obtained results from the synthesis process are tested experimentally for two resistance values. The hand exerciser design is proposed for various force ranges from 3lb to 15lb. The force values are chosen from the current state of art devices.

Greater importance has been given to user comfort while designing the handle curvatures on the exerciser. The device can not only be used in the rehabilitation process of people affected by hand arthritis, but a person with normal hand condition can also use this as a handgrip strength improver.

8.2. FUTURE WORK

Future work on the hand exerciser should include expanding this idea as a potential market product. A thorough market survey has to be conducted to build a business case. Also, collaborating with the medical institutions for the prototyping trails would definitely provide more insight into design elements improvisation. The design is currently limited to a maximum of 15lb force, but this can be explored further to see the limitation on the approach. The thermoplastic materials with self-lubricating properties need to be closely studied. The ease of customization is an added advantage to this design; for further customizing the device, one can consider reviewing the force-deflection profile of an individual instead of selecting from the available ranges. By studying the hand's individual user force-deflection profile, the mechanism needs to be modified for required cam and beam parameters.

If the mechanism's overall sizes increase drastically for any given resistance value, one must consider modifying the current prototype design. Because the mechanism cannot be constrained to suggested dimensions, it will not fit the user's average palm size

and over-strain the muscle during operation, and the main goal of the design may not be achieved. To avoid that, the new design can retain the current ergonomic handle design, but the mechanism must be moved away from the palm, and force can be transferred through the handles. By designing so, one must also consider the overall weight not being increased drastically.

The suggested manufacturing method of the current process is insert molding of spring steel beams and injection molding. Before moving to the product's injection molding process, the option of soft tooling [112] is suggested to be explored. Injection molding [113] of the thermoplastics is manufactured using aluminum molds, which is an expensive process considering the mold's tooling and setup cost. If the product is designed by following the injection molding design guidelines [114], the parts can be produced with an accelerated manufacturing cycle and effective tooling. The durability of the mold is exceptional and expected to be able to produce hundreds of components with a controlled surface finish [115-117].

Soft tooling [112,113], in contrast, is a cost-effective approach compared to injection molding. But the expected part count with this method is limited to low to medium volume. The moldings of the soft tooling are generally not made with metals. Materials such as silicon, fiberglass, carbon fiber, etc., are used, which can produce a shot size of 25-50. Soft tooling's main advantages are the easy implementation of complex geometries and short lead times compared with hard tooling.

APPENDIX A.

TEST SETUP INFORMATION

For the test setup presented in Section 7.2, the below bill of material was created. The test-up is used to test two force-deflection profiles with maximum forces of 3lb and 15lb. The detailed components drawings are also presented in Table A.1.

Table A.1. Bill of Materials

Component	**Supplier**	**Part Number**	**Qty**
1075 Spring Steel Sheet (0.025" beam)	McMaster	9074K35	1
1076 Spring Steel Sheet (0.015" beam)	McMaster	9074K17	2
301 Steel Sheets (0.025" steel beam)	McMaster	2416K126	1
Delrin rod (Length 1ft)	McMaster	8579K14	1
#6-32 screws	McMaster	91735A150	1
1.5" x 1" x 6" Aluminum Stock (Cams)	McMaster	8975K52	1
1" x 4" Aluminum (Base & Top piece)	McMaster	8582K22	2
Steel shaft	McMaster		1

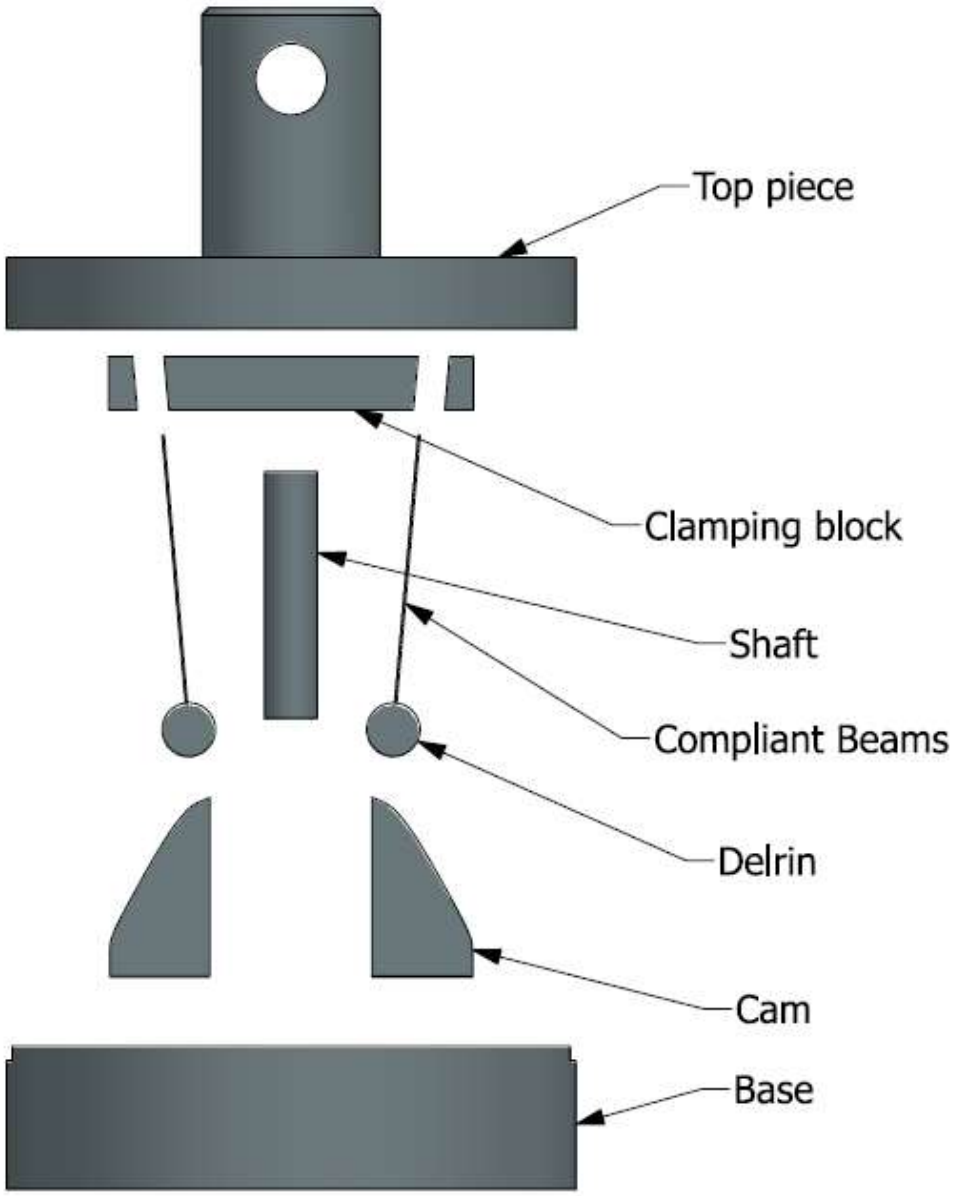

Figure A.1 Test Setup Exploded View

Figure A.2 Test Setup Exploded View

Base of the test setup machined as shown in Figure A.3. The base is designed such that it would fit in the UTM fixture.

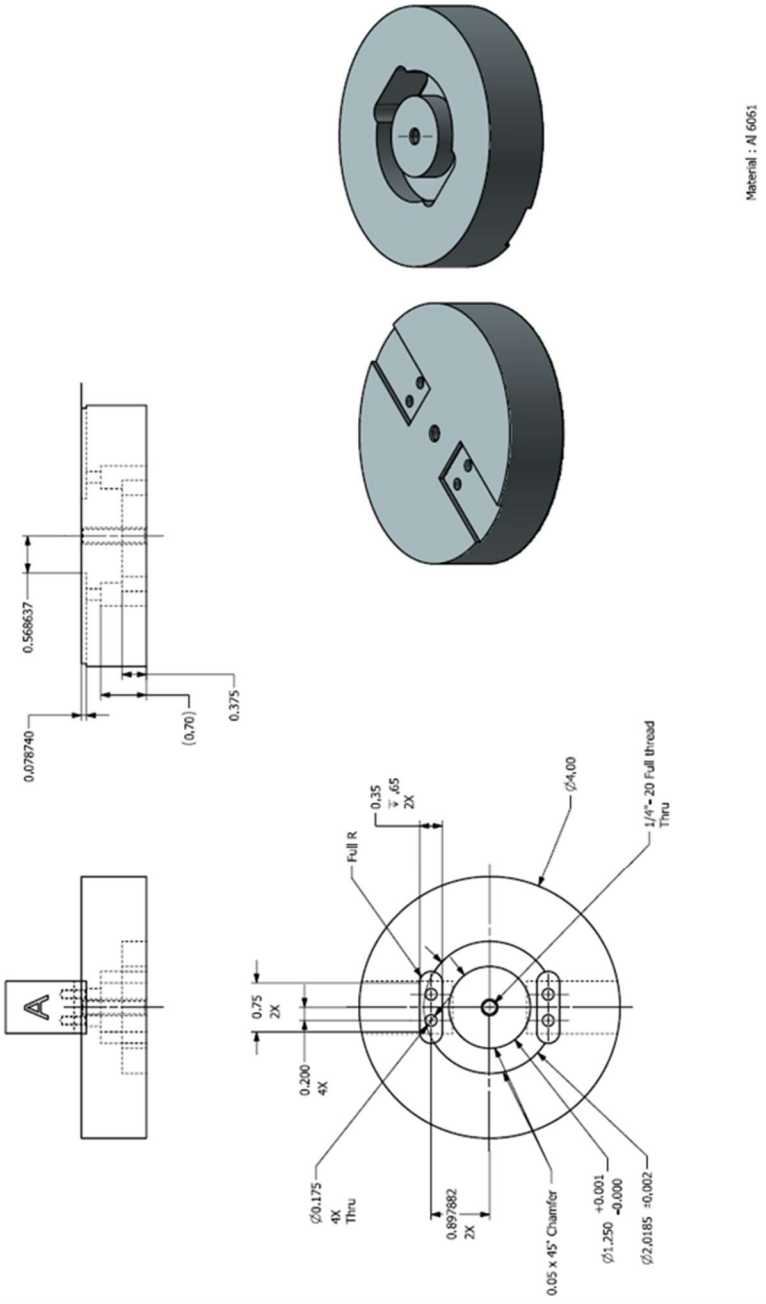

Figure A.3 Drawing of Base

Top piece of the test set up is machined as shown in Figure A.4. With the provision to add the UTM fixture pin on top.

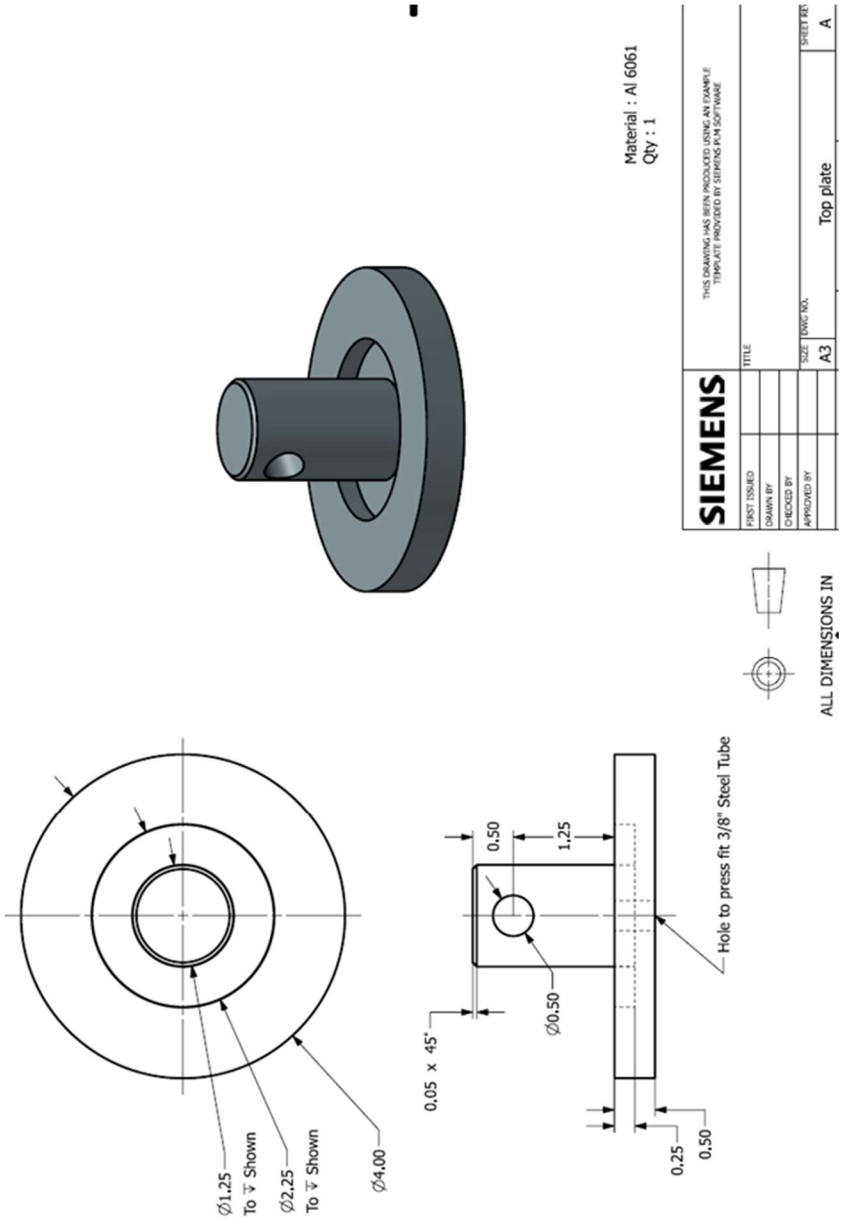

Figure A.4 Drawing of Top Piece

The clamping piece is machined to mount the beams at 5°. The outer clamping pieces have relief holes to mount the beams on the clamping piece. The clamping pieces are then pressed fit to the top piece using the shaft. The shaft is machined from a steel rod.

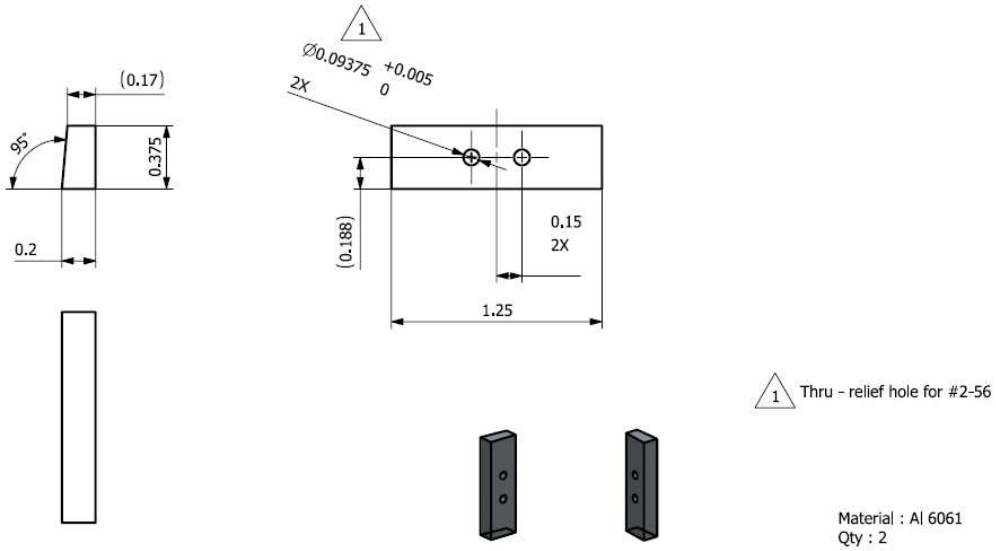

Figure A.5 Drawing of Clamping Piece

The center clamping piece is machined as per the beam positions obtained from the synthesis approach. The clamping piece in the current setup is attached to the top piece by a press-fit method. It is machined such that the beams are clamped at an initial angle. The threaded holes help clamp the flexible beams so that a cantilever effect is created at one end. The center hole was designed to mount a center shaft to guide the mechanism during mechanism operation. However, the guidance is removed to avoid the additional frictional forces.

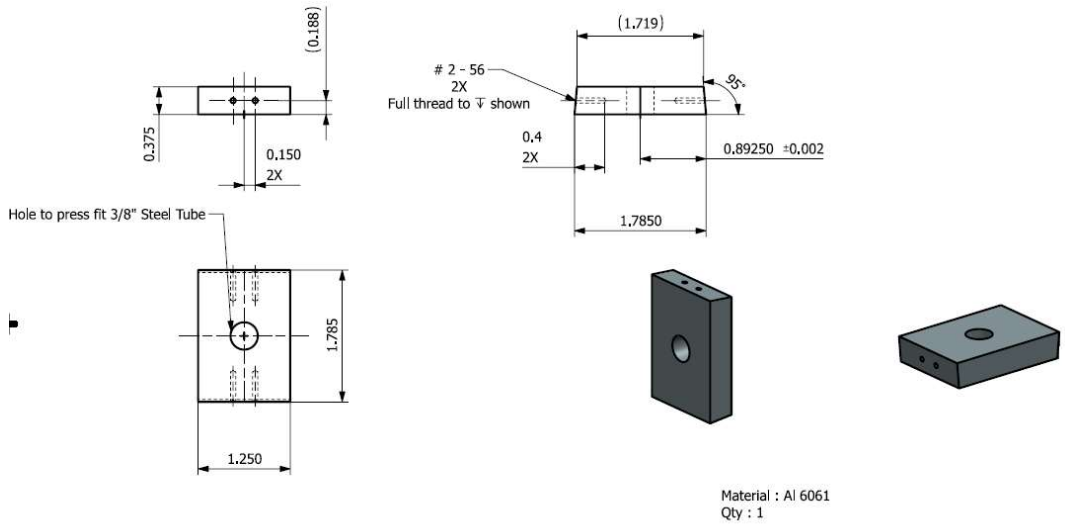

Figure A.6 Drawing of Center Clamping Piece

The cams are machined from aluminum stock to the required profile generated from synthesis.

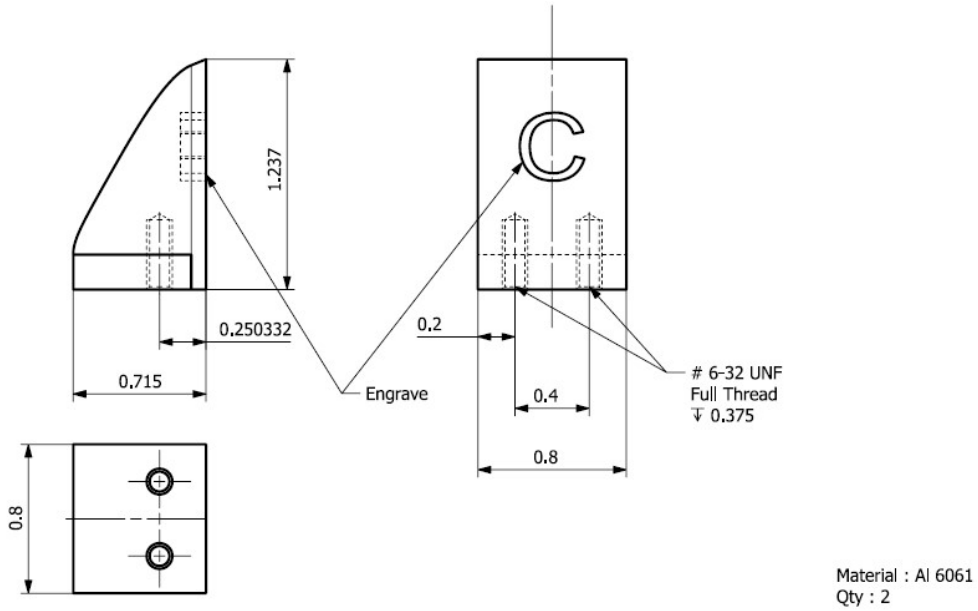

Figure A.7 Drawing of Cam

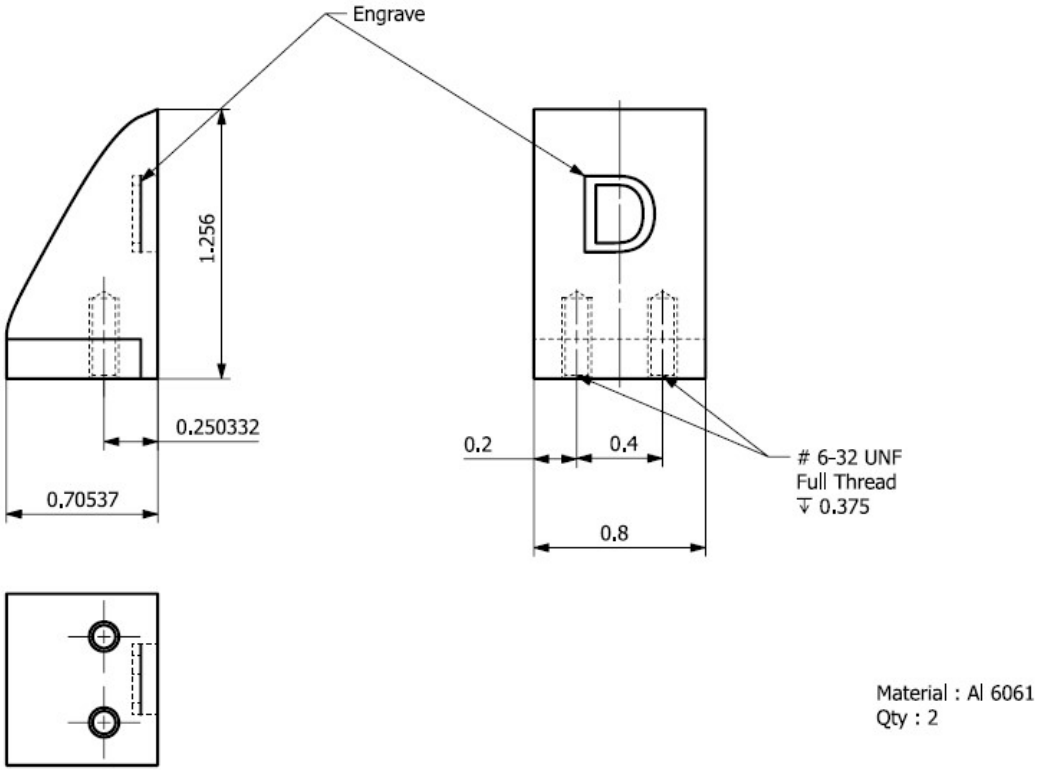

Figure A.8 Drawing of Cam

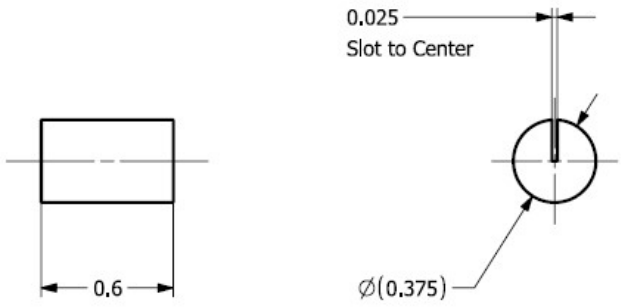

Figure A.9 Drawing of Delrin Rod

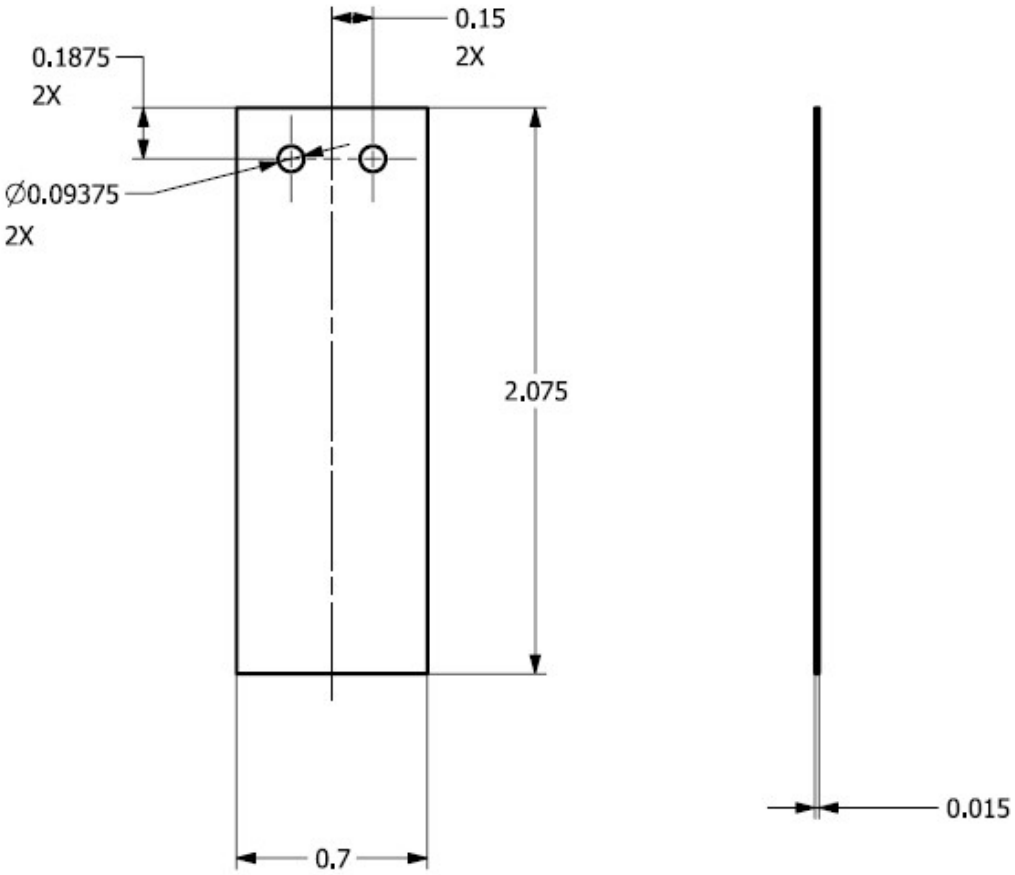

Figure A.10 Drawing of Spring Steel Beam

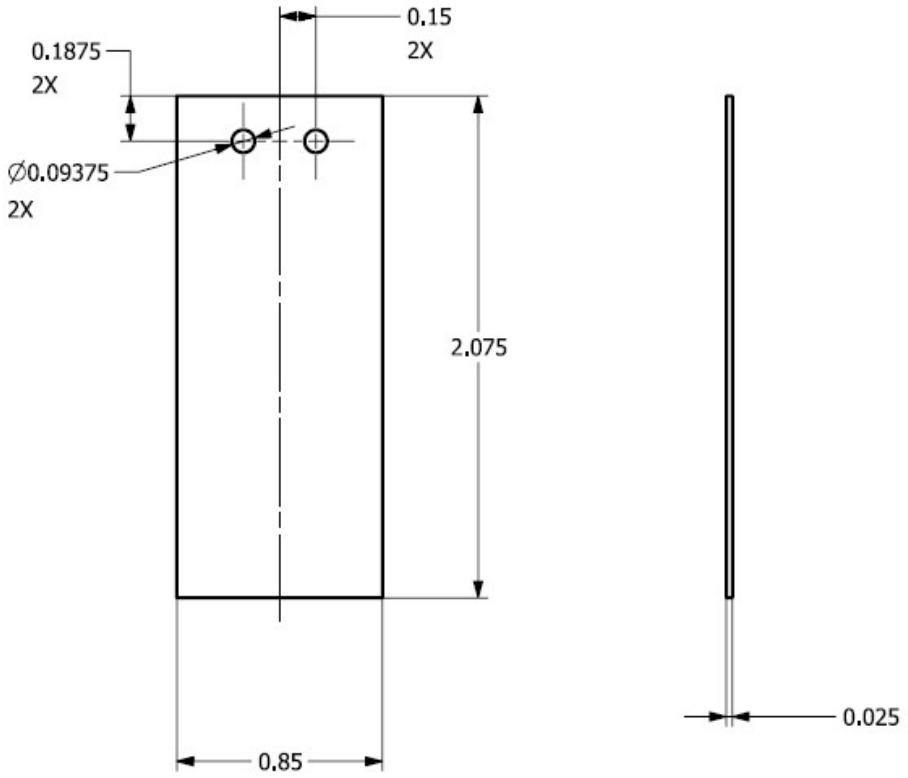

Figure A.11 Drawing of Spring Steel Beam

APPENDIX B.

PROTOTYPE INFORMATION

To analyze the snap fit assembly, the snap fit beam can be considered as a cantilever beam with overhand at one end. The amount of beam deflection then will depend upon the overhand depth of the beam. The entry and exit angles decide the ease or difficulty of the assembly. By modifying the angles, the assembly/disassembly forces can be optimized. The rigidity or strength of the beam can be increased by modifying the cross section or using a higher modulus material. The total assembly force will increase with maximum deflection of the beam and its stiffness. If the snap fit is designed with larger deflection, the beam stresses will also increase further increasing the total stress in the beam. This might result in the beam failure if the stress is above the material yield strength.

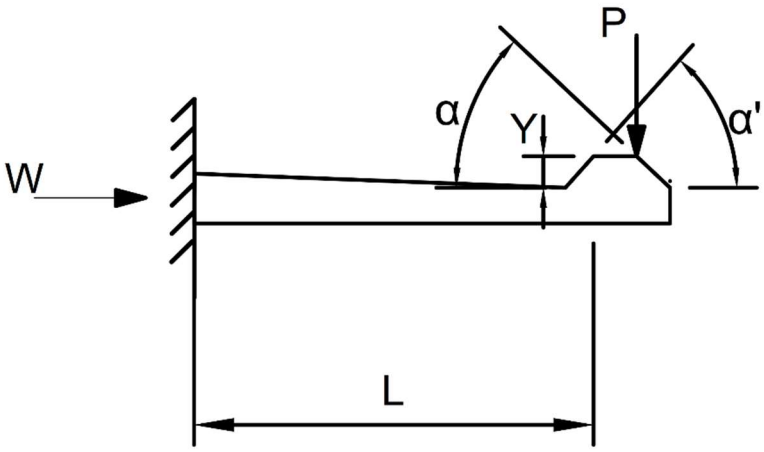

Figure B.1 Forces on Snap – Fit Assembly

The forces induced in the cantilever beam can be estimated by calculating the mating forces acting during assembly and maximum strain with the given deflection in the beam.

$$\varepsilon = 1.5\,\frac{tY}{L^2 Q} \tag{1}$$

$$W = P\frac{\mu + tan\alpha}{1 - \mu\, tan\alpha} \tag{2}$$

$$P = \frac{bt^2 E\varepsilon}{6L} \tag{3}$$

$$k = \frac{P}{Y} \tag{4}$$

where,

W – Mating force

P – force

μ - coefficient of friction

α- Lead angle

b – beam width

t – beam thickness

L- beam length

E – Flexural modulus

ε - strain

Q – deflection magnification factor

Y- deflection

However, the cantilever beam formulas consider the wall as rigid portion during deformation. This might not hold good for beams with length to thickness ratio greater than 10:1. A magnification factor [96] is applied to predict the total allowable deflection and strain for short beams. These factors values are verified by both finite element analysis and testing.

Since we have the current design maximum design to 15lbs, each beam on the prototype is designed to sustain the 15lb mating force without yielding. This value needs to be updated and considered for various force level requirements.

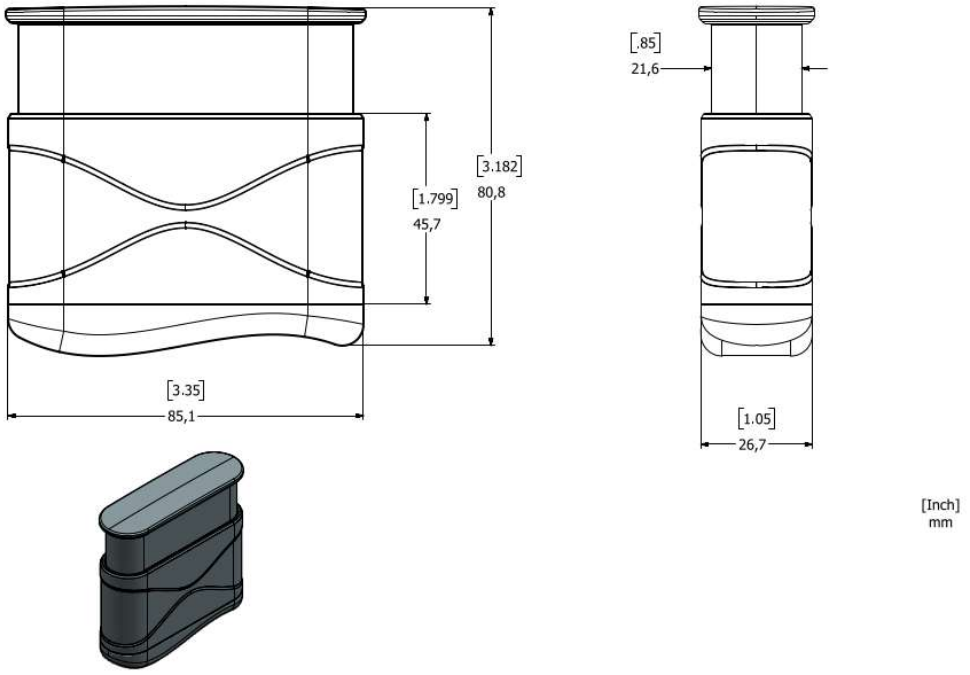

Figure B.2 Assembly Drawing of Prototype

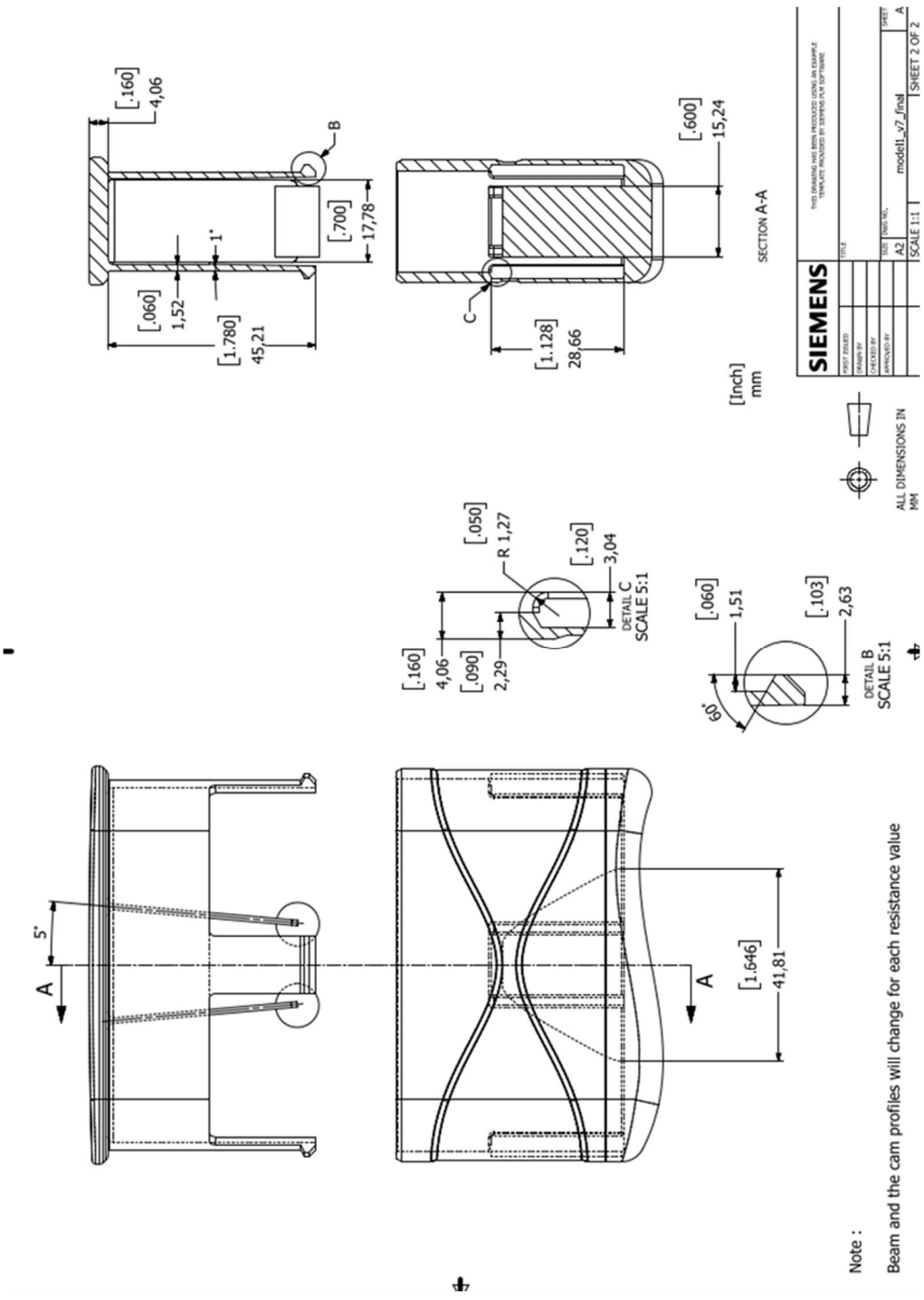

Figure B.3 Detailed Drawing of Prototype

APPENDIX C.

MATLAB CODE

The below programs can be used to generate the output force-deflection profile compared with the input prescribed force-deflection profile. Also, the total force is computed into both frictional force and normal force. The input beam parameters here can be entered manually or by performing the optimization routine. However, if the beam (input) parameters are known it is suggested to use the below code to avoid longer code executing time. The maximum force of the mechanism can be easily changed by modifying the below code.

```
% Program to verify the resultant force-deflection profiles and required cam shape {no optimization routine}
clc; clear all; close all.

   %Global variables
   global p; global FFreund;
   global dYf; global R2; global K; global thetaPre; global mu; global r;
   global theta; global alpha.

   %Segment 1: Defining Input Beam Parameters and Prescribed Force-Deflection Profile


   %How many elements should the cam surface be broken into?
   Elements=150;
   Travel=1.35;%
   %Defining travel increments
   dYf=Travel/Elements;
   dYfs=linspace(0, dYf*Elements,Elements+1);

   %PRBM Parameters (From Howell [31])
   gamma=0.89; %Characteristic radius factor
   Ktheta=2.65; %Stiffness Coefficient

   %Design Variables - Results from Optimization Routine
   width=0.8;%Width of beam
   thick=0.025;%Thickness of beam
   L=1.75; %Length of beam
   %%E=400000;
   E=30500000; %modulus of 1074 scaleless blue spring steel
   theta(1)=-5*pi/180; %Start angle (-5 is degrees. pi/180 converts to radians)
```

```
thetaPre=0.1*pi/180; % a small positive angle
mu=.1; %Coefficient of friction
r=0.1875; %Radius of small cylinder

% BEAM PARAMETERS
R2=L*gamma; %Pseudo-Rigid-Body length
      I=width*thick^3/12; %Cross-sectional Moment of Inertia of rectangular beam
K=gamma*Ktheta*E*I/L; %Torsional Spring Constant of PRBM



MaxForce=7.5; %Choose this based on strength of individual.
FFreund=@(D) MaxForce*(1.51*(1-D./Travel).^2+6.59*(1-D./Travel))./(13.7*(1-
D./Travel).^2+0.890); %Prescribed/ modified Freund function.



fprintf('Forces 1 and no Path info')

%Solving sum of moments around cam point for F32X of first position.
F32X(1)=(K*thetaPre-FFreund(0)*R2*sin(theta(1)))/(R2*cos(theta(1)));

%Solving system of 2 equations (sum of X forces and sum of Y forces) for
%alpha and N of first position.
alpha0andN0=fsolve(@(v) [F32X(1)+mu*v(2)*cos(v(1))-v(2)*sin(v(1));
-FFreund(0)+mu*v(2)*sin(v(1))+v(2)*cos(v(1))],[0;0]); %Structure:
([f1(vs);f2(vs)],[initial guesses for vs])
alpha(1)=alpha0andN0(1);
N(1)=alpha0andN0(2);

%Postprocessing. This is the first point on the cam surface.
PX(1)=-R2*sin(theta(1))+r*sin(alpha(1));
PY(1)=-R2*cos(theta(1))-r*cos(alpha(1));



%Initial guess for Forces 2 and Path A. fsolve uses initial guesses to
%help it solve.
aguess(2)=-2;
bguess(2)=1;
cguess(2)=-0.02;
thetaguess(2)=0.35;
F32Xguess(2)=-0.34;
Nguess(2)=0.16;
alphaguess(2)=0.83;

%Solver. Loops through for each element.
```

```
    for p=linspace(2,Elements+1,Elements)
        %p is for Node label. m is for Path label. Path 1 ends at Node 2.
        m=p-1;
        %To keep track of solutions in Command Window
        fprintf(['Forces ',num2str(p),' and Path ',num2str(m)])

        %Initial guesses
        x0(1)=aguess(m);
        x0(2)=bguess(m);
        x0(3)=cguess(m);
        x0(4)=thetaguess(p);
        x0(5)=F32Xguess(p);
        x0(6)=Nguess(p);
        x0(7)=alphaguess(p);

        %Solving with equations in ForcesPathP
        [SetResult, fval, exit, output] = fsolve(@Final_ForcesPathP_Freund_Metal,x0);

        %Recording results. Setting next initial guesses to be current results.
        a(m)=SetResult(1);          aguess(m+1)=a(m);
        b(m)=SetResult(2);          bguess(m+1)=b(m);
        c(m)=SetResult(3);          cguess(m+1)=c(m);
        theta(p)=SetResult(4);      thetaguess(p+1)=theta(p);
        F32X(p)=SetResult(5);       F32Xguess(p+1)=F32X(p);
        N(p)=SetResult(6);          Nguess(p+1)=N(p);
        alpha(p)=SetResult(7);      alphaguess(p+1)=alpha(p);
    end

        %Postprocessing. These are the points on the cam surface.
        PX=-R2*sin(theta)+r*sin(alpha);
        PY=-R2*cos(theta)-dYfs-r*cos(alpha);


figure %Cam surface figure
%For individual solutions on cam surface
hold on;
%For cam surface interpolated between individual solutions
for p=linspace(1,Elements,Elements)
    xs=linspace(PX(p),PX(p+1),50);
    plot(xs,a(p)+b(p).*xs+c(p).*xs.^2,'b','linewidth',2);
    Z(p,:)=xs; % Recording Cam x- coordinate values
    Z1(p,:)=a(p)+b(p).*xs+c(p).*xs.^2;  % Recording Cam Y- coordinate values
    hold on;
end
%For characteristic pivot at starting position
plot(0,0,'+R')
```

```
%Labelling plot, etc.
xlabel('X');
ylabel('Y');
axis([-2 2 -3.5 0.5]);
pbaspect([1 1 1]);


figure %Force comparison figure
%For each dYf, The forces at cam surface
plot(dYfs,N.*cos(alpha)+mu*N.*sin(alpha),'b','linewidth',2); % Recording totalforces
 mat(:,:)=N.*cos(alpha)+mu*N.*sin(alpha); % Recording Normal forces
 %mat1(:,:)=mu*N.*sin(alpha); % Recording frictional forces

hold on;
%What is prescribed force-deflection profile?
%   Compare magenta line with blue asterisks.
plot(dYfs,N.*cos(alpha),'r','linewidth',2); % Recording Normal forces
plot(dYfs,mu*N.*sin(alpha),'k','linewidth',2); % Recording frictional forces
mat2(:,:)=FFreund(dYfs);% Recording Prescribed forces
%Labelling plot, etc.
xlabel('Deflection, in');
ylabel('Force, lb');
title ('Force-Deflection Curve').
legend ('Total Force', 'Reaction Force', 'Frictional Force', 'location', 'northwest')
```

The below code can be used to run the optimization routine to find the beam parameters. The main purpose of the code is to limit the overall dimensions of the cam-follower mechanism such that overall dimensions of the prototype of are within the limitations. However, the execution time can be very long for this routine. Make sure run the code along with objective and constraint function of the optimization. Also, the optimization runs the inputs values from Solver function where the initial estimation of the optimization is used to synthesize the required force-deflection profile.

The Optimization Routine:

```
%Segment 1: OPTIMIZATION ROUTINE: Defining the Limits of the Optimization
%dv= [Width, Length]
x0 = [0.5,1]; % Initial point for DVs
```

```
xl = [0.25,0.25]; % Lower bound of DVs
xu = [0.85,2]; % Upper bound of DVs
options = optimoptions('fmincon','Display','iter','DiffMinChange',0.01);
[x,f] = fmincon('Final_Obj_Fun',x0,[],[],[],[],xl,xu,...
   'Final_Con_Fun',options);
format short e
% Display optimal point and objective
disp('     x1         x2     ');
disp([x(1), x(2)]);
```

The below objective and constraint functions defines the requirements of the optimization. There was no equality constraint provided to this function.

```
function p = Final_Obj_Fun (dv)

   [p,mPx]=Final_Solver (dv); %Obtaining the value for o.
   p=p; %Minimize o: the occurrence of mstress < Yield limit (0.8*YS)

end


function [g,h] = Final_Con_Fun_Freund_Metal(dv)
   %CONSTRAINTS
   [p,mPx]=Final_Solver_Freund_Metal(dv) %Obtaining the value for mPx
   g(1)=mPx-.25;
   h=[]; %No equality constraints.
end
```

The function to define the 7 synthesis equations

```
function fcns=Final_ForcesPathP_Freund_Metal(x0)


   global p; global FFreund;
   global dYf; global R2; global K; global thetaPre; global mu; global r;
   global theta; global alpha;


   %Section 1: DEFINE 7 UNKNOWNS
   A=x0(1);
   B=x0(2);
```

```
   C=x0(3);
   thetaK=x0(4);
   F32XK=x0(5);
   NK=x0(6);
   alphaK=x0(7);


   % DEFINE EQUATIONS (7)
   %Position of path at first position.
        fcns(1)=A+B*(-R2*sin(theta(p-1))+r*sin(alpha(p-1)))+C*(-R2*sin(theta(p-
       1))+r*sin(alpha(p-1)))^2+dYf*(p-2)+(R2*cos(theta(p-1))+r*cos(alpha(p-1)));
   %Slope of path at first position.
          fcns(2)=B+2*C*(-R2*sin(theta(p-1))+r*sin(alpha(p-1)))-tan(alpha(p-1));
   %Sum of moments around cam contact at second position.
       fcns(3)=K*(thetaPre+thetaK-theta(1))-FFreund(dYf*(p-1))*(R2*sin(thetaK)-
                   r*sin(alphaK))-F32XK*(R2*cos(thetaK)+r*cos(alphaK));
   %Sum of X forces at second position.
                    fcns(4)=F32XK+mu*NK*cos(alphaK)-NK*sin(alphaK);
   %Sum of Y forces at second position.
           fcns(5)=-FFreund(dYf*(p-1))+mu*NK*sin(alphaK)+NK*cos(alphaK);
   %Position of path at second position.
                      fcns(6)=A+B*(-R2*sin(thetaK)+r*sin(alphaK))+C*(-
     R2*sin(thetaK)+r*sin(alphaK))^2+(dYf*(p-1)+R2*cos(thetaK)+r*cos(alphaK));
   %Slope of path at second position.
                fcns(7)=B+2*C*(-R2*sin(thetaK)+r*sin(alphaK))-tan(alphaK);
end
```

The main function that connects the results from all sub routines and runs the optimization routine.

```
clc; clear all; close all;

   global p; global FFreund;
   global dYf; global dYfs; global R2; global thetaPre; global mu; global r;
   global a; global b; global c; global theta; global N; global alpha;
   global PX; global PY; global Elements;
   global StressReal; global S;

   global K;

%
% OPTIMIZATION ROUTINE:
%dv=[Width,Length];
x0 = [0.5,1];% Initial point for DVs
```

```
xl = [0.25,0.25];% Lower bound of DVs
xu = [0.85,2];% Upper bound of DVs
% Segment 2a: TO RUN OPTIMIZATION ROUTINE:
options = optimoptions('fmincon','Display','iter','DiffMinChange',0.01);
[x,f] = fmincon('Final_Obj_Fun_Freund_Metal',x0,[],[],[],[],xl,xu,...
   'Final_Con_Fun_Freund_Metal',options);
format short e
% Display optimal point and objective
disp('     x1         x2     ');
disp([x(1),x(2)]);



% TO RUN DIRECT ROUTINE:
x=[0.7,1.7];
Final_Solver (x);
StressRatio=StressReal/S;
mstress=max(abs(StressReal)) %Maximum Stress
mdisp=max(abs(PX)) %Maximum Displacement


figure %Cam surface figure

%For individual solutions on cam surface
hold on;
%For cam surface interpolated between individual solutions
for p=linspace(1,Elements,Elements)
   xs=linspace(PX(p),PX(p+1),50);
   plot(xs,a(p)+b(p).*xs+c(p).*xs.^2);
   hold on;
end

%For compliant beam shape profiles on the cam surface.
%Note: The PRBM pin joint should be at (0,0), not top of the compliant beam.
o=1;

%1 in front is to get start position. 5 others are from linspace.
for p=[1,linspace(30,Elements,Elements/30)]
   %Reflects from 180 degree FEA angle across vertical to energy-free angle.
   Angle0Transform=pi/2-theta(1)+thetaPre;
   %Final_Shape_Profile_Freund takes angular displacement relative to energy-free
angle
   [ax,trans]=Final_Shape_Profile_Freund_Metal(-R2*sin(theta(p+1)-(theta(1)-
thetaPre)));
   %Local x-coordinates of FEA beam transformed to global cartesian. Last
      %term gets top of beam where it needs to be since characteristic pivot at (0,0).
```

```
   xfea=-ax*cos(Angle0Transform)-trans*sin(Angle0Transform)+(1/0.89-
1)*R2*sin(theta(1)-thetaPre);
   %Local y-coordinates of FEA beam transformed to global cartesian.
      %Second-to-last term for finger deflection. Last term gets top of beam where it
needs to be.
   yfea=-ax*sin(Angle0Transform)+trans*cos(Angle0Transform)-dYf*(p)+(1/0.89-
1)*R2*cos(theta(1)-thetaPre);
   plot(xfea,yfea,'g');
   hold on;
   %If you want to plot the cylinders:
   th = 0:pi/50:2*pi;
   plot(xfea(length(trans))+r*cos(th),yfea(length(trans))+r*sin(th),'r')%Draws circles
around endpoints.
   hold on;

%Beams intersecting the cam surface:
   for n=1:length(trans)
      [ d, nCam ] = min( abs( PX-xfea(n) ) ); %nCam is the cam piece that had the
minimum.
         %d is just the minimum of the vector (placeholder/dummy)
      if (yfea(n) < PY(nCam))
         outsideP(o)=p;%This records the number of the specific beam that was the
perpetrator.
         o=o+1;
      end
   end
end

%Plot, etc.
xlabel('X');
ylabel('Y');
axis([-2 2 -4.5 0.5]);
pbaspect([1 1 1]);



figure %Force comparison figure
%For each dYf, Forces at cam surface
%plot(dYfs,N.*cos(alpha)+mu*N.*sin(alpha),'*');
xlabel('Displacement');
ylabel('Force');
title('Force-Displacement Curve');

K=K

%Alarm at the end of the optimization
```

```
for m=linspace(1,500,500)
   pause(1)
   beep
end
```

Element Stiffness matrix [Kattan]

```
function y = BeamElementStiffness (L)
y = [12 6*L -12 6*L ; 6*L 4*L*L -6*L 2*L*L ;
-12 -6*L 12 -6*L ; 6*L 2*L*L -6*L 4*L*L];
end
```

Assembled global stiffness matrix

```
function y = Final_Shape_BeamAssemble (K,k,i,j)
K(2*i-1,2*i-1) = K(2*i-1,2*i-1) + k(1,1);
K(2*i-1,2*i) = K(2*i-1,2*i) + k(1,2);
K(2*i-1,2*j-1) = K(2*i-1,2*j-1) + k(1,3);
K(2*i-1,2*j) = K(2*i-1,2*j) + k(1,4);
K(2*i,2*i-1) = K(2*i,2*i-1) + k(2,1);
K(2*i,2*i) = K(2*i,2*i) + k(2,2);
K(2*i,2*j-1) = K(2*i,2*j-1) + k(2,3);
K(2*i,2*j) = K(2*i,2*j) + k(2,4);
K(2*j-1,2*i-1) = K(2*j-1,2*i-1) + k(3,1);
K(2*j-1,2*i) = K(2*j-1,2*i) + k(3,2);
K(2*j-1,2*j-1) = K(2*j-1,2*j-1) + k(3,3);
K(2*j-1,2*j) = K(2*j-1,2*j) + k(3,4);
K(2*j,2*i-1) = K(2*j,2*i-1) + k(4,1);
K(2*j,2*i) = K(2*j,2*i) + k(4,2);
K(2*j,2*j-1) = K(2*j,2*j-1) + k(4,3);
K(2*j,2*j) = K(2*j,2*j) + k(4,4);
y = K;
end
```

Deformed beam shape profile [Kattan]

```
function [a,b] = Final_Shape_Profile (disp)
   %Define system (mesh)
   elements=800;
   nodes=elements+1;
    Ltot=1.7;
    L=Ltot/elements;
```

```
    kelement=Final_Shape_BeamElementStiffness_Freund_Metal(L);
    K=zeros(nodes*2,nodes*2);
    for n=linspace(1,elements,elements)
        K=Final_Shape_BeamAssemble_Freund_Metal(K,kelement,n,n+1);
    end


        %Delete first 2 rows/columns because cantilevered. Already know displacements.
    k=K([3:(nodes*2-2),nodes*2],[3:(nodes*2-2),nodes*2]);
    %Define Force Matrix
    F=zeros(nodes*2,1);
    F=disp*K(:,(nodes*2-1));
    f=F([3:(nodes*2-2),nodes*2],1);


    u=k\f;
    U=[0;0;u((1:(nodes*2-3-1)),1);disp;u((nodes*2-3),1)];



    a(1)=L;
    b(1)=U(1);
    theta(1)=U(2);
    for n=linspace(2,elements,elements-1)
        theta(n)=U(2*n);
        w(n)=U(2*n-1);
        a(n)=a(n-1)+L*cos(theta(n-1)); %Using displacement: (L^2-(w(n)-w(n-1))^2)^(1/2)
        b(n)=w(n);
    end
end


function [o,mPx] = Final_Solver (dv)

    global p; global FFreund;
    global dYf; global dYfs; global R2; global K; global thetaPre; global mu; global r;
    global a; global b; global c; global theta; global F32X; global N; global alpha;
    global PX; global PY; global Travel; global Elements;
    global StressReal; global S; global thick; global MaxForce; global I; global A;
    global oRecord; global MaxPxRecord; global dv1Record; global dv2Record;

    %Program to synthesize cam surface for arbitrary force-deflection profile


    Elements=150;
```

```
Travel=1.4;% From Freund curve
width=dv(1);
thick=0.015;
gamma=0.89;
Ktheta=2.65;
E=30500000; S=62000;
%E=400000; S=14000;%For Delrin
%E=30500000; S=62000;%For spring steel

%Design Variables
dYf=Travel/Elements; %Each hand increment is equal. Total travel is # in #/elements.
L=dv(2);
theta(1)=-5*pi/180
thetaPre=0.1*pi/180;
mu=.1;
r=0.1875;

R2=L*gamma;
      I=width*thick^3/12;
A=width*thick;
K=gamma*Ktheta*E*I/L;



MaxForce=1.5;
FFreund=@(D) MaxForce*(1.51*(1-D./Travel).^2+6.59*(1-D./Travel))./(13.7*(1-
D./Travel).^2+0.890); %Function from Freund's paper.



fprintf('Forces 1 and no Path info')

%Solving sum of moments around cam point for F32X of first position.
F32X(1)=(K*thetaPre-FFreund(0)*R2*sin(theta(1)))/(R2*cos(theta(1)));

%Solving system of 2 equations (sum of X forces and sum of Y forces) for
%alpha and N of first position.
alpha0andN0=fsolve(@(v) [F32X(1)+mu*v(2)*cos(v(1))-v(2)*sin(v(1));
-FFreund(0)+mu*v(2)*sin(v(1))+v(2)*cos(v(1))],[0;0]);
alpha(1)=alpha0andN0(1);
N(1)=alpha0andN0(2);

%Postprocessing. This is the first point on the cam surface.
PX(1)=-R2*sin(theta(1))+r*sin(alpha(1));
PY(1)=-R2*cos(theta(1))-r*cos(alpha(1));
```

```
%Initial guess for Forces 2 and Path A
aguess(2)=-2;%-15;
bguess(2)=1;%0.5;
cguess(2)=-0.02;%-0.006;
thetaguess(2)=0.35;%0.51;
F32Xguess(2)=-0.34;
Nguess(2)=0.16;%0.68;
alphaguess(2)=0.83;%0.19;

%Solver. Loops through for each element.
for p=linspace(2,Elements+1,Elements)
   %p is for Force label. m is for Path label. Path 1 ends at Force 2.
   m=p-1;
   %To keep track of solutions in Command Window
   fprintf(['Forces ',num2str(p),' and Path ',num2str(m)])

   %Initial guesses
   x0(1)=aguess(m);
   x0(2)=bguess(m);
   x0(3)=cguess(m);
   x0(4)=thetaguess(p);
   x0(5)=F32Xguess(p);
   x0(6)=Nguess(p);
   x0(7)=alphaguess(p);

   %Solving with equations in ForcesPathP
   [SetResult, fval, exit, output] = fsolve(@Final_ForcesPathP_Freund_Metal,x0);

   %Recording results. Setting next initial guesses to be current results.
   a(m)=SetResult(1);            aguess(m+1)=a(m);
   b(m)=SetResult(2);            bguess(m+1)=b(m);
   c(m)=SetResult(3);            cguess(m+1)=c(m);
   theta(p)=SetResult(4);        thetaguess(p+1)=theta(p);
   F32X(p)=SetResult(5);         F32Xguess(p+1)=F32X(p);
   N(p)=SetResult(6);            Nguess(p+1)=N(p);
   alpha(p)=SetResult(7);        alphaguess(p+1)=alpha(p);
end

   %Vector of all dYfs.
   dYfs=linspace(0,dYf*Elements,Elements+1);

   %Postprocessing. These are the points on the cam surface.
   PX=-R2*sin(theta)+r*sin(alpha);
   PY=-R2*cos(theta)-dYfs-r*cos(alpha);
   mPx=max(PX);
```

```
    %Postprocessing. These are measurements for optimization.
    F=F32X;
    n=FFreund(dYfs)./F;
    ain=0.11/0.89*R2-dYfs-PY;
    bin=-PX;
    StressReal=6*F.*(ain+n.*bin)/(width*thick^2)+n.*F/A;



  %Note: The PRBM pin joint should be at (0,0), not the top of the compliant beam.
  o=1;
  for p=[1,linspace(10,Elements,Elements/10)] %1 in front is to get start position. 5 others are from linspace.
      Angle0Transform=pi/2-theta(1)+thetaPre; %This is to get from 180 degree angle for FEA reflected across vertical to initial, energy free angle.
      [ax,trans]=Final_Shape_Profile_Freund_Metal(-R2*sin(theta(p+1)-(theta(1)-thetaPre)));%Final_Shape_Profile_Freund takes transverse displacement (angular displacement relative to energy-free angle)
      xfea=-ax*cos(Angle0Transform)-trans*sin(Angle0Transform)+(1/0.89-1)*R2*sin(theta(1)-thetaPre);%Local x-coordinates of FEA beam transformed to global cartesian. Last term is getting top of beam where it needs to be since characteristic pivot at (0,0).
      yfea=-ax*sin(Angle0Transform)+trans*cos(Angle0Transform)-dYf*(p)+(1/0.89-1)*R2*cos(theta(1)-thetaPre);%Local y-coordinates of FEA beam transformed to global cartesian. Second-to last term accounts for finger deflection. Last term is getting top of beam where it needs to be.

          for w=1: length(trans)
        [ d, nCam ] = min( abs( PX-xfea(w) ) ); %nCam is the cam piece that had the minimum. d is just the minimum of the vector (placeholder/dummy)
        if (yfea(w) < PY(nCam))
          outsideP(o)=p; %This records the number of the specific beam that was the perpetrator.
          o=o+1;
        end
      end
  end

  oRecord=[oRecord,o];
  MaxPxRecord=[MaxPxRecord,mPx];
  dv1Record=[dv1Record, dv(1)];
  dv2Record=[dv2Record, dv(2)];
end
```

BIBLIOGRAPHY

[1] Midha, Ashok, Her, Innchyn, and Salamon, B. A. "A Methodology for Compliant Mechanism Design: Part I – Introduction and Large-Deflection Analysis." *Proceedings of the 18th ASME Design Automation Conference, DE-Vol.44-2: Advances in Design* Automation. (1992): pp. 29-38.

[2] Midha, Ashok, Norton, Tony W., and Howell, Larry L. "On the Nomenclature, Classification and Abstractions of Compliant Mechanisms," *ASME Journal of Mechanical Design* Vol. 116 No. 1 (1994): pp. 270-279.

[3] Euler, Leonhard, "chapter Additamentum 1." Methodus inveniendi lineas curvas maximi minimive proprietate gaudentes, sive solutio problematis isoperimetrici lattissimo sensu accepti, eulerarchive.org E065. (1744).

[4] Bisshopp, K. E., and Drucker, D. C., "Large-defection of Cantilever Beams," *Quarterly of Applied Mathematics*, vol. 3, no. 3, (1945): pp. 272-275.

[5] Shoup, T. E., "On Analytical Investigations of the Large-Deflections of Flexible Beam Spring," Ph.D. Dissertation, The Ohio State University, Columbus, OH. 1969.

[6] Burns, R. H., "The Kinetostatic Synthesis of Flexible Link Mechanisms," Ph.D. Dissertation, Yale University, New Haven, CT. 1964.

[7] Burns, R. H., and Crossley, F. R. E., "Kinetostatic Synthesis of Flexible Link Mechanisms," *ASME Paper 68-MECH-36*. Atlanta, Ga. (1968).

[8] Midha, A., and Kuber, R., "Closed-Form Elliptic Integral Solution for Initially-Straight and Initially-Curved Small-Length Flexural Pivots," *Proceedings of the ASME 2014 International Design Engineering Technical Conferences & Computers and Information in Engineering Conference*, (2014): pp. DETC35268-1-7.

[9] Zhang, A., and Chen, G., "A Comprehensive Elliptic Integral Solution to the Large Deflection Problems of Thin Beams in Compliant Mechanisms," *Journal of Mechanisms and Robotics, Trans. ASME*, vol. 5, no. 1, (2013): pp. 021006-1-10.

[10] Midha, A., and Her, I., Research Notes, Purdue University, West Lafayette, IN. (1985).

[11] Salamon, B. A., and Midha, A., "An Introduction to Mechanical Advantage in Compliant Mechanisms," *ASME J Mech. Design*, 120(1), (1998): pp. 311-315.

[12] Salamon, B. A., "Mechanical Advantage Aspects in Compliant Mechanisms Design," MS Thesis, Purdue University, West Lafayette, IN. 1989.

[13] Howell, L. L., and Midha, A., "Parametric Deflection Approximations for End-Loaded, Large Deflection Beams in Compliant Mechanisms," *ASME J Mech. Design*, 117(1), 1995): pp. 156-165.

[14] Howell, L. L., Midha, A., and Norton, T. W., "Evaluation of Equivalent Spring Stiffness for Use in a Pseudo-Rigid-Body Model of Large-Deflection Compliant Mechanisms," *ASME J Mech. Design*, 118(1), (1996): pp. 126-131.

[15] Howell, L. L., "A Generalized Loop-Closure Theory for the Analysis and Synthesis of Compliant Mechanisms," Ph.D. Dissertation, Purdue University, West Lafayette, IN. 1993.

[16] Pauly, J., and Midha, A., "Improved Pseudo-Rigid-Body Model Parameter Values for End-Force-Loaded Compliant Beams," *Proceedings of the IDETC/CIE. DETC2004-57580: pp. 1513-1517*. Salt Lake City, UT, September 28 - October 2, 2004.

[17] Midha, A., and Kuber, R., "Closed-Form Elliptic Integral Solution of Initially-Straight and Initially-Curved Small-Length Flexural Pivots," *Proceedings of the IDETC/CIE. DETC2014-35268: pp. V05AT08A044, 1-7*. Buffalo, NY, August 17-20, 2014.

[18] Howell, L. L., and Midha, A., "A Method for the Design of Compliant Mechanisms with Small-Length Flexural Pivots," *ASME J Mech. Design, 116(1*), (1994): pp. 280-290.

[19] Howell, L. L., and Midha, A., "A Loop-Closure Theory for the Analysis and Synthesis of Compliant Mechanisms," *ASME J Mech. Design, 118(1),* (1996): pp. 121-125.

[20] Midha, A., Annamalai, Y., Kolachalam, S. K., Bapat, S. G., and Koli, A. B., "On a Compliant Mechanism Design Methodology using the Synthesis with Compliance Approach for Coupled and Uncoupled Systems," *Advances in Mechanisms, Robotics, and Design Education and Research*. Kumar V., Schmiedeler J., Sreenivasan S., Su HJ., eds., Springer, Heidelberg, Germany, (2013): pp. 95-116.

[21] Bapat, S. G., Midha, A., and Koli, A. B., "On a Generalized Approach for Design of Compliant Mechanisms Using the Pseudo-Rigid-Body Model Concept," *Proceedings of the IMECE,* IMECE2014-38788: pp. V014T06A001, 1-11. Montreal, Quebec, Canada, November 14-20, 2014.

[22] Murphy, M. D., "A Generalized Theory for the Type Synthesis and Design of Compliant Mechanisms," Ph.D. Dissertation, Purdue University. 1993.

[23] Howell, Larry L., Midha, Ashok, and Murphy, Morgan D. "Dimensional Synthesis of Compliant Constant-Force Slider Mechanisms." *Proceedings of the ASME Design Engineering Technical Conferences, DE-Vol. 71: 23rd Biennial Machine Elements and Machine Dynamics*. pp. 509-515. New York, NY, June 1994.

[24] Midha, Ashok, Murphy, Morgan D., and Howell, Larry L. "Compliant Constant-Force Mechanism and Devices Formed Therewith." *US Patent 5649454*. 1997.

[25] Howell, L. L., and Magleby, S. P., "Substantially Constant-Force Exercise Machine," *US Patent 7060012*. 2006.

[26] Karthik, K., "On the Design of A Nearly Constant-Force Modular Device Based on A Compliant Slider Mechanism," MS Thesis, Missouri University of Science and Technology, Rolla, MO. 2015.

[27] Christian, A. J., "On the Dynamic Analysis of Compliant Mechanisms Based on the Pseudo-Rigid-Body Model," MS Thesis, Missouri University of Science and Technology, Rolla, MO. 2015.

[28] Midha, A, Lodagala, V, Bagivalu Prasanna, P, & Komatireddy, J. "A Primal Treatise of Constant-Force, Compliant Segments, and Mechanisms." *Proceedings of the ASME 2020 International Design Engineering Technical Conferences and Computers and Information in Engineering Conference*. *Volume 10: 44th Mechanisms and Robotics Conference (MR)*. Virtual, Online. August 17–19, 2020. V010T10A016. ASME. https://doi.org/10.1115/DETC2020-22761

[29] Jutte, C. V., and Kota, S., "Design of single, multiple, and scaled nonlinear springs for prescribed nonlinear responses," *Journal of Mechanical Design*, Trans. ASME, vol. 132, no. 1, (2010): pp. 011003-1-011003-10.

[30] Jutte, C. V., "Generalized Synthesis Methodology of Nonlinear Springs for Prescribed Load-Displacement Functions," Ph.D. Dissertation, The University of Michigan, Ann Arbor, MI, 2008.

[31] Howell, L. L., *Compliant Mechanisms*, John Wiley & Sons Inc., New York, NY. 2001.

[32] "Michelin X Tweel Airless Radial Tire," last modified December 2020, accessed October 2020, www.michelintweel.com

[33] "The Mars Curiosity Rover Wheels and Legs," last modified on August 20, 2019, accessed January 20, 2020. https://mars.nasa.gov/msl/spacecraft/rover/wheels/

[34] "Adidas Springblade: Shoes with Actual Springs Might Be a Good Idea," last modified on June 2013, accessed January 2, 2018. https://www.gizmodo.com.au/2013/06/adidas-springblade-shoes-with-actual-springs-might-be-a-good-idea/

[35] Mettlach, G. A., Khanuja, S. S., and Midha, A., "Design of an Ergonomic Compliant Modular Chair," Proceedings of 4th National Applied Mechanisms and Robotics Conference, December, (1995): pp. AMR95-009-1-10.

[36] Halverson, Peter A., Bowden, Anton E., and Howell, Larry L. "A Compliant-Mechanism Approach to Achieving Specific Quality of Motion in a Lumbar Total Disc Replacement." *International Journal of Spine Surgery* Vol. 6 (2012): pp. 78-86.

[37] Davidson, Martha. "Innovative Lives: Artificial Parts – Van Phillips." created on March 9, 2005, last modified on April 14, 2016, and accessed on January 5, 2020. https://invention.si.edu/innovative-lives-artificial-parts-van-phillips

[38] Ossur hf. "Flex-Foot Cheetah." *Master Prosthetic Catalog 2016 of Ossur hf*. last modified on June 25, 2018, accessed on January 5, 2020. https://assets.ossur.com/library/39389/Flex-Foot%20Cheetah%20Catalog%20page%20-%202018.pdf

[39] "TED Speaker Nikolai Begg." last modified on March 13, 2021, accessed on January 5, 2020. https://www.ted.com/speakers/nikolai_begg

[40] Rutter, Bryce G. "The Human Hand," *The Hand*. Quarterly of Industrial Designers Society of America (2015): pp. 20-25.

[41] Katz, S., Ford, A. B., Moskowitz, R. W., Jackson, B. A., and Jaffe, M. W., "Studies of Illness in the Aged," *The Journal of the American Medical Association,* vol. 185, no. 12, (1963): pp. 94-99.

[42] Freund, Jouni, Toivonen, Risto, and Takala, Esa-Pekka. "Grip Forces of the Fingertips." *Clinical Biomechanics,* Vol. 17 (2002): pp. 515-520.

[43] "Osteoarthritis of the Hand," last modified December 9, 2019, accessed January 20, 2019.https://myhealth.alberta.ca/Health/pages/conditions.aspx?hwid=zm6124

[44] "Rheumatoid Arthritis vs. Osteoarthritis of the Hand Symptoms, Diagnosis, Prognosis, Treatments," last modified May 24, 2017, accessed February 20, 2019. https://cookwithkathy.wordpress.com/2017/05/24/rheumatoid-arthritis-vs-osteoarthritis/

[45] "Health day article: 4 in 10 Suffer from Arthritic Hands Over Time," last modified May 4, 2017, accessed February 4, 2019. https://consumer.healthday.com/senior-citizen-information-31/misc-arthritis-news-41/4-in-10-people-will-suffer-arthritic-hands-over-lifetime-722378.html

[46] "7 Hand Exercises to Ease Arthritis Pain," last modified on June 17, 2020, accessed January 2, 2019.https://www.healthline.com/health/osteoarthritis/arthritis-hand-exercises

[47] "Forty Percent of People Will be Affected by Symptomatic Hand Osteoarthritis," last modified on May 16, 2017, accessed February 2, 2020. https://arthritisbroadcastnetwork.org/2017/05/forty-percent-of-people-will-be-affected-by-symptomatic-hand-osteoarthritis/

[48] "Exercise: An effective prescription for joint pain," last modified on June 17, 2020, accessed January 2, 2019.https://www.health.harvard.edu/pain/exercise-an-effectiveprescription-for-joint-pain

[49] "Synovial Fluid," last modified on March 22, 2012, accessed January 2, 2019. https://www.orthopaedicsone.com/display/Main/Synovial+fluid

[50] "5 Simple Ways to Manage Hand Arthritis," last modified on June 23, 2020, accessed January 20, 2019. https://www.arthritis-health.com/blog/5-simple-ways-manage-hand-osteoarthritis

[51] "Hand Strengthening Exerciser Equipment." last modified on July 9, 2020, accessed February 2, 2020. https://www.rehab-store.com/c-hand-exercisers.html

[52] "Hand Therapy Putty Exercises." last modified on November 16, 2020, accessed February 12, 2020. https://www.flintrehab.com/2016/hand-therapy-putty-exercises/

[53] "Patterson Medical Supply Replacement Hand Exerciser Bands Ultimate Hand Helper," last modified on September 22, 2019, accessed February 1, 2020. https://www.devineexpress.com/products/925305-patterson-medical-supply-replacement-hand-exerciser-bands-ultimate-hand-helper?variant=15652903780395&cmp_id=403238383&adg_id=1345802770256574&kwd=&device=c&msclkid=4781d00fa6f61b43c81f8fab67648ffb

[54] "Arthritis Pain Reliever, Hand Strengthening Xtensor Pain Relief Device," last modified on January 1, 2021, accessed February 8, 2020. http://healiohealth.com/products/index/5032

[55] "Fitmotion Hand Exerciser Band," last modified on August 20, 2020, accessed March 8, 2020. http://www.juskeepsmile.net/2017/09/fitmotion-hand-exercise-band-latex-free.html

[56] "Cando Digi-Flex Finger Exerciser & Hand Exerciser," last modified on January 5, 2021, accessed February 12, 2020. https://www.allegromedical.com/gift-ideas-c573/digi-flex-exercise-rehabilitation-system-p191759.html?CS_003=9164468&CS_010=8ab281020bb66dff010bb67e1ffe5383&msclkid=7cbd7911458d1bfef8e326b58795f0a6&utm_source=bing&utm_medium=cpc&utm_campaign=(ROI)%20Shopping-%20All%20Products&utm_term=4581046480690733&utm_content=All%20Products&adlclid=7cbd7911458d1bfef8e326b58795f0a6#121D-1213F8E

[57] "5 Best Arthritis Gloves on The Market," last modified on August 6, 2020, accessed March 18, 2020.https://www.healthline.com/health/best-arthritis-gloves#imak-arthritis-gloves

[58] "Finger strength helper," last modified on August 20, 2020, accessed March 8, 2020. https://www.amazon.com/Sammons-Preston-Rehabilitation-Strengthening-Resistance/dp/B071VC7LF3/ref=sr_1_6?crid=2C6QG47XTHCS&dchild=1&keywords=thumb+exerciser&sprefix=thumb+exerc%2Caps%2C177&sr=8-6

[59] Xu, Zhe. "Approaching Human Hand Dexterity Through Highly Biomimetic Design." *Human Inspired Dexterity in Robotic Manipulation*, Academic Press, (2018): pp. 87-114.

[60] "Tendons," last modified on June 1, 2021, accessed June 13, 2020, https://www.assh.org/handcare/safety/tendons

[61] "Muscles of Hand and Wrist," last modified on February 07, 2020, accessed June 13, 2020, https://boneandspine.com/muscles-of-hand-and-wrist/

[62] "Hand," last modified on November 24, 2020, accessed June 13, 2020, https://www.lecturio.com/concepts/hand/

[63] "Soft Tissues of the Wrist," last modified on March 26, 2020, accessed June 13, 2020, https://boneandspine.com/muscles-of-hand-and-wrist/

[64] "Superficial posterior forearm muscles," last modified on March 26, 2020, accessed June 13, 2020, https://www.kenhub.com/en/library/anatomy/the-superficial-extensors-of-the-forearm

[65] Feix, Thomas, Romero, Javier, Schmiedmayer, Heinz-Bodo, Dollar, Aaron M., and Kragic, Danica. "The GRASP Taxonomy of Human Grasp Types," in *IEEE Transactions on Human-Machine Systems*, Vol. 46 No. 5 (2016): pp. 66-77. DOI: 10.1109/THMS.2015.2470657.

[66] Shahid, Talha, Gouwanda, Darwin, Nurzaman, Surya G., and Gopalai, Alpha A. “Moving toward Soft Robotics: A Decade Review of the Design of Hand Exoskeletons.” *Biomimetics* Vol. 3(3):17 (2018). DOI. https://doi.org/10.3390/biomimetics3030017

[67] “Understanding Hand Exercise & Grip Strength,” last modified on February 07, 2020, accessed June 13, 2020, https://www.kenhub.com/en/library/anatomy/the-superficial-extensors-of-the-forearm

[68] “Body Basics,” last modified on June 1, 1998, accessed June 13, 2020, https://waergo.com/JES/BodyBasics.htm

[69] Vigouroux, Laurent, Quaine, Franck, Labarre-Vila, Annick and Moutet, François. “Estimation of finger muscle tendon tensions and pulley forces during specific sport-climbing grip techniques.” *Journal of biomechanics*. Vol. 39 (2006): pp. 2583-92. DOI: 10.1016/j.jbiomech.2005.08.027

[70] Jung, Sung-yoon. and Moon, Inhyuk., “Grip force modeling of a tendon-driven prosthetic hand,” *International Conference on Control, Automation and Systems*, (2008), pp. 2006-2009. DOI: 10.1109/ICCAS.2008.4694429.

[71] Midha, Ashok. “Mechanical Advantage of a Rigid-Body Single-Input Multiple-Output Port (SIPMOP) Mechanism.” Lecture Notes for ME 6704: Mechanics of Machinery, Missouri University of Science and Technology, Rolla, MO. 2011.

[72] Amis, Andrew A. “Variation of Finger Forces in Maximal Isometric Grasp Tests on a Range of Cylinder Diameters.” *Journal of Biomedical Engineering* Vol. 9 No. 4 (1987): pp. 313-320.

[73] An, Kai-Nan, Cooney, W. P., III, Chao, E. Y., and Linscheid, R. L. “Functional Strength Measurement of Normal Fingers.” *ASME Advances in Bioengineering.* pp. 89-90. San Francisco, CA, December 10-15, 1978.

[74] Radhakrishnan, S. and Nagaravindra, M., “Analysis of Hand forces in Health and Disease during Maximum Isometric Grasping of Cylinder.” *Medical & Biological Engineering & Computing* Vol. 31 No. 4 (1993): pp. 372-376

[75] Jones, Arthur J. “Weight Lifting Exercising Devices.” *US Patent 3858873*. 1975.

[76] McArdle, William D., Katch, Frank I., and Katch, Victor L. *Exercise Physiology: Energy, Nutrition, and Human Performance*. Williams & Wilkins, Baltimore, MD. (1996).

[77] Komi, P. V., *Strength and Power in Sport*, Blackwell Science Ltd., Oxford, UK 2003.

[78] Hamilton, N., Weimar, W., and Luttgens, K., *Kinesiology: Scientific Basis of Human Motion*, McGraw-Hill Companies, New York, NY. 2007.

[79] Balado, D., *Exercise Physiology: Energy, Nutrition, and Human Performance*, Williams & Wilkins, Baltimore, MD. 1996.

[80] Mazzeo, R. S., and Tanaka, H., "Exercise prescription for the elderly: current recommendations," *Sports Med.,* vol. 31, no. 11, (2001): pp. 809-818.

[81] Howell, L. L., and Midha, A., "Parametric Deflection Approximations for Initially Curved, Large-Deflection Beams in Compliant Mechanisms," *Proceedings of the 1996 ASME Design Engineering Technical Conferences,* 96-DETC/MECH-1215. (1996)

[82] Bushkoetter, Kyle. "Design of a Compliant Mechanism to Generate an Arbitrary Nonlinear Force-deflection Profile." MS Thesis, Missouri University of Science and Technology, Rolla, MO. 2018.

[83] Kattan, P. I., *MATLAB Guide to Finite Elements, An Interactive Approach,* Springer-Verlag, Berlin. 2008.

[84] Her, I., Midha, A., and Salamon, B. A., "A Methodology for Compliant Mechanisms Design: Part II – Shooting Method and Application," *American Society of Mechanical Design, Design Engineering Division*, (1992) *vol. 44, no. 2*, pp. 39-45.

[85] Bapat, S., "On the Design and Analysis of Compliant Mechanisms Using the Pseudo-Rigid-Body Model Concept," Ph.D. Dissertation, Missouri University of Science and Technology. Rolla, MO. 2015.

[86] Zong, M. L., Latash, M. L., and Zatsiorsky, V. M. "Force sharing among fingers as a model of the redundancy problem," *Experimental Brain Research*, (1998) *vol. 119*, pp. 276-286.

[87] "Ergonomic Guidelines for Selecting Hand and Power Tools," last modified on May 16, 2017, accessed October 10, 2020, https://www.ehstoday.com/health/article/21908634/ergonomic-guidelines-for-selecting-hand-and-power-tools

[88] Fraser, T. M., *Ergonomic principles in the design of hand tools.* International Library office, Geneva (1980).

[89] *A Guide to Selecting Non-Powered Hand Tools*. National Institute for Occupational Safety and Health, California (2004).

[90] Gong, Lin. “Guidelines for Designing Handheld Tools for The Elderly.” MS Thesis. Auburn University, AL. 2017.

[91] Gordon, Claire C. et al. 1988, *“Anthropometric Survey of US Personnel: Summary Statistics Interim Report*.” March 1989.

[92] “Instron 5900 Series Universal Testing Systems,” last modified on March 9, 2021, accessed March 10, 2021. https://www.instron.us/en-us/products/testing-systems/universal-testing-systems/low-force-universal-testing-systems/5900-series-universal-testing-systems-up-to-50-kn

[93] “Instron Static Load Cells,” last modified on March 7, 2021, accessed March 9, 2021. https://www.instron.us/en-us/products/testing-accessories/load-cells/static

[94] “Haas CNC Machine,” last modified on March 8, 2021, accessed March 9, 2021. https://www.haascnc.com/machines/vertical-mills/vf-series/models/small/vf-2.html

[95] “2 Flute Carbide End Mill,” last modified on March 8, 2021, accessed March 9, 2021. https://www.amazon.com/Flute-Long-Length-Carbide-Mill/dp/B06XGPN2S4

[96] Buschkoetter, K., Midha, A. “Design of a Compliant Mechanism to Generate an Arbitrary Nonlinear Force-Deflection Profile,” *Proceedings of the ASME 2018 International Design Engineering Technical Conferences and Computers and Information in Engineering Conference*, DETC2018-86360.

[97] Komatireddy, J, Midha, A, Lodagala, V, & Bagivalu Prasanna, P. “A Methodology to Design a Variable Resistance Hand Exerciser Using a Compliant Mechanism.” *Proceedings of the ASME 2020 International Design Engineering Technical Conferences and Computers and Information in Engineering Conference*. *Volume 10: 44th Mechanisms and Robotics Conference (MR)*. Virtual, Online. August 17–19, 2020. V010T10A015. ASME. https://doi.org/10.1115/DETC2020-22760

[98] “SAE-AISI 1074 (G10740) Carbon Steel mechanical properties”, last modified on November 06, 2013, accessed January 20, 2019. https://www.makeitfrom.com/material-properties/SAE-AISI-1074-G10740-Carbon-Steel

[99] “AISI 1074 Carbon Steel properties”, last modified on November 06, 2013, accessed January 20, 2019. https://www.azom.com/article.aspx?ArticleID=6558

[100] “1075 spring steel strips”, last modified on December 11, 2020, accessed December 12, 2020. https://www.mcmaster.com/catalog/127/4020

[101] "Honeywell Plastics Snap-fit Design Manual," last modified on April 2002, accessed March 8, 2019. https://oldnc.3dn.ru/Docs/Honeywell_Plastics.Snap-Fit_Design_Manual.pdf

[102] Hee Ahn, and Sung, et al. "Effects of Grip Curvature and Hand Anthropometry for the Unimanual Operation of Touchscreen Handheld Devices," *Human Factors and Ergonomics in Manufacturing & Service Industries,* vol. 26, no. 3 (2016): pp.367-380.

[103] Hegde, Alan. "Hand Tool Design', Lecture Notes, DEA 3250 Human Factors: Ergonomics, Anthropometrics, and Biomechanics, Cornell University, NY, delivered, Aug 2013.

[104] González, Alfonso, et al. "Optimisation of a laparoscopic tool handle dimension based on ergonomic analysis," *International Journal of Industrial Ergonomics,* vol. 48, (2015): pp.16-24.

[105] Harih, Gregor, and Dolšak, Bojan*, "Tool-handle design based on a digital human hand model," International Journal of Industrial Ergonomics,* vol. 43, no. 4 (2013): pp.288-295.

[106] "Hand Tools for Industry and Manual works," last modified on December 20, 2020, accessed October 2, 2020, https://www.phoenixcontact.com/en-il/products/hand-tools

[107] "Meccion Aviation Snips," last modified on April 21, 2019, accessed November 2, 2020, https://www.amazon.com/Meccion-Aviation-Straight-Non-slip-Comfortable/dp/B07G54ZKV5

[108] "Thermo Plastic Elastomers," last modified on March 2, 2021, accessed March 4, 2021.https://www.timcorubber.com/rubber-materials/thermoplastic-elastomers-tpe/

[109] "TPE &TPU Injection Molding Resins," last modified on February 24, 2021, accessed March 4, 2021. https://www.stackplastics.com/injection-molding-resin/tpe-tpu

[110] "Thermo Plastic Elastomers and Thermo Plastic Polyurethane," last modified on February 26, 2021, accessed March 4, 2021. https://www.kentelastomer.com/tpe-vs-tpu/

[111] "DuPont- Design Guide Module - Delrin," last modified on April 2015, accessed March 8, 2019. http://foremostplastic.com/wp-content/uploads/2015/04/DuPont-Module-III-Delrin.pdf

[112] “Soft vs. Hard Tooling for Injection Molding,” last modified on February 28, 2021, accessed March 4, 2021. https://www.3erp.com/blog/soft-vs-hard-tooling-for-injection-molding/

[113] “3D-Printed Molds vs. Aluminum Tooling,” last modified on August 14, 2017, accessed March 4, 2021. https://www.protolabs.com/resources/blog/3d-printed-molds-vs-aluminum-tooling/?addsearch=soft%20tooling

[114] “Design Guidelines: Plastic Injection Molding”, last modified on January 20, 2021, accessed January 20, 2020. https://www.protolabs.com/services/injection-molding/plastic-injection-molding/design-guidelines/

[115] “Protolabs: Injection Molding Surface Finishes,” last modified on October 30, 2015, accessed March 9, 2021. https://www.amazon.com/Flute-Long-Length-Carbide-Mill/dp/B06XGPN2S4

[116] “How to Control Injection Molding Surface Finish,” last modified on June 26, 2019, accessed March 9, 2021. https://www.kaysun.com/blog/how-to-control-your-surface-finish

[117] “Injection Molding SPI Surface Finishes,” last modified on March 9, 2021, accessed March 9, 2021. https://www.3dhubs.com/knowledge-base/injection-molding-spi-surface-finishes/

VITA

Jyothi Komatireddy was born in Hyderabad, Andhra Pradesh, India. She received her bachelor's degree in Mechanical Engineering from Gokaraju Rangaraju Institute of Engineering and Technology, Hyderabad, India, in May 2012. She worked as a senior executive design engineer at Kennametal Shared Services Private Limited, Bangalore, from July 2012 to July 2017. In January 2018, she was accepted into the MS program in Mechanical Engineering at Missouri University of Science and Technology, Rolla. She received her Master of Science in Mechanical Engineering from Missouri S&T in July 2021.